ELECTRIC FIELD ASSISTED GROWTH AND CONTROL OF MORPHOLOGY OF FILMS FOR ORGANIC DEVICES

A Thesis Submitted in Partial Fulfillment for

the Requirements of the Degree of

Doctor of Philosophy

By

A.V. RAAGHESH

CHEMISTRY AND PHYSICS OF MATERIALS UNIT

JAWAHARLAL NEHRU CENTRE FOR ADVANCED
SCIENTIFIC RESEARCH

(A DEEMED UNIVERSITY)

Bangalore – 560064

July 2019

Dedicated to my parents

Declaration

I hereby declare that the matter embodied in the thesis entitled *"Electric Field Assisted Growth And Control Of Morphology Of Films For Organic Devices"* is the result of the work carried out by me under the supervision of Prof. K. S. Narayan, at Molecular Electronics Laboratory, in Chemistry and Physics of Materials Unit, Jawaharlal Nehru Centre for Advanced Scientific Research, Bangalore, India. It has not been submitted for the award of any degree or diploma or associateship of any other university or institute.

In keeping with the general practice in reporting scientific observations, due acknowledgement has been made whenever the work described is based on the findings of other investigators.

(A. V. Raaghesh)

JAWAHARLAL NEHRU CENTRE FOR ADVANCED SCIENTIFIC RESEARCH

Bangalore – 560064

K. S. NARAYAN

Professor and President In-Charge
Phone: +91 80 2208 2822/2750
E-mail: narayan@jncasr.ac.in
Fax: + 91 80 2208 2766
URL: www.jncasr.ac.in/narayan

July 30th, 2019

Certificate

I hereby certify that the matter embodied in this thesis entitled *"Electric Field Assisted Growth And Control Of Morphology Of Films For Organic Devices"* is the result of the work carried out by Mr. A.V. Raaghesh at the Molecular Electronics Laboratory, in Chemistry and Physics of Materials Unit, Jawaharlal Nehru Centre for Advanced Scientific Research, Bangalore, India, under my supervision and it has not been submitted for the award of any degree or diploma or associateship of any other university or institute.

Prof. K. S. Narayan

(Research supervisor)

Acknowledgements

I have no words to thank my parents for the sacrifices they have made in their life, for getting me and my brother educated. My brother Rajish for being a good friend to me and always being there for me.

Synopsis

Organic devices are a relatively newer generation of electronic devices which can be flexible and lightweight. Solution processing of these devices allows them to be scaled up by printing technologies. These factors allow organic devices to be crucial in certain niche areas where they have a significant edge over conventional inorganic devices. However certain challenges pertaining to the device performance and stability have to be overcome to meet the full potential of these devices. In this thesis, external electric field treatment (EFTA) has been used to address some of these issues related to organic devices, mainly organic solar cells and organic memristors. This treatment involves application of external electric field (EF) during the thermal annealing stage of device fabrication. Understanding the modifications in morphology introduced by the EFTA treatment and how the modifications can benefit the performance of the organic devices is the core of this thesis.

The first part focuses on EFTA treatment of model organic solar cell system of P3HT: PCBM. The dependence of donor chain length on EFTA treatment was studied by varying the molecular weight of the semi-crystalline donor polymer. EF strength required for optimal solar cell device performance was found to dependent on the molecular weight of the donor. It was also observed that EFTA treatment was able to control the vertical phase segregation of the donor and acceptor components in the active layer by varying the strength and direction of EF applied during the treatment. The observed improvement in device performance was attributed to increased hole mobility due to enhanced crystallinity of the donor component and optimal vertical phase segregation of the active layer components.

The second part focuses on extension of EFTA treatment to active layer system of PTB7-Th: PCBM, where PTB7-Th is a prototypical amorphous polymer donor. Additive DIO used in the fabrication of PTB7-Th: PCBM is imperative to improve device performance. The presence of residual DIO in the active layer however leads to stability issues in the device. Thermal treatment used to effectively remove DIO leads to reduction in solar cell device efficiency. Controlled Vertical phase segregation of active layer components by EFTA treatment was able to mitigate the efficiency loss incurred by the thermal treatment. This leads to stable solar cell devices with reasonable efficiency parameters.

The third part focuses on EFTA treatment of active layers in which the donor component was also small molecule along with PCBM acceptor. The results indicated that it is the PCBM

acceptor molecule that responds to the external EF. Studies carried out on polymer donor: non-fullerene acceptor systems did not show any discernible changes with EFTA treatment. Ability of the active layer to respond to EFTA treatment was strongly dependent on the solvent that was used during the fabrication. The presence of additive, DIO was shown to significantly enhance response towards EFTA treatment. This was attributed to the low vapour pressure of DIO allowing it to stay longer in the film. Selective dissolution of PCBM by DIO has shown to be the reason why PCBM is able to migrate in the presence of EF during EFTA treatment.

The fourth part focuses on EFTA treatment on organic memristors. Active layer of organic memristors contains semiconducting polymer (PFO/ P3HT) channels in a matrix of ferroelectric dielectric polymer (PVDF-TrFE), sandwiched between two electrodes. Injection of charge carriers from electrodes into semiconducting channels is controlled by the polarization state of the ferroelectric polymer. Semiconducting channels that do not bridge the top and bottom electrodes limits maximum current allowed through the device. EFTA treated devices has shown an improvement in this parameter over control devices. The improvement in current was attributed to increase in bridged semiconducting channels and optimal domain sizes of semiconducting polymer regions in the ferroelectric polymer matrix.

List of Publications

- **Raaghesh Vijayan**, K. Swathi, K. S. Narayan, *"Synergistic Effects of Electric-Field-Assisted Annealing and Thermal Annealing in Bulk-Heterojunction Solar Cells"*, ACS Appl. Mater. Interfaces, 2017, 9, 23, 19436-19445

- **Raaghesh Vijayan**, Abdul Azeez, K. S. Narayan *"Enhanced Stability and Optimized Morphology Induced by Electric-Field-Assisted Annealing of Bulk Heterojunction Solar Cells"*, Solar RRL, 2019, 3, 10, 1900120

- **Raaghesh Vijayan**, K. S. Narayan, *"Strategy for Enhancing Performance of Organic Ferroelectric Memristors"*, Manuscript submitted.

- **Raaghesh Vijayan**, K. S. Narayan, *"Role of solvent additive during electric field assisted thermal annealing of organic solar cells"*, Manuscript under preparation.

- Shekhar Shinde, **Raaghesh Vijayan**, K. S. Narayan, S. K. Asha *"Supramolecular complexes of poly(3-hexylthiophene)-block (and random)-poly[3-(2-(6-carboxyhexyl)methyl)thiophene] copolymers with perylene bisimide"*, J. Polym. Sci. A, 2018, 56, 1574–1583

Table of Contents

Chapter 2: *Electric Field Assisted Thermal Annealing Treatment of Semi-Crystalline Polymer: Fullerene-Based Solar Cell Devices*

Chapter 3: *Electric Field-Assisted Thermal Annealing (EFTA) Treatment of Amorphous-Polymer Donor: Fullerene Acceptor-Based Solar Cells*

Chapter 4: *Electric Field Assisted Thermal Annealing (EFTA) Treatment of Small Molecule Donor-Based and Non-Fullerene Acceptor-Based Solar Cells*

Chapter 5: *Organic Ferroelectric Memristors (OFMs) and Electric Field Assisted Thermal Annealing (EFTA) Treatment of Organic Ferroelectric Memristors*

Abbreviations

OPV	Organic Photovoltaic
OSC	Organic Solar Cell
BHJ	Bulk Heterojunction
J_{sc}	Short Circuit Current
V_{oc}	Open Circuit Voltage
FF	Fill Factor
HOMO	Highest Occupied Molecular Orbital
LUMO	Lowest Unoccupied Molecular Orbital
EQE	External Quantum Efficiency
P3HT	Poly(3-hexylthiophene-2,5-diyl)
PCBM	Phenyl-C71-butyric acid methyl ester
PTB7-Th	Poly[4,8-bis(5-(2-ethylhexyl)thiophen-2-yl)benzo[1,2-b;4,5-b']dithiophene-2,6-diyl-alt-(4-(2-ethylhexyl)-3-fluorothieno[3,4-b]thiophene-)-2-carboxylate-2-6-diyl)]
DIO	1,8-Diiodooctane
PBDBT	Poly[(2,6-(4,8-bis(5-(2-ethylhexyl)thiophen-2-yl)-benzo[1,2-b:4,5-b']dithiophene))-alt-(5,5-(1',3'-di-2-thienyl-5',7'-bis(2-ethylhexyl)benzo[1',2'-c:4',5'-c']dithiophene-4,8-dione)]
PBDBT-2Cl	Poly[(2,6-(4,8-bis(5-(2-ethylhexyl-3-chloro)thiophen-2-yl)-benzo[1,2-b:4,5-b']dithiophene))-alt-(5,5-(1',3'-di-2-thienyl-5',7'-bis(2-ethylhexyl)benzo[1',2'-c:4',5'-c']dithiophene-4,8-dione)]
ITIC	3,9-bis(2-methylene-(3-(1,1-dicyanomethylene)-indanone))-5,5,11,11-tetrakis(4-hexylphenyl)-dithieno[2,3-d:2',3'-d']-s-indaceno[1,2-b:5,6-b']dithiophene
ITIC-2F	3,9-bis(2-methylene-((3-(1,1-dicyanomethylene)-6,7-difluoro)-indanone))-5,5,11,11-tetrakis(4-hexylphenyl)-dithieno[2,3-d:2',3'-d']-s-indaceno[1,2-b:5,6-b']dithiophene
SA48	tris{4-[5'-(1,1,-dicyanoprop-1-en-2-yl)-2,2'-bithien-5-yl]-2-methoxyphenyl}amine
OFM	Organic Ferroelectric Memristor
PFO	Poly(9,9-di-n-octylfluorenyl-2,7-diyl)

PVDF-TrFE   Poly(vinylidene fluoride-co-trifluoroethylene)

Chapter 1

Introduction

1.1 Solar cells

Non-renewable sources of energy like petroleum, coal and natural gas contributed to 75% of the world's energy requirements in 2018.[1] Studies have shown that world's energy demand in 2018 was more than 23 000 TWh and increased by 2.9%.[1] This level of energy consumption needs a shift from fossil-fuel and non-renewable energy sources to affordable-economic renewable sources with minimum impact on factors leading to climate change.[2]

Among the different renewable energy sources, solar energy is the most abundant. Solar energy can be tapped in the form of heat (solar-thermal) or electricity (photovoltaics). In the field of solar photovoltaics, the basic solar cell device which converts solar energy into electrical energy are largely silicon-based. In these devices, absorbed photons generate charge carriers which are then extracted into an external circuit and generate power at large-area efficiencies of 25 %.[3]

1.2 Organic solar cells

These cells have an active layer consisting of organic semiconductors with appropriate buffer layers and electrodes. The mechanism of energy conversion of these solar cells is conceptually different from that of Silicon solar cells.

1.2.1 Advantages of organic solar cells

Organic solar cells (OSCs) have certain inherent advantages over conventional Si-based solar cells, namely:

i.   Flexibility: Silicon solar cells are usually thick (> 1 μm) because of their low absorption coefficient. They are also rigid. These factors prevent them from being fabricated on flexible substrates. Organic solar cells overcome this barrier since the active layers are usually thin layers (< 200 nm) owing to its high absorption coefficients.

ii. Bandgap tunability: The absorption bandgap and absorption window of molecules are determined by the structure. By carefully tuning the structure of the molecules of the active layer, organic solar cells, which absorb in selective absorption range, can be fabricated.

iii. Solution-processable: Organic solar cells can be fabricated by solution-processable techniques like spin-coating, drop-casting at room temperature conditions. This allows easier scaling up of these devices using roll to roll processing methods.

iv. Low energy cost: Unlike the conventional solar cells, which require energy-intensive processing steps, the energy cost involved in the fabrication of organic solar cells is quite low. Life cycle analyses of these solar cells have shown that the energy invested in the fabrication of these solar cells can be gained back in a matter of months when the solar cell is under operation.[4, 5]

However, major drawbacks from the technical standpoint are the absence of proven stability of these devices, especially under extreme environmental conditions over a long period. It is expected that an improved understanding of the decay processes involved should assist in addressing these issues.

1.2.2 Organic (Polymer) semiconductors
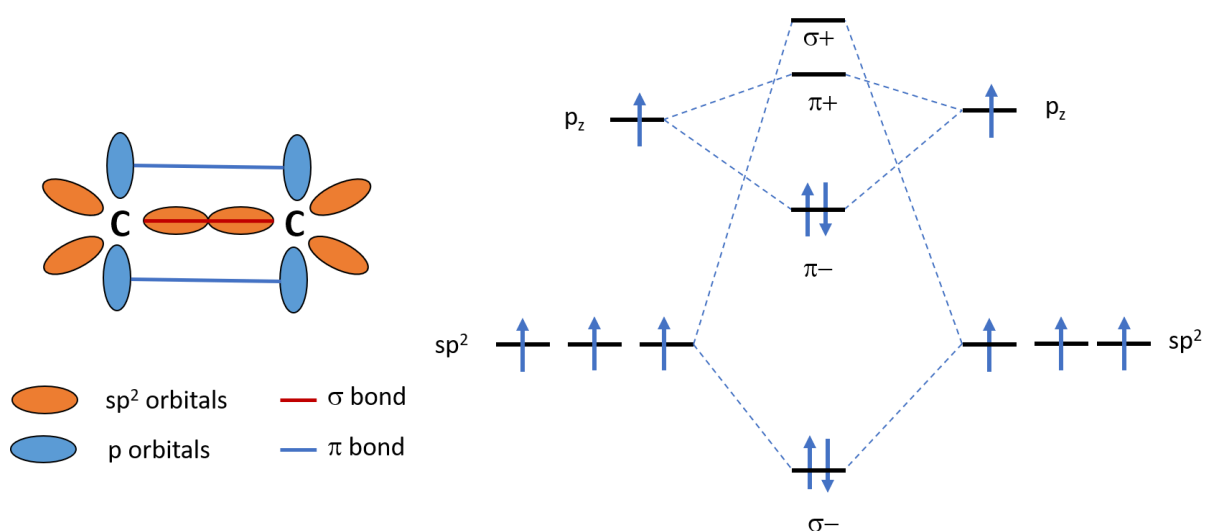
Figure 1.1 *Schematic of orbital overlap for two sp^2 hybridised carbon atoms.*

The charge transport in low-dimensional polymer semiconductors is different from conventional transport in doped inorganic semiconductors. [6, 7] The carbon atoms in these systems are sp^2-hybridized having sp^2 orbitals in a trigonal planar configuration with the p$_z$ orbitals perpendicular to the plane (shown in Figure 1.1). This forms a conjugated system with delocalized π electrons due to resonating alternate double ($\sigma+\pi$) bonds and (σ) bonds in the molecule. As a result of this conjugation, p$_z$-orbitals split into two energy states, completely filled lower-energy Bonding Molecular Orbital state which acts as Highest Occupied Molecular Orbital (HOMO) and partially filled higher-energy Non-Bonding Molecular Orbital state

which acts as Lowest Unoccupied Molecular Orbital (LUMO). The energy gap between the LUMO and HOMO levels forms the bandgap. As the delocalization of the π_z electrons increases, the bandgap of these organic semiconductors reduces, and the associated energy levels become closely spaced, converging to a band structure nearly akin to inorganic semiconductors. In general, polymers are structurally and electronically disordered materials. A perturbation along the conjugation of the polymer backbone can change the HOMO and LUMO levels locally. The density of states available for charge transport is often approximated by Gaussian distribution. The mechanism of conductivity/mobility in these molecules is based on the motion of charged defects within the conjugated framework. Hence, the bulk parameter of charge transport mobility in polymer materials is effectively much lower than in crystalline inorganic materials.

Cathode	Cathode	Cathode
Active layer	Acceptor	Bulk Heterojunction
	Donor	
Transparent Electrode	Transparent Electrode	Transparent Electrode

a) Single layer OSCs   b) Bilayer OSCs   c) Bulk heterojunction OSCs
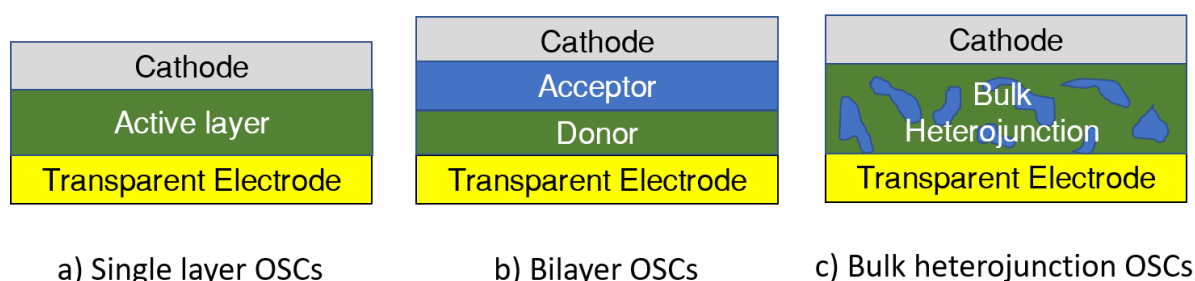
Figure 1.2 Evolution of organic solar cells (OSCs)

Due to the inherent low dielectric constant and high electron-lattice interactions of these organic materials, the electron-hole pair generated upon photon absorption remains bound because of the strong coulombic interaction. The characteristics of the bound electron-hole pair -'exciton' such as the binding energy and diffusion lengths play a decisive role in charge generation. To generate photocurrent, the exciton has to be separated as electrons and holes, and collected at the respective electrodes.

In the initial organic solar cells fabricated, the active layer was made up of single organic semiconductor material. The efficiency of these single-layer organic solar cell devices was very low ($\sim 10^{-3} - 10^{-1}$ %). It was realized that to efficiently split the exciton, at least two organic semiconductors with differing energy (LUMO or HOMO) levels are required. The organic material with higher LUMO levels acts as the donor molecule, whereas the organic material with lower LUMO levels acts as the acceptor. The photon absorption and the generation of exciton generally ensue in the donor molecule in systems involving fullerene derivatives as the acceptors.

At the interface-junction of these two components, the electron gets transferred to the lower LUMO energy levels. The spatially separated charges across the interface can remain bound together as Charge Transfer (CT) state prior to a complete charge-separated state or a recombination process. After separation of the CT state, the hole remaining in the donor molecule and the electron remaining in the acceptor molecule have to be collected at the respective electrode. To facilitate the charge transport of the separated charge carriers, donor molecules provide a transport network for the holes while the acceptor molecules provide the same for electrons. Bi-layer solar cells where the active layer is made of the two adjacent layers of donor and acceptor lead to efficiencies in the range of 1%.[8] The efficiency of these bilayer solar cells is limited by the thickness of the solar cells, which in turn is limited by exciton diffusion length. Exciton diffusion length (usually around 10-20 nm) is the distance exciton travels before recombining on its own.[9] This type of recombination is called 'Geminate recombination,' and acts as a loss parameter for the performance of the solar cells since the generated charge carriers are not extracted.
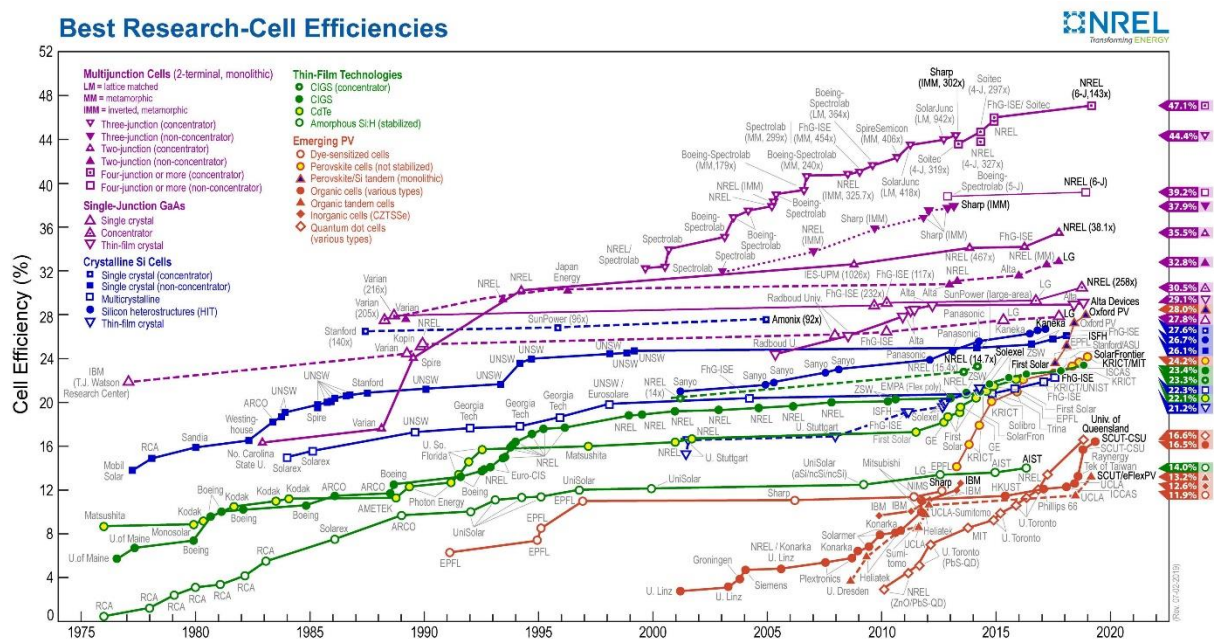
Figure 1.3 *NREL Efficiency chart of different solar cell technologies. The rapid growth of organic solar cells (OSCs) can be observed in the chart*

Significant improvement in the working of organic solar cells was achieved with the introduction of bulk heterojunction (BHJ) solar cells.[10] In these BHJ solar cells, the active layer consisted of a blend of donor and acceptor molecule mixed together leading to a film formation with the donor phase and acceptor phase forming a large number of interfaces in the 3-

dimensional bulk. This type of solar cells provides a sufficient interface area of donor and acceptor for charge generation and percolation pathways for charge collection. Evolution of organic solar cells has been depicted in the schematic (Figure 1.2). Recently, by carefully tuning the structure of the molecules involved, and the morphology of the active layer, efficiency as high as 16% have been reported for single layer BHJ organic solar cells.[11,12] NREL chart (shown in Figure 1.3) depicts the improvement in best device efficiencies obtained for organic solar cells in the last few years, along with other solar cell technologies.

1.2.3 Different architectures of organic solar cells

Single-layer organic BHJ solar cells can be typically fabricated in two different architectures, depending on whether the transparent electrode acts as a hole-collecting electrode or electron-collecting electrode (Figure 1.4). If the transparent electrode acts as a hole-collecting electrode or electron-collecting electrode, it is termed 'normal' device structure or 'inverted' device structure, respectively. For normal device structure, low-work function metal is reserved as the top electrode to facilitate electron collecting. However, low-work function metal at the top of the device will be prone to oxidation and leads to stability issues. The inverted device structure is relatively more stable with high-work-function metal on top.

(a) Normal device structure   (b) Inverted device structure
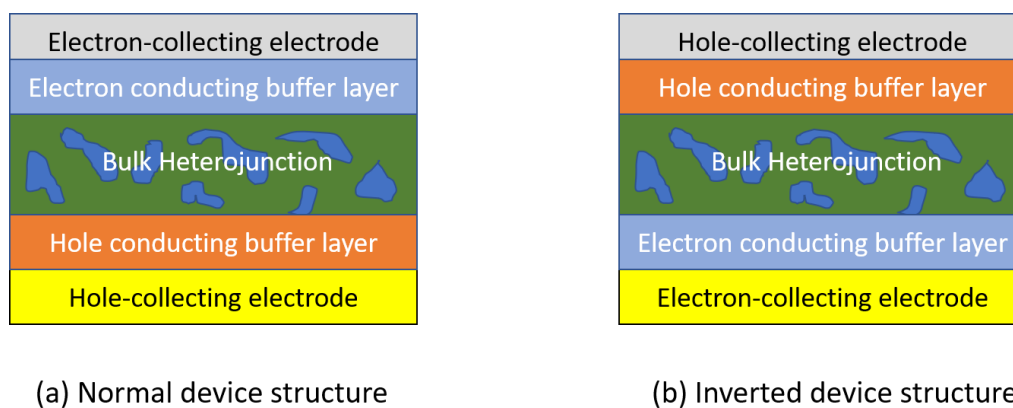
Figure 1.4 Different architectures of organic solar cells (OSCs)

1.2.4 Buffer layers

The active layer is usually sandwiched between buffer layers to improve the charge collection efficiency of separated charges to the respective electrodes.[13, 14] Buffer layers generally allow only one type of charge carriers to flow through them while limiting charge carriers of opposite charge to flow through them. These layers are usually solution-processed or thermally evaporated. Commonly used electron-buffer layers include Zinc oxide (ZnO), Lithium fluoride

(LiF) and Titanium oxide (TiO$_x$). Poly(3,4-ethylenedioxithiophene): poly(styrenesulphonate) (PEDOT: PSS), Molybdenum oxide (MoO$_x$), Vanadium oxide (V$_2$O$_5$) are typical hole buffer layers. Figure 1.4 shows the typical device architectures of organic solar cells with buffer layers.

1.2.5 Stability of organic solar cells

Along with increased efficiency numbers, the stability of OSCs also has to be addressed to make these OSCs commercially viable. Currently, the stability of OSCs is one of the bottle-necks towards scaling up of these devices. There are a lot of factors limiting the stability of solar cells namely[15, 16]

i)   The reaction of the active layer to oxygen and moisture
ii)   Degradation under thermal stress
iii) Intolerance towards mechanical stress
iv)   Degradation of metal electrodes
v)   Unfavourable diffusion of electrodes and buffer layers into the active layer
vi)   Metastable BHJ morphology which evolves over time

Most of these factors can be overcome by careful selection of materials for fabrication and suitable encapsulants. Among these factors, metastable device morphology, which leads to irreversible morphological changes in the active layer is the least understood. The thesis presents a few methods to address some of these issues.

1.2.6 Solar cell parameters

100 mW/cm^2 is the universal standard for incident power used in the measurement of solar cells, and corresponding solar spectra is given by AM 1.5 Global (Figure 1.5). Typical schematic of current density-voltage (J-V) characteristics of the solar cell under illumination is shown in Figure 1.6. In spite of differences with inorganic solar cells, the J-V characteristics equations used for conventional cells is applicable for OSCs.

$$J = J_o \left[exp\left(\frac{eV}{nk_BT}\right) - 1 \right] - J_{ph} \qquad (1.1)$$

Here, J is the current density through the device, J$_o$ is the reverse saturation current density through the device under dark conditions of operation, J$_{ph}$ is the photogenerated current density, n is the ideality factor, e is the elementary charge, k$_B$ is the Boltzmann's constant and T is the absolute temperature of operation.
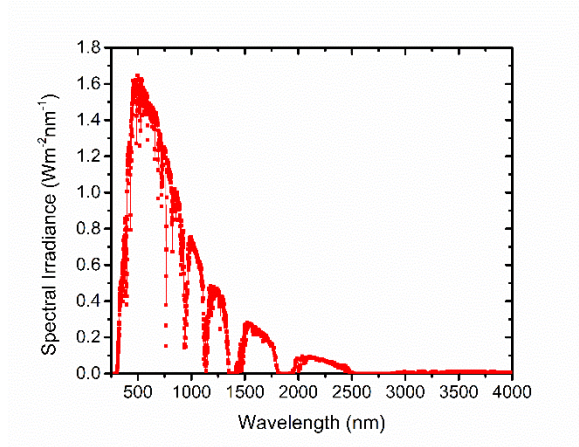
***Figure 1.5** AM 1.5 Global Standard solar spectra used for the measurement of solar cells*

The power conversion efficiency (η) of solar cells is dependent on three main parameters, namely Open-Circuit Voltage (V_{oc}), Short-Circuit Current (J_{sc}), and Fill factor (FF). It is given by the following equation,

$$PCE(\eta) = \frac{V_{OC} \times J_{SC} \times FF}{P_{in}} \qquad (1.2)$$
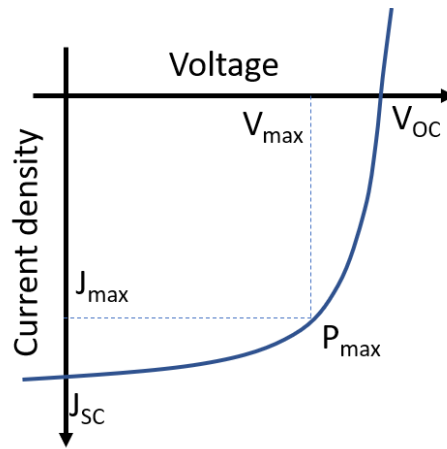
***Figure 1.6** Typical current density – voltage (J-V) characteristics of solar cells under illumination*

V_{oc} is the maximum obtainable voltage from a solar cell and it occurs when the current through the device is zero. J_{sc} is the current following through the solar cell when the voltage across the solar cell is maintained zero. FF is a quantity which describes the maximum power that can be obtained from the solar cell and is given by the following equation.

$$FF = \frac{V_{max} \times J_{max}}{V_{OC} \times J_{SC}} \qquad (1.3)$$

For organic solar cells, V_{oc} is primarily controlled the effective bandgap of the active layer, i.e., $LUMO_{acceptor}$- $HOMO_{donor}$, where energy loss term is also included.[17-19] Hence, it is crucially dependent on the choice of the active layer components. E_{loss} is associated with energy losses involved during exciton dissociation and charge transport.

$$eV_{OC} = (LUMO_{acceptor} - HOMO_{donor})E_{loss} \tag{1.4}$$

J_{sc} of organic solar cells quantifies the portion of photogenerated charge carriers extracted with only the in-built potential of the device.[20-22] It is limited by recombination losses inside the active layer of the solar cell. At higher reverse bias voltages, all the photogenerated charge carriers will be extracted, and J_{sc} becomes equal to J_{sat} (saturation current density).

FF reflects the efficacy of charge extraction of the separated charge carriers.[23-25] Buffer layers, which were discussed earlier help in improving the FF of the solar cells.

1.3 Working of Bulk heterojunction organic solar cells
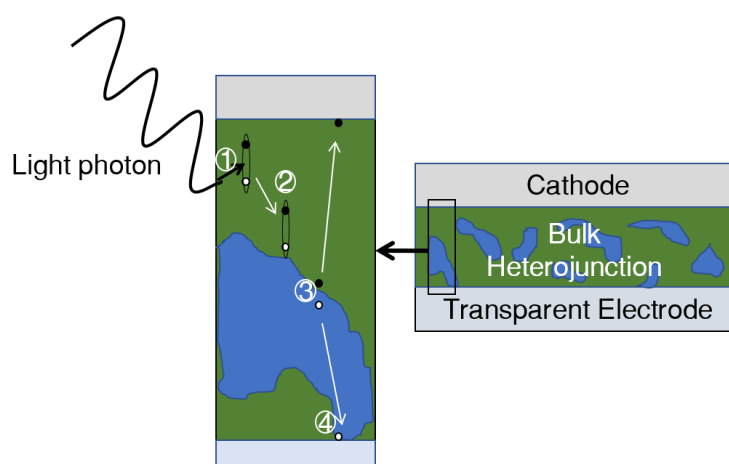
Figure 1.7 *Schematic representation of morphological perspective on working of organic solar cells*

The working of BHJ OSCs can be summarized by the following steps

1. Absorption of photon by the active layer and formation of exciton
2. Diffusion of exciton to donor-acceptor interface
3. Exciton dissociation, formation of Charge-Transfer (CT) state and separation of CT state at the interface
4. Migration of separated charges and collection at respective electrodes

Internal Quantum Efficiency (η_{IQE}) of an OSC is given by the product of the efficiency of each of the above-mentioned steps.

By definition, Internal Quantum Efficiency,

$$\eta_{IQE} = \eta_{AB}\eta_{D}\eta_{CT}\eta_{CC} \qquad (1.5)$$
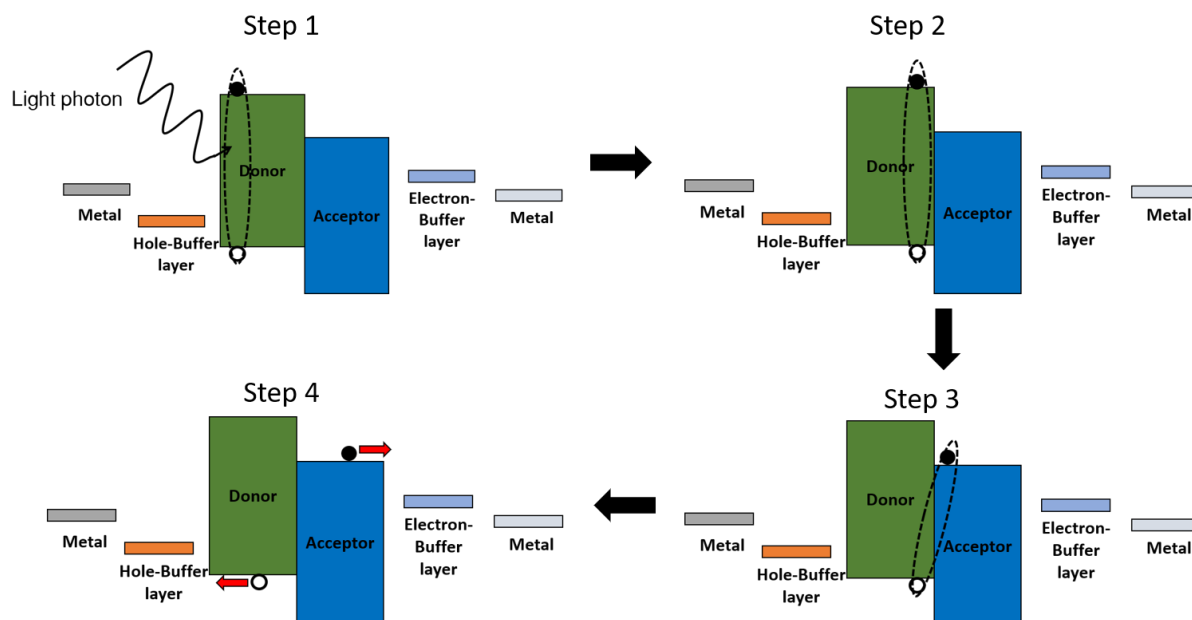
Figure 1.8 *Schematic representation of energetic perspective on working of organic solar cells*

Here, η_{AB} is the efficiency of absorption of the incident light. This efficiency parameter is dependent on the amount of overlap between the absorption of the active layer to that of the solar spectra, and the thickness of the active layer.

η_{D} is the efficiency of the diffusion of the formed exciton to the Donor-Acceptor interface. It is limited by the exciton diffusion length (λ_d).[26] Domain sizes of donor and acceptor components smaller than the λ_d are required in the active layer to ensure that the efficiency is not lost at this step.

η_{CT} is defined as the efficiency of dissociation of exciton and formation of the charge-transfer (CT) state, and its dissociation into free charges. It depends on the morphology of the active layer and the choice of donor and acceptor. Recombination of CT state without leading to separated charges needs to be restricted.

η_{CC} is the efficiency of the collection of separated charges. This parameter depends on the percolation pathways for separated charges in the active layer to reach the electrode, choice of

electrode and buffer layers. The charge carriers can undergo recombination with charge carriers of opposite type in the active layer before reaching the electrodes. This recombination loss process is termed Non-Geminate or Bimolecular Recombination.[27]

Schematic representation of these above-mentioned steps involved in the working of solar cells is shown in Figure 1.7 (morphological perspective) and Figure 1.8 (energetic perspective).

1.4 Morphology of organic solar cells

The morphology of the active layer film plays a critical role in all the efficiency parameters discussed earlier.[28] Morphology characterization techniques like X-ray Scattering methods (Small and Wide Angle X-ray Scattering,[29] Polarized X-ray Scattering,[30] Resonant Soft X-ray Scattering),[31] Atomic Force Microscopy, and Transmission Electron Microscopy have allowed the researchers in the field to obtain correlations between internal microstructure and the resultant solar cell device performance. The solution containing the blend of donor and acceptor components is cast into films using spin-coating or doctor blade technique. The resultant morphology is ultimately dictated by thermodynamics and kinetics of film formation parameters dominated by the degree of phase separation between the donor and acceptor components.

A basic thumb rule for optimum morphology for solar cell device performance is the need for

i) Domain sizes to be smaller than the exciton diffusion length so that all the generated excitons access the donor-acceptor interface.

ii) Presence of percolation pathways in the active layer for the separated charge carriers to reach the respective electrodes.

For polymer components, parameters like regioregularity, molecular weight, side chains, and molecular backbone dictate interactions between other polymer molecules of the same type and other components in the blend. Solvents used for casting active layer films also play a role in deciding the final morphology, since the solubilities of active layer components determine the kinetics of formation of solid-phase from the liquid phase. Solvents in which active layer components have comparable high solubilities are found to yield well-mixed smooth films with low roughness. The D:A ratio required for good film formation features is D-A system-specific. A balance of factors required for charge generation, transport, and extraction processes form a major part of device studies leading to efficient solar cells.

The morphology of the active layer immediately obtained after spin-coating is usually not favourable for device performance. For these solution-processed solar cells, external processing treatments are used to control the organization of the blend components to form a morphology suitable for optimum charge generation and transport, to extract the best device performance from a given D-A system. Some of them are:

1.4.1 Thermal annealing treatment
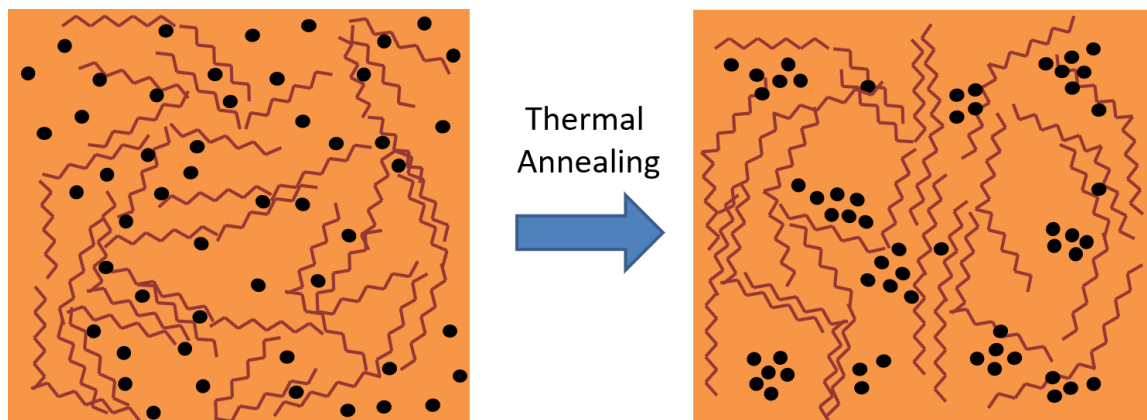
Figure 1.9 *Schematic representing morphological modifications due to thermal annealing treatment. The red lines indicate polymer chains and black circles represent acceptor small molecules. Thermal annealing improves the ordering of the polymer chains and increases aggregation of the small molecules.*

Thermal annealing treatment is the process by which the spin-coated active layer films are heated above their glass transition temperature for a short duration of time.[32, 33] Thermal annealing treatment has been used to increase and optimize the fraction of ordered regions in the active layer, where temperature and duration of treatment are process parameters. This treatment is effective in BHJ systems in which one of the components is semi-crystalline in the thin-film state. Thermal annealing treatment has shown to increase phase segregation of the active layer components and improve domain purity. For a semi-crystalline polymer: small molecule BHJ system, there are differing views on the origin of driving forces behind the phase separation of the active layer components due to thermal annealing. Few reports suggest that phase separation is mainly driven by crystallization of the polymer donor at higher temperatures, which leads to enhanced π-π stacking of the polymer chains. This subsequently allows acceptor small molecules to aggregate over longer time scales.[34] Few other reports claim that acceptor molecule aggregation kinetics competes with the crystallization kinetics of the donor polymer.[35]

Thermally annealed films have shown improved packing (better crystallinity) of semi-crystalline component, reflected in improved peaks in X-ray diffraction spectra and better charge carrier mobility in the blend. This enhanced charge carrier mobility has been found to improve the transport of separated charge carriers and reduce bimolecular recombination in the BHJ system. Schematic showing morphological changes in the active layer with thermal annealing is shown in Figure 1.9. Optimum thermal annealing temperature and duration is dependent on the active layer BHJ system. There is a critical threshold above which the treatment can become detrimental and can lead to unfavourable morphology. Thermal annealing at higher than optimum temperatures or longer durations of time creates larger phase-separated domains in the active layer, which limits charge generation efficiency and is undesirable for solar cell device performance.[32, 36, 37]

1.4.2 Solvent vapour annealing treatment

Spin-coating of active layer on substrates

Storing the spin-coated active layer in a solvent vapour rich atmosphere

Solvent-annealed active layer
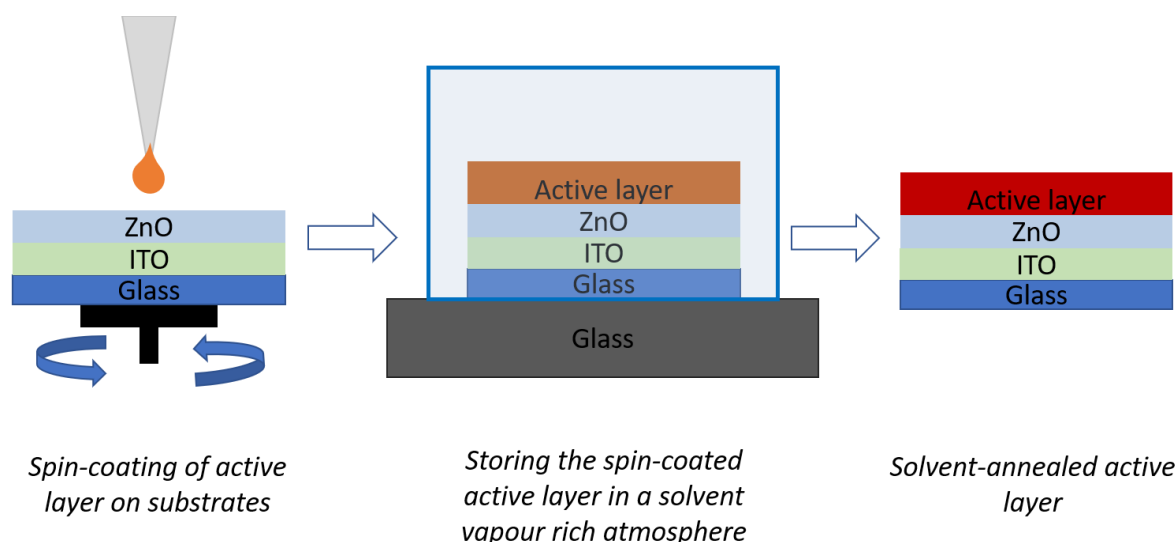
***Figure 1.10** Schematic representing solvent vapour annealing treatment of active layer thin films.*

Solvent vapour annealing treatment involves storing the spin-coated active layer films in a solvent-vapour rich environment.[38, 39] This reduces the rate of evaporation of the remnant solvent from the thin film. This allows the active layer components to redistribute into a more favourable morphology. The observed improvement in device performance is ascribed to increased ordering and crystallinity of the semi-crystalline donor component in the blend.

The spin-casted active layer films can also be stored in vapour-rich atmospheres of solvents other than the host solvent. By carefully choosing the vapour solvent, aggregation in the active

layer can be controlled in one of the components which has more solubility to the vapour annealing solvent.[40] Two-step vapour-annealing treatments where spin-coated active film is vapour treated with two different solvents, one after the other, have shown to improve device performance.[41] Use of mixed vapours of two different solvents have also been used to tune the morphology of the active layer thin film.[42] Schematic of methodology of solvent vapour annealing treatment is shown in Figure 1.10.

1.4.3 Use of Additives

The additives are high boiling solvents with low vapour pressure added in small quantities to the native solvent used to cast the active layer film.[43, 44] Additives usually have selective dissolution to one of the active layer components, usually the acceptor molecule. Additives stay longer in the film than the native solvent and allow the BHJ to reach optimum morphology for device performance. 1,8-Di-iodo-octane (DIO), alkyl-dithiols, 1-chloronaphthalene are some of the commonly used additives. For semi-crystalline donor BHJ systems, usage of additives has shown to improve phase separation of the active layer components. On the contrary, for amorphous donor BHJ systems, additives have shown to reduce phase separation and improve percolation of acceptor into donor-rich regions. Additives have also shown to bring in vertical phase segregation of active layer components in the thin film.[45, 46] These reports indicate that for amorphous polymer donor-based BHJ systems, acceptor small molecules tend to segregate in the lower segment of the BHJ layer. On the contrary, for the semi-crystalline polymer donor-based BHJ systems, the difference between the interaction parameter between the donor and acceptor drives donor polymer to the bottom of the BHJ film while acceptor small molecule displaces to the BHJ-air interface.

1.5 Patterning of organic thin films with external electric field

Pioneering work on patterning of thin film with external electric field were initially carried out in the groups of Prof. U.Steiner and Prof. T.P. Russell.[47-50] Electric field induced pattern formation on soft films is termed Electro-Hydro-Dynamic Lithography. The physical basis of this patterning technique is the amplification of fluctuations at a thin film-air interface or thin film-thin film interface (for bilayers) by a destabilizing force generated when an electric field is applied perpendicular to the surface. Patterning of thin films occurs when the destabilizing electrostatic forces is sufficiently large to overcome the stabilizing forces of viscoelastic forces of the thin film and gravity acting at the interface.

Usually, polymer films are coated on one of the electrodes and electric field is applied between the top and bottom electrodes which are separated by an air gap. On application of the electric field, enhancement in the amplitude of capillary waves present on the polymer surface has been observed. The characteristic spacing (λ) of the patterns is given by

$$\lambda = 2\,\pi \left[\frac{\gamma U}{\varepsilon_o \varepsilon_p (\varepsilon_p - 1)^2} \right] E_p^{\frac{-3}{2}} \tag{1.6}$$

where U is the voltage applied, ε_o and is the dielectric constant of free space, ε_p is the relative permittivity of the medium, γ is the surface tension of polymer and E_p is the field strength in the medium.

Similar studies have also been carried out in our laboratory where external electric field was used for studying surface instability and patterning of soft viscoelastic dielectric films. [51-53] Regularly ordered cylindrical pillars of dielectric material could be fabricated by this treatment (shown in Figure 1.11).
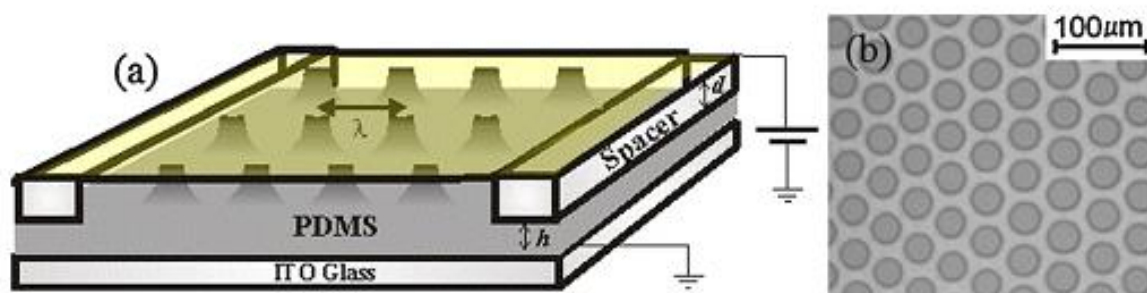
Figure 1.11 *Electro-Hydro-Dynamic Lithography used to create ordered patterning of thin films of PDMS. Patterning is created because of instabilities driven by the competition between electrostatic forces acting on the film and the surface tension of the film. (reproduced with permission from Ref. [53].*

1.6 External electric field assisted thermal annealing treatment

In this thesis, an external electric field-assisted thermal annealing treatment referred to as 'EFTA treatment' is used to control the morphology of BHJ active layers. This treatment is not commonly used for device fabrication. The thesis highlights the utility of this procedure for OSCs. The application of EFTA on spin-coated BHJ films fall under a different class of phenomena. The BHJ films with multiple components do not respond collectively and the large-scale extended electrostatic energy-driven instability pattern is not dominant. The

reorganization and the rearrangement of the microstructure upon EFTA treatment in these asymmetric complex binary systems form the major part of this thesis.

1.6.1 EFTA treatment methodology
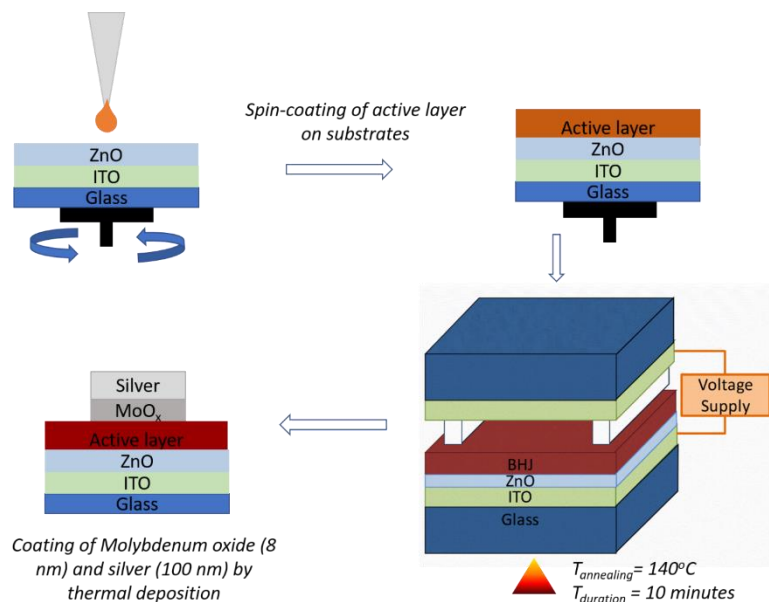
Figure 1.12 *Schematic representation of the methodology of Electric field-assisted thermal annealing (EFTA) treatment.*

The active layer is typically spin-coated on ZnO coated ITO electrodes inside the glove box. Here, ZnO acts as the electron buffer layer. The spin-coated substrate is then immediately taken to a heating stage. A temporary top ITO electrode is brought over the active layer and kept separated by a spacer (≈ 300 μm). Voltage is then applied between the top and bottom electrodes. Thermal annealing for 140 °C for 10 minutes is carried out on the active layer. DC voltage (strength of EF was varied during the treatment) is maintained throughout the thermal annealing process. After the annealing process, the voltage terminals are removed along with the temporary top electrode and spacer. All of these steps are carried out inside the glove box. A permanent top electrode is then deposited by thermal deposition to complete the solar cell device. Schematic representing the EFTA treatment of BHJ films is shown in Figure 1.12.

1.6.2 Review of EFTA treatment in the field of OSCs

Electric field treatment usually during thermal annealing of the active layer and its influence of the morphology have been studied in the literature. A brief summary of some of these results is described below.

In 2003, Sariciftzi and his group applied electric bias during the post-thermal annealing treatment of P3HT: PCBM devices.[54] It was observed that this treatment leads to an enhancement in current density to 8.5 mA cm^{-2}, which consequently improved efficiencies of solar cell devices from 2.5% to 3.5%. Similar treatments on different BHJ solar cell systems where the electric field was applied between electrodes during thermal annealing post device fabrication have been reported.[55, 56]

Cindy X. Zhao et al., applied AC electric field during thermal annealing of P3HT: PCBM BHJ films.[57, 58] The electric field was applied to a floating top electrode and bottom ITO. The electric field was applied by maintaining a voltage of 165 V$_{rms}$ with an air gap of 25 μm. AC frequency was around 10^{-3} Hz. The power conversion efficiencies of the treated solar cell devices increased from 2.89% to 3.14%. They attributed the increase in device performance to better crystalline order in the P3HT domains.

Ching-Fuh Lin et al., reported that efficiency of their P3HT: PCBM solar cell devices increased from 3.16% to 3.51%, when electric field strength of 5.0 x 10^5 V/m was externally applied to the device during the thermal annealing stage.[59] The same group had also reported that the increase in device efficiency was relatively higher when the external electric field was applied in a horizontal direction (in the plane of the active layer) rather than when it was applied vertically (perpendicular to the active layer).[60]

S. Sundar Kumar Iyer and his group studied the effect of external electric field on P3HT: PCBM BHJ solar cells and P3HT pristine films, during thermal annealing.[61, 62] It was observed that the crystalline order of P3HT domains improved in both pristine case and BHJ case with EFTA treatment. This improvement was also reflected in corresponding hole mobility studies and peaks of P3HT polymer in the XRD studies. External Electric field treatment has been shown to improve the device performance of solar cells based on P3HT-nanofibers and PCBM.[63] Effect of external electric field treatment was studied on semi-crystalline and amorphous polymer BHJ systems by Ankur Solanki et. al.[64] Significant changes were observed for semi-crystalline BHJ solar cells (during thermal annealing) while amorphous donor BHJ systems (without thermal annealing) did not show any discernible change with electric field treatment.

Spray deposition is a technique of film casting where the active layer films are formed by spreading of fine droplets of the blend solution and coalescence of the deposited material on the substrate. Electric field assisted spray deposition of BHJ thin films, and buffer layers have

shown improvement when compared to corresponding control devices.[65-67] In this process, an electric field is applied to the spray nozzle through which the deposition is carried out. The improvement in performance was attributed to better crystallinity of the domains, enhanced transport, and reduced recombination at the donor-acceptor interfaces.

Electric field treatment during solvent annealing without thermal annealing has also been found to increase self-organization in P3HT domains, which subsequently improved P3HT: PCBM solar cell device performance.[68] Electric field-assisted thermal annealing has also been studied on P3HT: PCBM BHJ systems with small addition 4-cyano-4'-pentylterphenyl (5CT) liquid crystalline molecules.[69] By carefully optimizing the process parameters, they were able to increase device efficiency compared to control devices.

To control the nanomorphology of P3HT: PCBM BHJ films, wet thin films were exposed to E-field of Van de Graaff (VDG) generator at three different directions -horizontal (H), tilted (T), and vertical (V) relative to the plane of the substrate.[70] Favourable morphologies with efficient charge separation, transport, and collection were obtained by this treatment.

It is to be noted that in most of these studies, EFTA treatment has been largely carried out only on semi-crystalline donor BHJ systems, mainly P3HT: PCBM systems. The observed increase in efficiency parameters was typically attributed to increase in crystalline order in donor domains and corresponding improvement in hole mobility in the active layer. We generalize this approach by applying EFTA to a host of other types of BHJ systems and compare the effects. In this process, we seek to improve the understanding of structure-property correlations in both amorphous and semi-crystalline systems as well as small molecule and macromolecule systems. A major outcome is the demonstration of the possibility of lowering the annealing temperature and improved stability of EFTA systems. A final example of EFTA is also demonstrated for binary mixture films for memory-switch application.

1.7 Thesis Outline and structure

The thesis is organized as follows:

The first part (chapter 2) focuses on EFTA treatment of model organic solar cell system of P3HT: PCBM. The dependence of donor chain length on EFTA treatment was studied by varying the molecular weight of the semi-crystalline donor polymer. EF strength required for optimal solar cell device performance was found to depend on the molecular weight of the donor. The observed EFTA induced improvement in device performance was attributed to

increased hole mobility due to enhanced crystallinity of the donor component and optimal vertical phase segregation of the active layer components.

The third chapter focuses on the extension of EFTA treatment to active layer system of PTB7-Th: PCBM, where PTB7-Th is a prototypical amorphous polymer donor. The presence of residual additives in the active layer leads to a profound effect and is also accompanied by a faster rate of degradation. Controlled Vertical phase segregation of active layer components by EFTA treatment was able to mitigate the efficiency loss incurred by the thermal treatment. This leads to stable solar cell devices with reasonable efficiency parameters.

Chapter 4 focuses on EFTA treatment of active layers of two classes of systems (i) one in which both the donor and acceptor are small molecules (ii) macromolecular donors and non-fullerene acceptors. The results from the systems are examined and compared with the model systems of chapter 2 and 3.

The final part focuses on EFTA treatment on two-component organic memristors. The active layer of organic memristors consisted of semiconducting polymer (PFO or P3HT) channels in a matrix of ferroelectric dielectric polymer (PVDF-TrFE), sandwiched between two electrodes. The memristor action relies on the state of the barriers and transport network via the semiconducting channels, which is controlled by the polarization state of the ferroelectric polymer. EFTA treated devices reveal improvement in the performance parameters over normal control- devices

References

1.   BP Statistical Review of World Energy 2019.

2.   Renewable energy consumption (% of total final energy consumption) | Data". data.worldbank.org.

3.   Adachi, D.; Hernández, J. L.; Yamamoto, K., Impact of carrier recombination on fill factor for large area heterojunction crystalline silicon solar cell with 25.1% efficiency. *Applied Physics Letters* **2015,** *107* (23), 233506.

4.   García-Valverde, R.; Cherni, J. A.; Urbina, A., Life cycle analysis of organic photovoltaic technologies. *Progress in Photovoltaics: Research and Applications* **2010,** *18* (7), 535-558.

5.   Lizin, S.; Van Passel, S.; De Schepper, E.; Maes, W.; Lutsen, L.; Manca, J.; Vanderzande, D., Life cycle analyses of organic photovoltaics: a review. *Energy & Environmental Science* **2013,** *6* (11), 3136-3149.

6.   Abdulrazzaq, O. A.; Saini, V.; Bourdo, S.; Dervishi, E.; Biris, A. S., Organic Solar Cells: A Review of Materials, Limitations, and Possibilities for Improvement. *Particulate Science and Technology* **2013,** *31* (5), 427-442.

7.   Günes, S.; Neugebauer, H.; Sariciftci, N. S., Conjugated Polymer-Based Organic Solar Cells. *Chemical Reviews* **2007,** *107* (4), 1324-1338.

8.   Tang, C. W., Two-layer organic photovoltaic cell. *Applied Physics Letters* **1986,** *48* (2), 183-185.

9.   Forrest, S. R., The Limits to Organic Photovoltaic Cell Efficiency. *MRS Bulletin* **2011,** *30* (1), 28-32.

10.   Yu, G.; Gao, J.; Hummelen, J. C.; Wudl, F.; Heeger, A. J., Polymer Photovoltaic Cells: Enhanced Efficiencies via a Network of Internal Donor-Acceptor Heterojunctions. *Science* **1995,** *270* (5243), 1789.

11.   Xu, X.; Feng, K.; Bi, Z.; Ma, W.; Zhang, G.; Peng, Q., Single-Junction Polymer Solar Cells with 16.35% Efficiency Enabled by a Platinum(II) Complexation Strategy. *Advanced Materials* **2019,** *0* (0), 1901872.

12.   Hou, J.; Inganäs, O.; Friend, R. H.; Gao, F., Organic solar cells based on non-fullerene acceptors. *Nature Materials* **2018,** *17*, 119.

13.   Po, R.; Carbonera, C.; Bernardi, A.; Camaioni, N., The role of buffer layers in polymer solar cells. *Energy & Environmental Science* **2011,** *4* (2), 285-310.

14.   Steim, R.; Kogler, F. R.; Brabec, C. J., Interface materials for organic solar cells. *Journal of Materials Chemistry* **2010,** *20* (13), 2499-2512.

15.   Cheng, P.; Zhan, X., Stability of organic solar cells: challenges and strategies. *Chemical Society Reviews* **2016,** *45* (9), 2544-2582.

16.   Heremans, P.; Cheyns, D.; Rand, B. P., Strategies for Increasing the Efficiency of Heterojunction Organic Solar Cells: Material Selection and Device Architecture. *Accounts of Chemical Research* **2009,** *42* (11), 1740-1747.

17.   Brabec, C. J.; Cravino, A.; Meissner, D.; Sariciftci, N. S.; Fromherz, T.; Rispens, M. T.; Sanchez, L.; Hummelen, J. C., Origin of the Open Circuit Voltage of Plastic Solar Cells. *Advanced Functional Materials* **2001,** *11* (5), 374-380.

18.   Elumalai, N. K.; Uddin, A., Open circuit voltage of organic solar cells: an in-depth review. *Energy & Environmental Science* **2016,** *9* (2), 391-410.

19.   Azzouzi, M.; Kirchartz, T.; Nelson, J., Factors Controlling Open-Circuit Voltage Losses in Organic Solar Cells. *Trends in Chemistry* **2019,** *1* (1), 49-62.

20.   Monestier, F.; Simon, J.-J.; Torchio, P.; Escoubas, L.; Flory, F.; Bailly, S.; de Bettignies, R.; Guillerez, S.; Defranoux, C., Modeling the short-circuit current density of polymer solar cells based on P3HT:PCBM blend. *Solar Energy Materials and Solar Cells* **2007,** *91* (5), 405-410.

21.   Nogueira, A. F.; Montanari, I.; Nelson, J.; Durrant, J. R.; Winder, C.; Sariciftci, N. S.; Brabec, C., Charge Recombination in Conjugated Polymer/Fullerene Blended Films Studied by Transient Absorption Spectroscopy. *The Journal of Physical Chemistry B* **2003,** *107* (7), 1567-1573.

22.   Pivrikas, A.; Sariciftci, N. S.; Juška, G.; Österbacka, R., A review of charge transport and recombination in polymer/fullerene organic solar cells. *Progress in Photovoltaics: Research and Applications* **2007,** *15* (8), 677-696.

23.   Gupta, D.; Mukhopadhyay, S.; Narayan, K. S., Fill factor in organic solar cells. *Solar Energy Materials and Solar Cells* **2010,** *94* (8), 1309-1313.

24.   Qi, B.; Wang, J., Fill factor in organic solar cells. *Physical Chemistry Chemical Physics* **2013,** *15* (23), 8972-8982.

25.   Gupta, D.; Bag, M.; Narayan, K. S., Correlating reduced fill factor in polymer solar cells to contact effects. *Applied Physics Letters* **2008,** *92* (9), 093301.

26.   Pal, S. K.; Kesti, T.; Maiti, M.; Zhang, F.; Inganäs, O.; Hellström, S.; Andersson, M. R.; Oswald, F.; Langa, F.; Österman, T.; Pascher, T.; Yartsev, A.; Sundström, V., Geminate Charge Recombination in Polymer/Fullerene Bulk Heterojunction Films and Implications for Solar Cell Function. *Journal of the American Chemical Society* **2010,** *132* (35), 12440-12451.

27.   Koster, L. J. A.; Mihailetchi, V. D.; Blom, P. W. M., Bimolecular recombination in polymer/fullerene bulk heterojunction solar cells. *Applied Physics Letters* **2006,** *88* (5), 052104.

28.   Huang, Y.; Kramer, E. J.; Heeger, A. J.; Bazan, G. C., Bulk Heterojunction Solar Cells: Morphology and Performance Relationships. *Chemical Reviews* **2014,** *114* (14), 7006-7043.

29.   Chiu, M.-Y.; Jeng, U.-S.; Su, C.-H.; Liang, K. S.; Wei, K.-H., Simultaneous Use of Small- and Wide-Angle X-ray Techniques to Analyze Nanometerscale Phase Separation in Polymer Heterojunction Solar Cells. *Advanced Materials* **2008,** *20* (13), 2573-2578.

30.   Collins, B. A.; Cochran, J. E.; Yan, H.; Gann, E.; Hub, C.; Fink, R.; Wang, C.; Schuettfort, T.; McNeill, C. R.; Chabinyc, M. L.; Ade, H., Polarized X-ray scattering reveals non-crystalline orientational ordering in organic films. *Nature Materials* **2012,** *11*, 536.

31.   Swaraj, S.; Wang, C.; Yan, H.; Watts, B.; Lüning, J.; McNeill, C. R.; Ade, H., Nanomorphology of Bulk Heterojunction Photovoltaic Thin Films Probed with Resonant Soft X-ray Scattering. *Nano Letters* **2010,** *10* (8), 2863-2869.

32.   Kim, Y.; Choulis, S. A.; Nelson, J.; Bradley, D. D. C.; Cook, S.; Durrant, J. R., Device annealing effect in organic solar cells with blends of regioregular poly(3-hexylthiophene) and soluble fullerene. *Applied Physics Letters* **2005,** *86* (6), 063502.

33.   Li, G.; Shrotriya, V.; Huang, J.; Yao, Y.; Moriarty, T.; Emery, K.; Yang, Y., High-efficiency solution processable polymer photovoltaic cells by self-organization of polymer blends. *Nature Materials* **2005,** *4* (11), 864-868.

34.   Agostinelli, T.; Lilliu, S.; Labram, J. G.; Campoy-Quiles, M.; Hampton, M.; Pires, E.; Rawle, J.; Bikondoa, O.; Bradley, D. D. C.; Anthopoulos, T. D.; Nelson, J.; Macdonald, J. E., Real-Time Investigation of Crystallization and Phase-Segregation Dynamics in P3HT:PCBM Solar Cells During Thermal Annealing. *Advanced Functional Materials* **2011,** *21* (9), 1701-1708.

35.   Wu, W.-R.; Jeng, U. S.; Su, C.-J.; Wei, K.-H.; Su, M.-S.; Chiu, M.-Y.; Chen, C.-Y.; Su, W.-B.; Su, C.-H.; Su, A.-C., Competition between Fullerene Aggregation and Poly(3-hexylthiophene) Crystallization upon Annealing of Bulk Heterojunction Solar Cells. *ACS Nano* **2011,** *5* (8), 6233-6243.

36.   Li, G.; Shrotriya, V.; Yao, Y.; Yang, Y., Investigation of annealing effects and film thickness dependence of polymer solar cells based on poly(3-hexylthiophene). *Journal of Applied Physics* **2005,** *98* (4), 043704.

37.   Swinnen, A.; Haeldermans, I.; vande Ven, M.; D'Haen, J.; Vanhoyland, G.; Aresu, S.; D'Olieslaeger, M.; Manca, J., Tuning the Dimensions of C60-Based Needlelike Crystals in Blended Thin Films. *Advanced Functional Materials* **2006,** *16* (6), 760-765.

38.   Li, G.; Yao, Y.; Yang, H.; Shrotriya, V.; Yang, G.; Yang, Y., "Solvent Annealing" Effect in Polymer Solar Cells Based on Poly(3-hexylthiophene) and Methanofullerenes. *Advanced Functional Materials* **2007,** *17* (10), 1636-1644.

39.   Li, G.; Shrotriya, V.; Yao, Y.; Huang, J.; Yang, Y., Manipulating regioregular poly(3-hexylthiophene) : [6,6]-phenyl-C61-butyric acid methyl ester blends—route towards high efficiency polymer solar cells. *Journal of Materials Chemistry* **2007,** *17* (30), 3126-3140.

40.   Li, M.; Liu, F.; Wan, X.; Ni, W.; Kan, B.; Feng, H.; Zhang, Q.; Yang, X.; Wang, Y.; Zhang, Y.; Shen, Y.; Russell, T. P.; Chen, Y., Subtle Balance Between Length Scale of Phase Separation and Domain Purification in Small-Molecule Bulk-Heterojunction Blends under Solvent Vapor Treatment. *Advanced Materials* **2015,** *27* (40), 6296-6302.

41.   Tang, H.; Lu, G.; Li, L.; Li, J.; Wang, Y.; Yang, X., Precise construction of PCBM aggregates for polymer solar cells via multi-step controlled solvent vapor annealing. *Journal of Materials Chemistry* **2010,** *20* (4), 683-688.

42.   Liu, J.; Chen, L.; Gao, B.; Cao, X.; Han, Y.; Xie, Z.; Wang, L., Constructing the nanointerpenetrating structure of PCDTBT:PC70BM bulk heterojunction solar cells induced by aggregation of PC70BM via mixed-solvent vapor annealing. *Journal of Materials Chemistry A* **2013,** *1* (20), 6216-6225.

43.   Lee, J. K.; Ma, W. L.; Brabec, C. J.; Yuen, J.; Moon, J. S.; Kim, J. Y.; Lee, K.; Bazan, G. C.; Heeger, A. J., Processing Additives for Improved Efficiency from Bulk Heterojunction Solar Cells. *Journal of the American Chemical Society* **2008,** *130* (11), 3619-3623.

44.   Lou, S. J.; Szarko, J. M.; Xu, T.; Yu, L.; Marks, T. J.; Chen, L. X., Effects of Additives on the Morphology of Solution Phase Aggregates Formed by Active Layer Components of High-Efficiency Organic Solar Cells. *Journal of the American Chemical Society* **2011,** *133* (51), 20661-20663.

45.   Xiao, Z.; Yuan, Y.; Yang, B.; VanDerslice, J.; Chen, J.; Dyck, O.; Duscher, G.; Huang, J., Universal Formation of Compositionally Graded Bulk Heterojunction for Efficiency Enhancement in Organic Photovoltaics. *Advanced Materials* **2014,** *26* (19), 3068-3075.

46.   Kim, M.; Lee, J.; Jo, S. B.; Sin, D. H.; Ko, H.; Lee, H.; Lee, S. G.; Cho, K., Critical factors governing vertical phase separation in polymer–PCBM blend films for organic solar cells. *Journal of Materials Chemistry A* **2016,** *4* (40), 15522-15535.

47.   Schäffer, E.; Thurn-Albrecht, T.; Russell, T. P.; Steiner, U., Electrically induced structure formation and pattern transfer. *Nature* **2000,** *403* (6772), 874-877.

48.   Lin, Z.; Kerle, T.; Russell, T. P.; Schäffer, E.; Steiner, U., Structure Formation at the Interface of Liquid/Liquid Bilayer in Electric Field. *Macromolecules* **2002,** *35* (10), 3971-3976.

49.   Lin, Z.; Kerle, T.; Russell, T. P.; Schäffer, E.; Steiner, U., Electric Field Induced Dewetting at Polymer/Polymer Interfaces. *Macromolecules* **2002,** *35* (16), 6255-6262.

50.   Xu, T.; Zhu, Y.; Gido, S. P.; Russell, T. P., Electric Field Alignment of Symmetric Diblock Copolymer Thin Films. *Macromolecules* **2004,** *37* (7), 2625-2629.

51.   Arun, N.; Sharma, A.; Shenoy, V. B.; Narayan, K. S., Electric-Field-Controlled Surface Instabilities in Soft Elastic Films. *Advanced Materials* **2006,** *18* (5), 660-663.

52.   Arun, N.; Sarkar, J.; Sharma, A.; Shenoy, V. B.; Narayan, K. S., Electric-Field Induced Morphological Transitions in Elastic Contact Instability of Soft Solid Films. *The Journal of Adhesion* **2007,** *83* (6), 513-534.

53.   Arun, N.; Sharma, A.; Pattader, P. S. G.; Banerjee, I.; Dixit, H. M.; Narayan, K. S., Electric-Field-Induced Patterns in Soft Viscoelastic Films: From Long Waves of Viscous Liquids to Short Waves of Elastic Solids. *Physical Review Letters* **2009,** *102* (25), 254502.

54.   Padinger, F.; Rittberger, R. S.; Sariciftci, N. S., Effects of Postproduction Treatment on Plastic Solar Cells. *Advanced Functional Materials* **2003,** *13* (1), 85-88.

55.   Pandey, A. K.; Nunzi, J. M.; Wang, H.; Oey, C. C.; Djurišić, A. B.; Xie, M. H.; Leung, Y. H.; Man, K. K. Y.; Chan, W. K., Reverse biased annealing: Effective post treatment tool for polymer/nano-composite solar cells. *Organic Electronics* **2007,** *8* (4), 396-400.

56.   Li, Y.; Hou, Y.; Wang, Y.; Feng, Z.; Feng, B.; Qin, L.; Teng, F., Thermal treatment under reverse bias: Effective tool for polymer/fullerene bulk heterojunction solar cells. *Synthetic Metals* **2008,** *158* (5), 190-193.

57.   Zhao, C. X.; Wang, K.; Britten, J. F.; Zhi, M.; Wang, X.; Chen, Z. K.; Xu, G., Dual nanostructures in poly (3-hexylthiophene) based organic photovoltaics under alternative current electric field. *Thin Solid Films* **2012,** *520* (17), 5770-5774.

58.   Zhao, C. X.; Wang, X.; Zeng, W.; Chen, Z. K.; Ong, B. S.; Wang, K.; Deng, L.; Xu, G., Organic photovoltaic power conversion efficiency improved by AC electric field alignment during fabrication. *Applied Physics Letters* **2011,** *99* (5), 053305.

59.   Ma, S.-Y.; Shen, Y.-M.; Yang, P.-C.; Chen, C.-S.; Lin, C.-F., Morphological modification induced by external electric field during solution process of organic solar cells. *Organic Electronics* **2012,** *13* (2), 297-301.

60.   Shen, Y.-M.; Chen, C.-S.; Yang, P.-C.; Ma, S.-Y.; Lin, C.-F., Improvement of surface morphology of thin films and performance by applying electric field on P3HT:PCBM based solar cells. *Solar Energy Materials and Solar Cells* **2012,** *99*, 263-267.

61.   Bagui, A.; Iyer, S. S. K., Effect of Solvent Annealing in the Presence of Electric Field on P3HT:PCBM Films Used in Organic Solar Cells. *IEEE Transactions on Electron Devices* **2011,** *58* (11), 4061-4066.

62.   Bagui, A.; Iyer, S. S. K. In *Improvement of morphological and electrical properties in poly (3-hexylthiophene-2, 5-diyl) Films Formed by Thermal Annealing in the presence of*

electric field during the solvent drying step, 2012 38th IEEE Photovoltaic Specialists Conference, 3-8 June 2012; 2012; pp 002301-002305.

63. Solanki, A.; Wu, B.; Salim, T.; Yeow, E. K. L.; Lam, Y. M.; Sum, T. C., Performance Improvements in Polymer Nanofiber/Fullerene Solar Cells with External Electric Field Treatment. *The Journal of Physical Chemistry C* **2014,** *118* (21), 11285-11291.

64. Solanki, A.; Bagui, A.; Long, G.; Wu, B.; Salim, T.; Chen, Y.; Lam, Y. M.; Sum, T. C., Effectiveness of External Electric Field Treatment of Conjugated Polymers in Bulk-Heterojunction Solar Cells. *ACS Applied Materials & Interfaces* **2016,** *8* (47), 32282-32291.

65. Chaturvedi, N.; Swami, S. K.; Dutta, V., Spray deposition of poly(3-hexylthiophene) and [6,6]-phenyl-C61-butyric acid methyl ester blend under electric field for improved interface and organic solar cell characteristics. *Thin Solid Films* **2016,** *598*, 82-87.

66. Mohammad, T.; Bharti, V.; Kumar, V.; Mudgal, S.; Dutta, V., Spray coated europium doped PEDOT:PSS anode buffer layer for organic solar cell: The role of electric field during deposition. *Organic Electronics* **2019,** *66*, 242-248.

67. Chaturvedi, N.; Swami, S. K.; Dutta, V., Electric field assisted spray deposited MoO3 thin films as a hole transport layer for organic solar cells. *Solar Energy* **2016,** *137*, 379-384.

68. Lin, C.-C.; Lin, Y.-Y.; Li, S.-S.; Yu, C.-C.; Huang, C.-L.; Lee, S.-H.; Du, C.-H.; Lee, J.-J.; Chen, H.-L.; Chen, C.-W., Electric field-assisted self-organization of polymer:fullerene hybrids on the photovoltaic performance. *Energy & Environmental Science* **2011,** *4* (6), 2134-2139.

69. Zhou, W.; Shi, J.; Lv, L.; Chen, L.; Chen, Y., A mechanistic investigation of morphology evolution in P3HT–PCBM films induced by liquid crystalline molecules under external electric field. *Physical Chemistry Chemical Physics* **2015,** *17* (1), 387-397.

70. Elshobaki, M.; Gebhardt, R.; Carr, J.; Lindemann, W.; Wang, W.; Grieser, E.; Venkatesan, S.; Ngo, E.; Bhattacharjee, U.; Strzalka, J.; Jiang, Z.; Qiao, Q.; Petrich, J.; Vaknin, D.; Chaudhary, S., Tailoring Nanoscale Morphology of Polymer:Fullerene Blends Using Electrostatic Field. *ACS Applied Materials & Interfaces* **2017,** *9* (3), 2678-2685.

Chapter 2

Electric Field Assisted Thermal Annealing Treatment of Semi-Crystalline Polymer: Fullerene-Based Solar Cell Devices

2.1 Introduction

2.1.1 Active layer

P3HT (poly(3-hexylthiophene)) is a semi-crystalline polymer donor and $PC_{70}BM$ (phenyl-C_{71}-butyric acid methyl ester) is a small molecule acceptor. Bulk heterojunction (BHJ) blends of P3HT: $PC_{70}BM$ have been extensively studied as a model binary system. The device performance-microstructure correlations of this BHJ blend is well understood in the literature.[1-5] The active layer of P3HT: $PC_{70}BM$ blend film is generally modelled in terms of a three-phase morphology, with donor-pure regions, acceptor-pure regions, and amorphous regions of intermixed donor and acceptor components.[6-8] Donor-acceptor interface junctions, which acts as carrier generation sites, are more in the intermixed amorphous regions. However, charge extraction from these regions is limited by non-geminate recombination owing to insufficient percolated pathways for separated charge carriers. The relative fractions of these three phases in the active layer dictate the performance of solar cells fabricated, and it is found to be critically dependent on the processing conditions. When P3HT: $PC_{70}BM$ blend is spin-coated from the native solvent of chlorobenzene or dichlorobenzene, it is observed that it leads to larger proportions of amorphous content in the active layer; hence the solar cells fabricated without any treatments are inefficient.
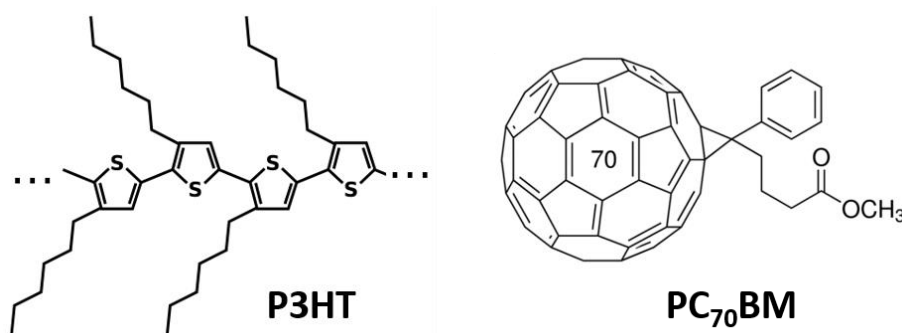
Figure 2.1 *Molecular structures of P3HT polymer donor and $PC_{70}BM$ small molecule acceptor*

Thermal annealing treatment has been used to improve the performance of P3HT: $PC_{70}BM$ BHJ solar cells. By careful tuning of the thermal annealing treatment parameters, the fraction of ordered regions can be optimized to improve the solar cell device performance.[9-13] Improvement in ordering due to thermal treatment is reflected in better crystalline peaks in XRD studies and mobility studies.

Using additives like Di-iodo-octane (DIO) along with the native solvent have also shown to improve the morphology of active layer and enhance subsequent device performance.[14, 15] Additive solvents have been found to selectively dissolve $PC_{70}BM$ acceptor molecules and it stays longer in the film due to their very low vapour pressure.[16] This allows active layer components to redistribute into a morphology favourable for enhanced device performance.

The molecular weight of the polymer donor also plays a role in deciding the initial state of the active layer. As the molecular weight of the polymer is increased, the fraction of amorphous content is found to increase in the active layer.[17, 18] This is because inertial forces and conformational constraints of the polymer increases with the donor chain length.[19] Solar cell devices fabricated from BHJ with higher molecular weight P3HT have shown to be less efficient because of the resultant lower crystalline donor in the polymer regions. Thermal annealing conditions required to optimize the morphology favourable for optimum device performance is also dependent on the molecular weight of the polymer.[20]

2.2 Dependence of the molecular weight of the polymer donor on the effectiveness of EFTA treatment
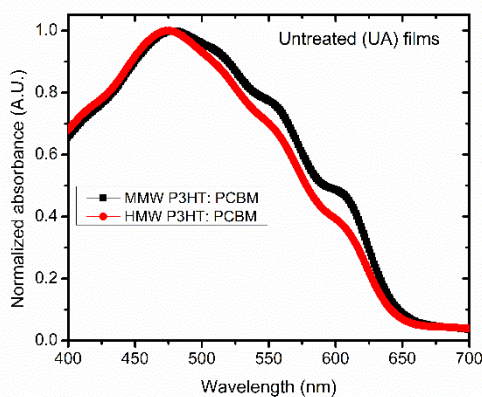
Figure 2.2 *Normalized absorbance spectra of Untreated (UA) films of MMW-P3HT: $PC_{70}BM$ and HMW-P3HT: $PC_{70}BM$ BHJ films. The thickness of the films was ≈ 200 nm. Tthe films were coated on glass substrates for absorption studies. Absorption studies of thin films were carried out using Perkin Elmer UV/Vis/NIR Lambda 750 Spectrometer.*

In this part of the chapter, the effectiveness of EFTA treatment on the P3HT: $PC_{70}BM$ BHJ system was studied by varying the molecular weight of the P3HT molecule. This study is aimed at understanding how different initial states (different fractions of amorphous content) of the same BHJ system responds to the EFTA treatment.

Medium molecular weight (MMW)-P3HT of 45 kDa and high molecular weight (HMW)-P3HT of 88 kDa were used in the study. High-Molecular weight P3HT was obtained from Prof. Anil Kumar at IIT-Bombay (Sycon Polymers India Pvt. Ltd.). P3HT polymer of varying molecular weights are available from the Sycon Polymers India Pvt. Ltd. MMW-P3HT. $PC_{70}BM$ molecules were purchased from Luminescence Technology Corp., Taiwan.

BHJ blend solutions were fabricated with the donor: acceptor in the ratio 1:1 with dichlorobenzene solvent. The 28 mg/ml solution was kept stirring at 55 °C for more than 8 hours. The blend solutions were spin-coated at 700 rpm for 1 minute on substrates when the solution was at room temperature (30 °C) in inert conditions. ITO- substrates and ZnO-coated ITO substrates were used depending on the requirement, with the latter case for the fabrication of inverted solar cells.

Higher amorphous content in the HMW-P3HT BHJ film than the MMW-P3HT BHJ films can be observed in the blue-shifted absorption spectra of the HMW-P3HT BHJ film when compared to the MMW-P3HT system for Untreated samples (as shown in Figure 2.2).

2.2.1 EFTA treatment

Thermal annealing conditions during EFTA treatment was maintained same for both the BHJ systems (130 °C for 10 minutes). The strength of the EF applied during the treatment by varying the voltage maintained between the top and bottom electrodes. Voltage values of 8, 40, and 200 V maintained with an air gap of 200 μm yield EF strengths of 4×10^2, 2×10^3, and 1×10^4 V/cm, respectively. The voltage was applied using Keithley 248 High Voltage power supply. The treated samples are correspondingly denoted as low-EF, med-EF, and high-EF, respectively. Only-thermally annealed devices are denoted as zero-EF or TA devices. The direction of EF during the treatment was maintained such that the positive terminal is connected to the bottom electrode and the top electrode was left grounded.

Morphological variations induced by the external EFTA treatment on the active layer is followed by studying absorption spectra, mobility studies in the blend film, X-ray characterisation, AFM imaging of the film. The solar cell devices fabricated after EFTA treatment reflects how the EFTA treatment alters the resultant device performance.

2.2.2 Absorption studies

Structural reorganization in the BHJ films upon EFTA treatment was probed by analysing the absorption spectra. Absorption spectra give insight into the degree of orientation and

crystallinity in P3HT.[21, 22] Absorption spectra of the EFTA treated and control BHJ blend thin films are shown for both MMW P3HT: PC$_{70}$BM and HMW-P3HT: PC$_{70}$BM in Figure 2.3 respectively, as a function of the strength of EF, applied during the treatment. Control Untreated (UA) films show more blue-shifted spectra, which shows that there is larger amorphous content in the active layer. The absorption spectra of TA and EFTA treated active layer films is more red-shifted than the control UA films.
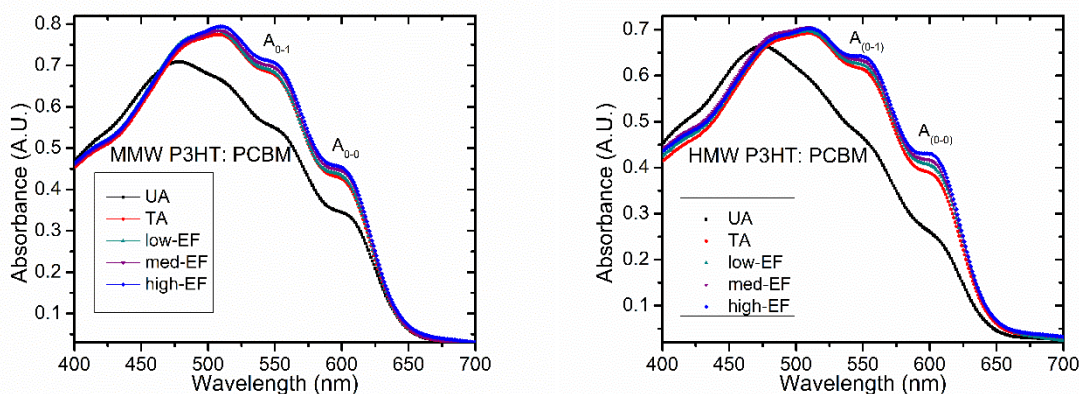
Figure 2.3 *Absorbance spectra of MMW-P3HT: PC$_{70}$BM and HMW-P3HT: PC$_{70}$BM BHJ films as a function of EFTA treatment. UA and TA correspond to Untreated and Thermally annealed control films, respectively. low-EF, med-EF, and high-EF correspond to EFTA treated films with EF strengths 4 × 10^2 V/cm, 2 × 10^3 V/cm, and 1 × 10^4 V/cm respectively. The thickness of the films was close to 200 nm. All the films were coated on ITO substrates for absorption studies. Absorption studies of thin films were carried out using Perkin Elmer UV/Vis/NIR Lambda 750 Spectrometer.*

The intensity of peak around 600 nm is found to increase in intensity as the strength of the electric field was increased during the treatment. This peak at 600 nm corresponds to alkyl chain interaction between P3HT polymer molecules. This observation implies that there is a definite increase in interaction between P3HT molecules with EFTA treatment.

From the intensities of peaks around 600 nm (2 eV) and 550 nm (2.25 eV) referred to A$_{0-0}$ and A$_{0-1}$ respectively, exciton bandwidth (W) can be extracted from the following equation developed by Spano for P3HT chains,[23] with the assumption that the Huang−Rhys parameter is unity.

$$\frac{A_{0-0}}{A_{0-1}} \cong \frac{1-0.24\frac{W}{\hbar\omega_o}}{1+0.073\frac{W}{\hbar\omega_o}} \tag{2.1}$$

Huang-Rhys parameter (S) is commonly used to characterize linear vibrational coupling to electronic excitations through the difference between ground and excited state geometries.[24] The Huang-Rhys factor can be related to the displacement between the minimum energy positions of harmonic vibrational potentials associated with ground and excited electronic states by the expression, $S = \Delta^2/2$, where Δ is a dimensionless displacement expressed in units of $(h/\mu\omega)^{1/2}$, with μ being the reduced mass of the vibrational coordinate. S characterizes the strength of exciton-vibration coupling.
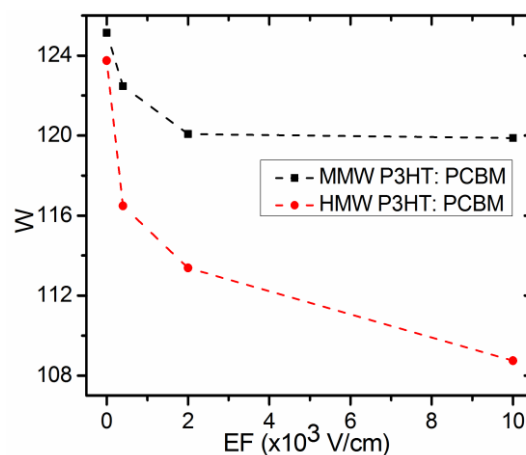
Figure 2.4 *Exciton bandwidths (W) estimated from eq.2.1 as a function of EF strength maintained during EFTA treatment for both the BHJ systems.*

In equation 2.1, $h\omega_0 = 180$ meV is the effective energy of the main intermolecular vibrational modes coupled to the electronic transitions. W has been shown to inversely proportional to the conjugation length in the P3HT polymer chains.[25, 26] In Figure 2.4, exciton bandwidth obtained as the absorption spectra are plotted as a function of the strength of electric field applied during the treatment. It can be observed that W reduces with EF strength for both the MMW-P3HT: $PC_{70}BM$ and HMW-P3HT: $PC_{70}BM$ BHJ systems. For MMW-P3HT: $PC_{70}BM$, W obtained for TA treatment was ~ 125 meV. The value of W progressively reduces with increasing EF strengths and saturates at higher EF strengths. But for HMW-P3HT: $PC_{70}BM$, W value continuously keeps reducing as the strength of EF was increased during the treatment. This observation implies that the conjugation length of donor domains increases in the active layer film with EFTA treatment.

2.2.3 Hole mobility studies

The increase in conjugation length in the donor domains was further probed by hole mobility studies. The mobility studies cab be estimated by different methods, including space-charge-

limited current (SCLC), Charge Extraction by Linearly Increasing Voltage (CELIV), time of flight (ToF), etc. Hole mobility was studied by dark MIS-CELIV technique systematically as a function of processing conditions. MIS-CELIV technique extracts the unipolar charge carrier mobility in a metal-insulator-semiconductor structure and is more accurate than conventional techniques like SCLC and TOF mobility studies and utilizes films of thickness as used for solar cell studies.[27]
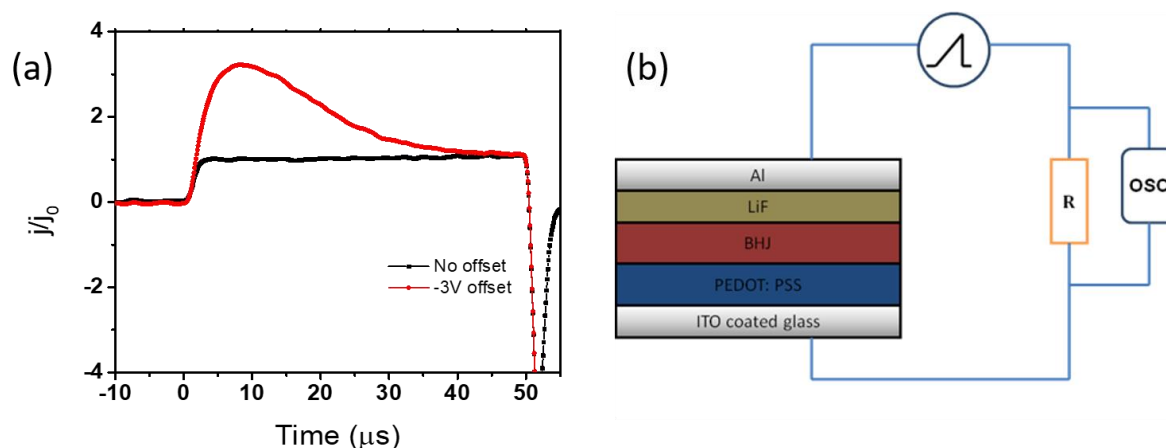
Figure 2.5 *a) MIS-CELIV output profile under negative offset and no offset conditions. b) Experimental setup for CELIV studies (the layers are not drawn to scale). A Tektronix 1022 Arbitary function generator was programmed to generate a CELIV ramp pulse with adjustable slope and offset. A LeCroy Waverunner digital storage oscilloscope A6100 was used to record the response signal.*

The BHJ film was sandwiched between hole-injecting ITO/PEDOT: PSS (40 nm) electrode and hole-blocking lithium fluoride (100 nm)/ Aluminium (100 nm) electrode. Pre-cleaned and patterned ITO substrates were spin-coated with PEDOT-PSS (obtained from Ossila Limited) at 4500 rpm and annealed at 120˚C for 1 hour. BHJ spin-coating was carried out as described earlier inside the glove box. Lithium fluoride and aluminium was thermally evaporated at 10^{-6} mbar base pressure on control and EFTA treated BHJ films. The experimental setup is shown in Figure 2.5b.

When an offset voltage is applied, holes are injected into the semiconductor layer. If the capacity of the insulator is higher than the capacity of the semiconductor, the injected charges get accumulated at the semiconductor-dielectric interface. A reverse linear sweep of the voltage V with slope A = dV/dt results in extraction of the accumulated charges. The current increases

(Δj(t)) from its displacement value (j_o) till the transit time (t_{tr}) of the charges according to the form:

$$\frac{\Delta j(t)}{j_o} = tan^2\left(\frac{t}{t_{tr}}\right) \tag{2.2}$$

Current output was a function of time is shown in Figure 2.5a. From the transit time t_{tr}, the mobility μ can be calculated using the equation,

$$t_{tr} = d_s\sqrt{\frac{\mu}{2A}\left(1 + \frac{\varepsilon_s d_i}{\varepsilon_i d_s}\right)} \tag{2.3}$$

Here, d_i and d_s are the thickness of the insulator and semiconductor, respectively. ε_i and ε_s are the respective dielectric constants.

Table 2.1: *Hole Mobilities Extracted from dark-MIS-CELIV studies on BHJ blends of MMW-P3HT: PC$_{70}$BM and HMW-P3HT: PC$_{70}$BM as a function of EFTA treatment. TA corresponds to Thermally annealed control devices. low-EF, med-EF, and high-EF correspond to EFTA treated devices with EF strengths 4×10^2 V/cm, 2×10^3 V/cm, and 1×10^4 V/cm, respectively.*

Hole mobility (cm^2/Vs)	MMW P3HT: PC$_{70}$BM	HMW P3HT: PC$_{70}$BM
TA	$3.23\pm0.56 \times 10^{-5}$	$5.46\pm0.65 \times 10^{-6}$
low-EF	$3.94\pm0.27 \times 10^{-5}$	$1.30\pm0.34 \times 10^{-5}$
med-EF	$1.31\pm0.33 \times 10^{-4}$	$5.50\pm0.52 \times 10^{-5}$
high-EF	$1.44\pm0.31 \times 10^{-4}$	$1.40\pm0.45 \times 10^{-5}$

Hole mobility (μ_h) obtained from several devices (>10 for each case) for both the BHJ systems is shown in Table 2.1 as a function of EFTA treatment. In case of the thermally annealed devices (TA) these studies point to higher μ_h for MMW P3HT based blend films ($\approx 3.2 \times 10^{-5}$ cm^2/Vs) compared to HMW-P3HT case ($\approx 5.4 \times 10^{-6}$ cm2/Vs) in spite of the higher effective conjugation length prevailing in the HMW systems as observed in the absorption studies. These results indicate the presence of larger amorphous content in the HMW-P3HT BHJ film which offers a higher barrier for charge transport in the BHJ.

For both the BHJ systems, hole mobilities of EFTA treated devices are found to increase when compared to control TA devices. For MMW-P3HT: PC$_{70}$BM hole-only BHJ devices, hole mobilities keeps on increasing as the strength of EF was increased during the EF treatment. For

HMW-P3HT: $PC_{70}BM$, hole mobilities initially increases as strength is increased, but hole mobilities reduce at higher EF strengths maintained during EFTA treatment. This mobility trend further provides validation to the enhanced wavefunction overlap and conjugation length for charge carriers upon EF treatment of BHJ films, as seen from the absorption studies

2.2.4 Atomic Force Microscopy (AFM) imaging

The change in the microstructure in bulk due to EFTA treatment is expected to cause significant changes in the air-BHJ interface of the active layer. This was suitably characterized by AFM imaging for both the BHJ systems, shown in Figure 2.6. Topography images reveal that the surface roughness of the thin films does not show discernible change with EFTA treatment. However, the phase images indicate that for both the BHJ systems, there is a significant increase in the domain size with EFTA treatment when compared with the control TA films, with the largest variations observed in the HMW P3HT: PCBM BHJ thin films. The observed domains are expected to be due to the polymer donor owing its semi-crystalline nature. This variation has been estimated in section 2.3.3.
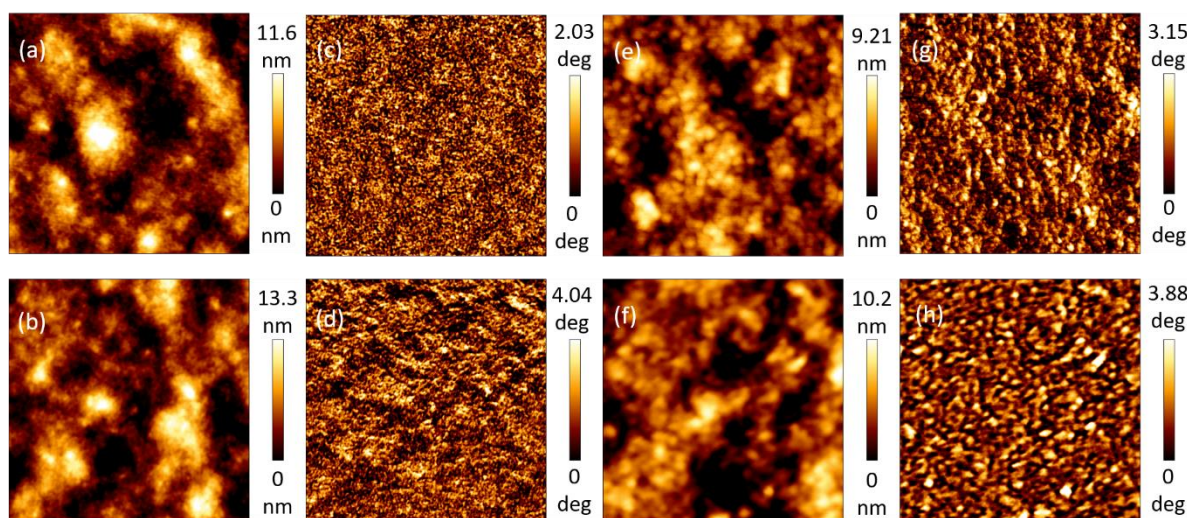
Figure 2.6 *Typical 3 μm × 3 μm AFM Topography (a,b,e,f) and corresponding phase (b,d,g.h) images of TA (a,c) and EFTA (b, d) -treated MMW P3HT: $PC_{70}BM$ BHJ films; TA (e, g) and EFTA (f, h) -treated HMW P3HT: $PC_{70}BM$ BHJ films. EF strength $\cong 1 \times 10^4$ V/cm during the EFTA treatment. For surface imaging, JPK Instruments (Nanowizard 3) AFM was used. The AFM head was mounted on an inverted microscope (Carl-Zeiss). Feedback is controlled using Four-Quadrant position detector measuring the deflection of the 810 nm laser from the AFM cantilever as the tip scans over the surface. Budget sensor silicon AFM tips coated with gold*

coating with resonance frequency 300 kHz and force constant 40 N/m was used in tapping-mode for the study.

2.2.5 GIWAXS studies

X-ray analysis of the degree of ordering in P3HT chains in the active layer has been correlated to the parameters of device performance.[28-31] The increase in crystallinity of P3HT domains was considered as the main reason for the increase in device efficiency for the EFTA treated P3HT: $PC_{70}BM$ solar cells in the earlier studies. The increase in crystallinity of polymer donor was studied by carrying out GIWAXS studies on EFTA treated and control BHJ films. The bulk of the thin films was probed by X-ray by having an angle of incidence ($\alpha_i = 0.5°$) higher than the critical angle ($\alpha_c = 0.12°$). The Out-of-Plane GIWAXS spectra obtained for both BHJ systems is shown as a function of EFTA treatment in Figure 2.7. The peaks around 2θ values of 5.4°, 10.7° and 16° correspond to (100), (200) and (300) peaks of P3HT chains respectively. By Voigt-fitting of (100) peaks of P3HT, domain sizes were estimated by Scherrer's equation. The domain sizes increased from 14 nm (TA) to 16 nm (EFTA) for MMW-P3HT: $PC_{70}BM$. For HMW-P3HT: $PC_{70}BM$ domain sizes increased from 12 nm to 14 nm, respectively. The edge-on orientation of the P3HT chains in the active layer favoured during thermal annealing is found to improve with EFTA treatment.[4, 9]
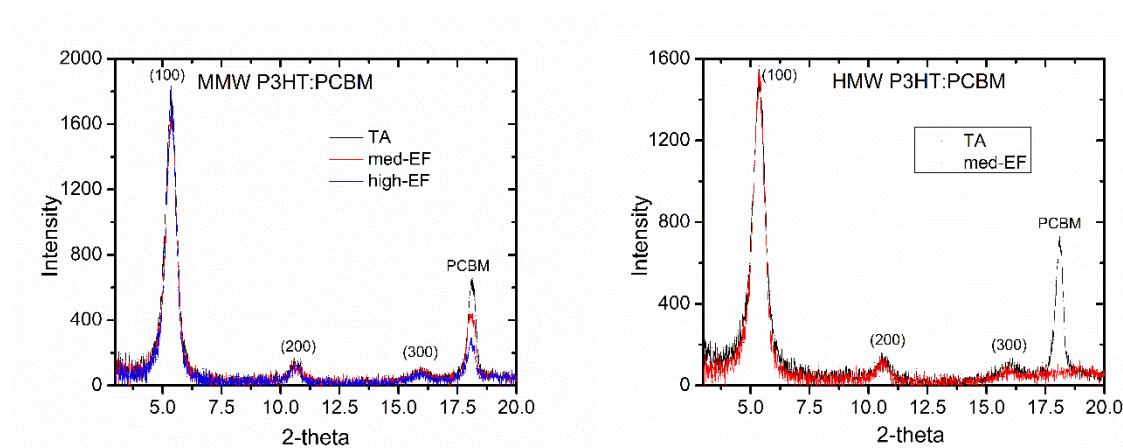
Figure 2.7 *GIWAXS OOP-spectra of (a) MMW P3HT: $PC_{70}BM$ and (b) HMW P3HT: $PC_{70}BM$ BHJ thin films. TA corresponds to Thermally annealed control. med-EF and high-EF correspond to EFTA treated films with EF strengths 2×10^3 V/cm and 1×10^4 V/cm respectively. Out-of-Plane GIWAXS patterns were obtained using Rigaku SmartLab X-Ray Diffractometer system at Centre for Nano Science and Engineering (CeNSE), Indian Institute of Sciences.*

It was noticed that the intensity of $PC_{70}BM$ around 2θ of 18° reduces in magnitude as the strength was increased during the EFTA treatment for both the BHJ systems. The change in intensity was very drastic for HMW-P3HT: $PC_{70}BM$ where $PC_{70}BM$ peak completely reduced even for very low EF strengths maintained during EFTA treatment.

2.2.6 Vertical phase segregation

From the reduction in the intensity of $PC_{70}BM$ peak, it can be inferred that the average distribution of $PC_{70}BM$ molecules are translated to the bottom of the active layer, close to the ZnO-BHJ interface. It is also observed that this redistribution is dependent on the strength of the EF and the molecular weight of the donor, with redistribution more prominent in the case of higher EF strengths during EFTA treatment and higher molecular weight of the polymer. This vertical phase segregation is advantageous for solar cells of Inverted device architecture since $PC_{70}BM$ moving to the bottom of the film will improve the charge collection efficiency at the ZnO interface which acts as the electron-collecting buffer layer. But beyond a threshold, it will be detrimental since the charge generation efficiency will be hampered as $PC_{70}BM$ moving to the bottom of the film will reduce the total Donor-Acceptor interfaces.

2.2.7 Solar cell characteristics
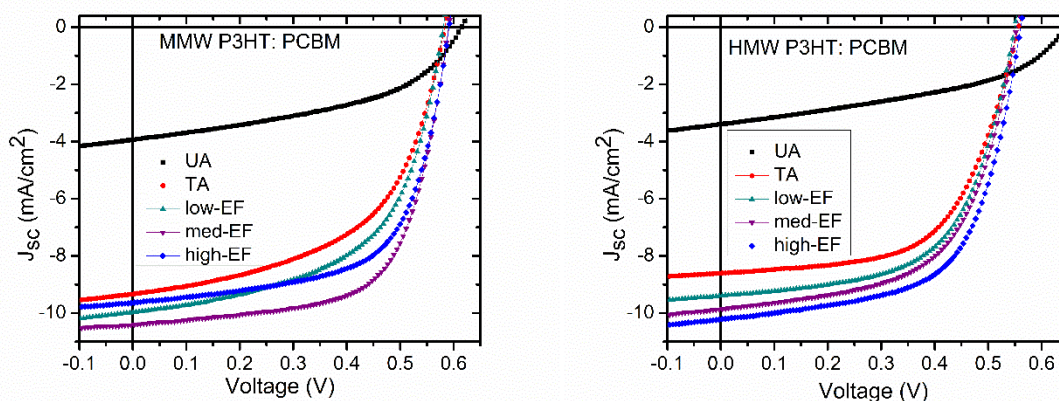
Figure 2.8 *Typical solar cell characteristics of (a) MMW P3HT: $PC_{70}BM$ and (b) HMW P3HT: $PC_{70}BM$ BHJ solar cells under 1 sun illumination. UA and TA correspond to Untreated and Thermally annealed control devices, respectively. low-EF, med-EF, and high-EF correspond to EFTA treated devices with EF strengths 4×10^2 V/cm, 2×10^3 V/cm and 1×10^4 V/cm respectively. Solar cell measurements were carried out using Newport class AAA solar simulator and Source Meter (Keithley 2420) interfaced with data acquisition software (Oriel Instruments I-V test station).*

Pre-cleaned and patterned ITO substrates were spin-coated with zinc oxide (ZnO) nanoparticle dispersion (purchased from Sigma Aldrich) in ethanol. Thermal annealing of ZnO layer was done at 120˚C for half an hour. The active layer was then spin-coated inside a nitrogen-rich glove-box on the ZnO coated ITO substrates. It was followed by thermal annealing or EFTA treatments as described earlier. The devices (electrode area $\approx$ 7 mm^2) were completed by thermal evaporation of 8 nm of molybdenum oxide and 100 nm of silver.

Solar cell characteristics were obtained for EFTA treated and control BHJ devices. Typical J-V characteristics under 1 sun illumination (AM1.5 standard 100 mW/cm^2) is shown in Figure 2.8. Statistics from a large set of data (>10 devices of each case) is shown in Table 2.2.

Table 2.2 *Solar cell parameters obtained from J−V Characteristics measured under 1 Sun light Illumination for MMW-P3HT: PC$_{70}$BM and HMW-P3HT: PC$_{70}$BM devices. UA and TA correspond to Untreated and Thermally annealed control devices, respectively. low-EF, med-EF, and high-EF correspond to EFTA treated devices with EF strengths 4 × 10^2 V/cm, 2 × 10^3 V/cm and 1 × 10^4 V/cm respectively.*

		V_{oc} (V)	J_{sc} (mA/cm^2)	Fill Factor (%)	Efficiency (%)
MMW P3HT: PC$_{70}$BM	UA	0.60±0.01	4.11±0.50	42.56±1.94	1.05±0.12
	TA	0.57±0.01	9.53±0.16	57.01±3.37	3.09±0.13
	low-EF	0.56±0.01	9.95±0.39	57.83±2.45	3.25±0.20
	med-EF	0.58±0.01	10.25±0.33	63.77±0.60	3.78±0.11
	high-EF	0.59±0.01	9.64±0.32	61.43±0.94	3.49±0.16
HMW P3HT: PC$_{70}$BM	UA	0.62±0.01	3.01±0.65	43.30±2.01	0.81±0.18
	TA	0.55±0.01	8.44±0.20	57.37±1.43	2.69±0.11
	low-EF	0.56±0.01	9.48±0.28	56.05±1.76	2.98±0.13
	med-EF	0.56±0.01	9.65±0.16	58.51±1.22	3.19±0.07
	high-EF	0.56±0.01	10.12±0.27	58.55±1.91	3.32±0.15

The following are the main results inferred from the solar cell characteristics.

i. For EFTA treated devices, the device efficiency increases for both the BHJ systems when compared to control thermally annealed devices: 17% increase (3.6% to 4.2%) for MMW-P3HT: PC$_{70}$BM OSCs and 20% increase (2.7% to 3.3%) for HMW-P3HT: PC$_{70}$BM OSCs.

ii.   Largest variations are observed in J_{sc} of the devices, which is reflected in the efficiency parameters.

iii. For MMW-P3HT: $PC_{70}BM$ devices, there is a critical threshold of EF strength above which the EFTA treatment becomes detrimental. For the HMW-P3HT: $PC_{70}BM$ solar cells, the efficiency of the solar cells keeps on increasing as the strength of EF was increased, in the range of EF strength studied. This reduction at higher EF strengths during EFTA treatment for MMW-P3HT: $PC_{70}BM$ OSCs could be due to reduced percolation pathways for the separated charge carriers due to unfavourable phase separation of the BHJ components.[32]

iv.   Higher device performance of MMW-P3HT BHJ system when compared to HMW-P3HT BHJ system is due to their different initial states in the thin film. HMW-P3HT BHJ system is more prone to chain entanglements and conformational constraints due to the longer chain length of the polymer. It should also be noted that EFTA treatment can overcome these restrictions and improve efficiency higher than conventional TA treatments.
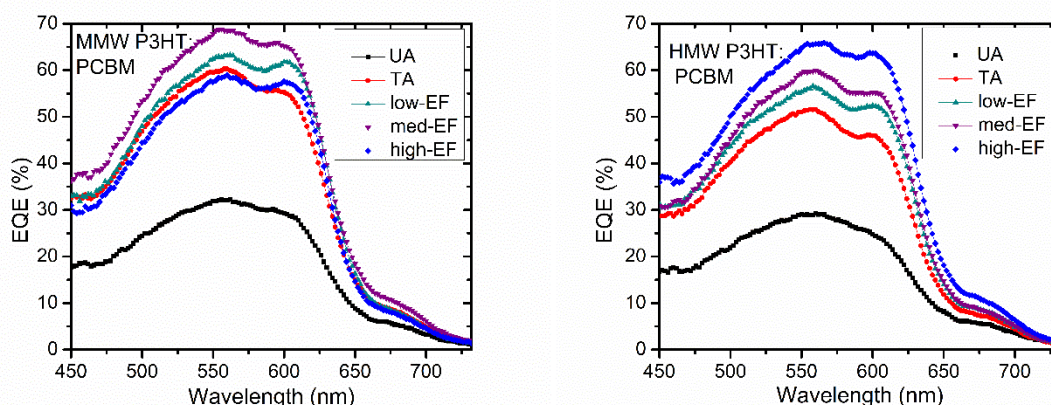
Figure 2.9 *Typical EQE characteristics of (a) MMW P3HT: $PC_{70}BM$ and (b) HMW P3HT: $PC_{70}BM$ BHJ solar cells. UA and TA correspond to Untreated and Thermally annealed control devices, respectively. low-EF, med-EF, and high-EF correspond to EFTA treated devices with EF strengths 4×10^2 V/cm, 2×10^3 V/cm and 1×10^4 V/cm respectively. A light source (Zolix LSH – T150 Tungsten Halogen Lamp) coupled with a monochromator (SPEX 500) was used to illuminate the device area. EQE was measured at short circuit conditions using an electrometer (Keithley EM 6514). The light intensity was calibrated using a silicon detector (from UDT instruments).*

Typical External Quantum Efficiency (EQE) spectra obtained for MMW-P3HT: $PC_{70}BM$ and HMW-P3HT: $PC_{70}BM$ devices are shown in Figure 2.9. The EQE spectra are characterized by two distinct peaks, centered around 550 nm and 600 nm, respectively. These peaks correspond to the absorption features of P3HT. For MMW-P3HT: $PC_{70}BM$ system, EQE_{max} increases from ~ 60% (TA) to ~ 70% (med-EFTA) with EFTA treatment. EQE_{max} decreases to ~60% when EFTA treatment is carried out at higher EF strengths. For HMW-P3HT: $PC_{70}BM$ BHJ system, EQE_{max} increases from ~ 55% (TA) to ~ 65% (high-EFTA) respectively, with EFTA treatment. This correlates well with the observed increase in J_{sc} of the solar cell devices with EFTA treatment.

Table 2.3 *Solar cell parameters obtained from J−V Characteristics measured under 1 Sun light Illumination for MMW-P3HT: $PC_{70}BM$ devices. TA corresponds to thermally annealed devices. med-EF and high-EF refer to EFTA treated devices with EF strengths 2 x 10^3 V/cm and 1 x 10^4 V/cm, respectively. Thermal Annealing at 70 °C was carried out for various time durations t_{dur}.*

t_{dur} (minutes)		V_{oc} (V)	J_{sc} (mA/cm^2)	Fill Factor (%)	Efficiency (%)
20	TA	0.57±0.00	7.97±0.23	38.22±1.44	1.74±0.11
	med-EF	0.56±0.00	8.2±0.17	44.68±1.07	2.05±0.01
	high-EF	0.58±0.00	9.24±0.30	45.85±0.02	2.48±0.08
90	TA	0.59±0.00	9.28±0.30	66.86±0.30	3.67±0.12
	med-EF	0.57±0.00	10.51±0.10	63.26±0.76	3.78±0.08
	high-EF	0.59±0.00	9.90±0.17	66.58±0.01	3.90±0.07
150	TA	0.57±0.00	9.93±0.24	62.50±0.91	3.57±0.11
	med-EF	0.55±0.01	9.43±0.08	53.06±1.75	2.77±0.08
	high-EF	0.57±0.00	9.44±0.19	38.26±1.86	2.07±0.15

Effect of EFTA treatment on MMW-P3HT: $PC_{70}BM$ was also studied by varying the duration of thermal annealing at a lower annealing temperature of 70 °C. The ability to arrive at optimum morphology of the active layer without higher temperature processing is beneficial when the fabrication is scaled up and flexible substrates are involved. It has been shown that thermal treatments above 150°C increases sheet resistance and physical deformation in flexible

substrates.[33] OSCs were fabricated whose corresponding BHJ films were subjected EFTA treatment where the duration of the treatment(t_{dur}) and strength of EF was varied. Solar cell characteristics obtained from a large set of data is shown in Table 2.3. When t_{dur} = 20 minutes, EFTA treatment enhances device performance (1.78% to 2.48%) when compared to control-TA devices with significant improvements in J_{sc} (8 mA/cm^2 to 9.24 mA/cm^2) and FF (38% to 46%). Similar results are obtained with EFTA treatments at higher t_{dur} = 90 minutes, but the device efficiencies are higher and relative increase with EFTA treatment is lower. Average efficiencies were as high as 3.9% for high-EF devices with t_{dur} = 90 minutes.

On the further increase of t_{dur} to 150 minutes, it was observed that EFTA treatment reduces the device performance with increase in EF strength applied during the treatment. This observed trend is similar to the case where higher EF strengths reduced the device efficiencies for MMW-P3HT: PC$_{70}$BM devices annealed at 130ºC for 10 minutes. This implies that the BHJ system has entered a state where EFTA treatment becomes detrimental because of unfavourable vertical phase separation in the blend.

2.3 Dependence of direction of EF applied during EFTA treatment on the change in morphology

From the earlier part, it is clear that EFTA treatment can bring in vertical phase segregation in the BHJ system. The increase in device performance obtained due to EFTA treatment is due to increased ordering in donor domains and optimized vertical phase separation.

2.3.1 EFTA treatment

The question addressed in this part of the chapter is whether the redistribution of PC$_{70}$BM due to EFTA treatment dependent on the direction of EF applied during the treatment. To understand that, EFTA treatment was studied by varying the polarity. Two new terminologies are introduced. EF(+) implies that the positive terminal was connected to the bottom ITO and top ITO was left grounded during the EFTA treatment. EF(-) implies that during the EFTA treatment, the positive terminal was connected to the top electrode and the bottom electrode was grounded.

2.3.2 Solar cell characteristics

Solar cell characteristics were studied by varying the direction of EF treatment for MMW-P3HT: PC$_{70}$BM solar cells. Typical J-V characteristics obtained for the control and EFTA

treated samples are shown in Figure 2.10. Solar cell parameters obtained from a large set of solar cells are shown in Table 2.4. From the data, it is very clear that there is a dependency in the direction of EF applied during the treatment. Best device efficiencies ($\approx$ 3.5 %) are obtained for low-EF(+) treated devices. High-EF treated devices EFTA treated both in the positive and negative directions show a reduction in efficiency because of undesirable morphology.
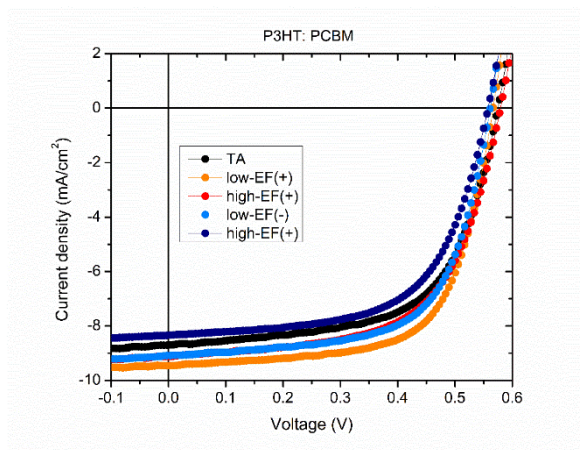
Figure 2.10 *Typical solar cell characteristics of MMW P3HT: PC$_{70}$BM BHJ solar cells under 1 sun illumination. TA corresponds to the thermally annealed control device. Low-EF and high-EF refer to EFTA treated devices with EF strengths 3.3 **x** 10^3 V/cm, and 8.3 $\times$ 10^3 V/cm, respectively. EF(+) and EF(-) correspond to positive and negative directions of polarity maintained during EFTA treatment, respectively. Experimental setup is described in the caption of Figure 2.8.*

It should be noted that for the same EF strengths, EF(+) treated devices show higher device parameters than corresponding EF(-) treated devices. This clearly shows that there is a clear dependence on the polarity of EF applied during EFTA treatment.

Table 2.4 *Solar cell parameters obtained from J-V characteristics of MMW P3HT: PC$_{70}$BM BHJ solar cells under 1 sun illumination. TA corresponds to the thermally annealed control device. Low-EF and high-EF refer to EFTA treated devices with EF strengths 3.3 x 10^3 V/cm, and 8.3 × 10^3 V/cm, respectively. EF(+) and EF(-) correspond to positive and negative directions of polarity maintained during EFTA treatment, respectively.*

	Voc (V)	J$_{sc}$ (mA/cm2)	Fill Factor (%)	Efficiency (%)
TA	0.57±0.00	8.4±0.15	63.32±1.26	3.06±0.04
Low-EF(+)	0.57±0.00	9.44±0.17	65.91±1.3	3.52±0.08
High-EF(+)	0.58±0.00	9.03±0.05	58.01±2.13	3.03±0.12
Low-EF(-)	0.56±0.00	9±0.05	64.28±0.89	3.23±0.07
High-EF(-)	0.55±0.00	8.47±0.07	59.39±0.90	2.75±0.06

2.3.3 Atomic Force Microscopy (AFM) imaging
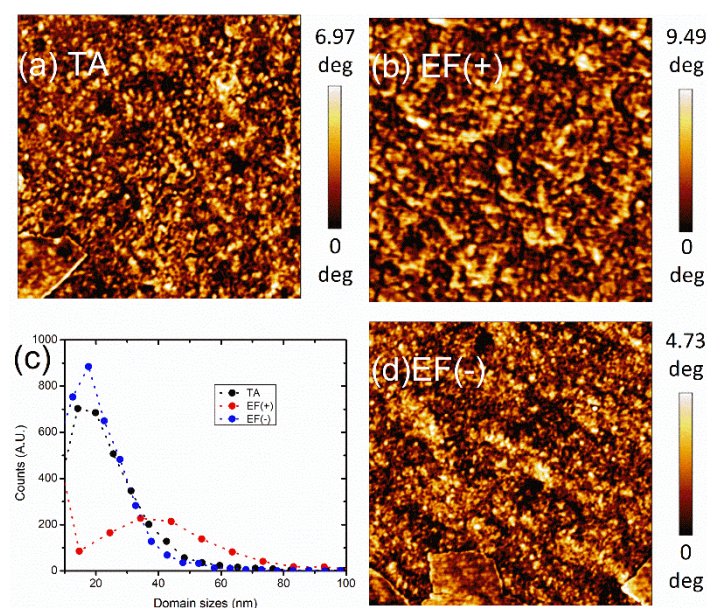
Figure 2.11 *AFM phase images (3 x 3 μm^2) of a) TA b) EF(+) d) EF(-) treated P3HT: PC$_{70}$BM BHJ active layers coated on ZnO coated ITO substrates. EF strength maintained during the treatment was ≅ 8.3 × 10^3 V/cm. c) Domain sizes calculated from sample area of 3 x 3 μm^2 using Image Processing software Gwyddion. Experimental setup is described in the caption of Figure 2.6.*

The changes introduced in the BHJ films owing to the EFTA treatment is more evident from the AFM imaging. The phase images obtained for the P3HT: $PC_{70}BM$ films are shown as a function of treatment. For the EF(+) case, where the average distribution of $PC_{70}BM$ is moving to the bottom of the film, allows P3HT domains to form larger clusters. This is evident in the domain size distribution estimated from the AFM phase images using image analysis. The mean of the domain size shifts to 40 nm for the EF(+) case. For the EF(-) case, where $PC_{70}BM$ comes to the top of the film competes with the P3HT domain formation. This shifts the average domain size to smaller domains when compared to the domain sizes obtained from TA thin films.

2.3.4 Advantages of EFTA over other treatments

Both thermal annealing and solvent annealing treatments have also shown to bring in vertical phase segregation in the active layer. The direction of phase segregation is not controlled, favouring either conventional or inverted device architecture. But EFTA treatment allows vertical phase segregation in either direction depending on the polarity of EF applied during the treatment. The strength of EF allows us to control the extent of vertical phase separation of active layer components.

Absorption and hole mobility studies have indicated that there is an improvement in the crystalline order in the P3HT domains with EFTA treatment. It was noticed from the GIWAXS studies that EFTA treatment is able to bring in controlled vertical phase segregation of active layer components. Solar cells fabricated showed an improvement in device efficiency when compared to control thermal annealed devices. The improvement in performance was attributed to enhanced ordering in the crystalline regions of the polymer and better optimized vertical phase segregation of active layer components.

The EF strength required for optimum device performance is dependent on the molecular weight of the polymer donor. There is a critical threshold EF strength above which EFTA treatment becomes detrimental. It was shown that this threshold EF strength was dependent on the molecular weight of the donor. This reduction at higher EF strengths could be due to the reduction of charge generation efficiency due to increased vertical phase separation. Role of crystallinity of donor was also studied in this chapter. It was observed that it was easier for $PC_{70}BM$ to migrate in relatively less crystalline HMW-P3HT BHJ films.

By varying the direction of the electric field applied during the EFTA treatment, it was shown that the directionality of vertical phase segregation in the active layer can be varied. It was

shown that PC$_{70}$BM could be moved to the bottom and top of the active layer by applying positive EF (positive terminal connected to the bottom electrode during EFTA treatment) and negative EF (positive terminal connected to the top electrode during EFTA treatment) respectively. This was clearly observed in AFM morphology studies as variation in domain size distribution with EFTA treatment.

2.4 Summary

Dependence of the molecular weight of P3HT and its response towards EFTA treatment was studied in this chapter. EFTA treatment was shown to improve device efficiency for both the BHJ systems. It was also noticed that the vertical distribution of the active layer components can be tuned by EFTA treatment by controlling the strength and polarity of EF applied during the treatment.

References

1. Dang, M. T.; Hirsch, L.; Wantz, G., P3HT:PCBM, Best Seller in Polymer Photovoltaic Research. *Advanced Materials* **2011,** *23* (31), 3597-3602.

2. Chen, D.; Nakahara, A.; Wei, D.; Nordlund, D.; Russell, T. P., P3HT/PCBM Bulk Heterojunction Organic Photovoltaics: Correlating Efficiency and Morphology. *Nano Letters* **2011,** *11* (2), 561-567.

3. Campoy-Quiles, M.; Ferenczi, T.; Agostinelli, T.; Etchegoin, P. G.; Kim, Y.; Anthopoulos, T. D.; Stavrinou, P. N.; Bradley, D. D. C.; Nelson, J., Morphology evolution via self-organization and lateral and vertical diffusion in polymer:fullerene solar cell blends. *Nature Materials* **2008,** *7*, 158.

4. Erb, T.; Zhokhavets, U.; Gobsch, G.; Raleva, S.; Stühn, B.; Schilinsky, P.; Waldauf, C.; Brabec, C. J., Correlation Between Structural and Optical Properties of Composite Polymer/Fullerene Films for Organic Solar Cells. *Advanced Functional Materials* **2005,** *15* (7), 1193-1196.

5. Collins, B. A.; Tumbleston, J. R.; Ade, H., Miscibility, Crystallinity, and Phase Development in P3HT/PCBM Solar Cells: Toward an Enlightened Understanding of Device Morphology and Stability. *The Journal of Physical Chemistry Letters* **2011,** *2* (24), 3135-3145.

6. Westacott, P.; Tumbleston, J. R.; Shoaee, S.; Fearn, S.; Bannock, J. H.; Gilchrist, J. B.; Heutz, S.; deMello, J.; Heeney, M.; Ade, H.; Durrant, J.; McPhail, D. S.; Stingelin, N., On the role of intermixed phases in organic photovoltaic blends. *Energy & Environmental Science* **2013,** *6* (9), 2756-2764.

7.   Watts, B.; Belcher, W. J.; Thomsen, L.; Ade, H.; Dastoor, P. C., A Quantitative Study of PCBM Diffusion during Annealing of P3HT:PCBM Blend Films. *Macromolecules* **2009,** *42* (21), 8392-8397.

8.   Treat, N. D.; Brady, M. A.; Smith, G.; Toney, M. F.; Kramer, E. J.; Hawker, C. J.; Chabinyc, M. L., Interdiffusion of PCBM and P3HT Reveals Miscibility in a Photovoltaically Active Blend. *Advanced Energy Materials* **2011,** *1* (1), 82-89.

9.   Agostinelli, T.; Lilliu, S.; Labram, J. G.; Campoy-Quiles, M.; Hampton, M.; Pires, E.; Rawle, J.; Bikondoa, O.; Bradley, D. D. C.; Anthopoulos, T. D.; Nelson, J.; Macdonald, J. E., Real-Time Investigation of Crystallization and Phase-Segregation Dynamics in P3HT:PCBM Solar Cells During Thermal Annealing. *Advanced Functional Materials* **2011,** *21* (9), 1701-1708.

10.   Wu, W.-R.; Jeng, U. S.; Su, C.-J.; Wei, K.-H.; Su, M.-S.; Chiu, M.-Y.; Chen, C.-Y.; Su, W.-B.; Su, C.-H.; Su, A.-C., Competition between Fullerene Aggregation and Poly(3-hexylthiophene) Crystallization upon Annealing of Bulk Heterojunction Solar Cells. *ACS Nano* **2011,** *5* (8), 6233-6243.

11.   Li, G.; Shrotriya, V.; Yao, Y.; Yang, Y., Investigation of annealing effects and film thickness dependence of polymer solar cells based on poly(3-hexylthiophene). *Journal of Applied Physics* **2005,** *98* (4), 043704.

12.   Kim, Y.; Choulis, S. A.; Nelson, J.; Bradley, D. D. C.; Cook, S.; Durrant, J. R., Device annealing effect in organic solar cells with blends of regioregular poly(3-hexylthiophene) and soluble fullerene. *Applied Physics Letters* **2005,** *86* (6), 063502.

13.   Swinnen, A.; Haeldermans, I.; vande Ven, M.; D'Haen, J.; Vanhoyland, G.; Aresu, S.; D'Olieslaeger, M.; Manca, J., Tuning the Dimensions of C60-Based Needlelike Crystals in Blended Thin Films. *Advanced Functional Materials* **2006,** *16* (6), 760-765.

14.   Lee, J. K.; Ma, W. L.; Brabec, C. J.; Yuen, J.; Moon, J. S.; Kim, J. Y.; Lee, K.; Bazan, G. C.; Heeger, A. J., Processing Additives for Improved Efficiency from Bulk Heterojunction Solar Cells. *Journal of the American Chemical Society* **2008,** *130* (11), 3619-3623.

15.   Liao, H.-C.; Ho, C.-C.; Chang, C.-Y.; Jao, M.-H.; Darling, S. B.; Su, W.-F., Additives for morphology control in high-efficiency organic solar cells. *Materials Today* **2013,** *16* (9), 326-336.

16.   Lou, S. J.; Szarko, J. M.; Xu, T.; Yu, L.; Marks, T. J.; Chen, L. X., Effects of Additives on the Morphology of Solution Phase Aggregates Formed by Active Layer Components of

High-Efficiency Organic Solar Cells. *Journal of the American Chemical Society* **2011,** *133* (51), 20661-20663.

17.   Schilinsky, P.; Asawapirom, U.; Scherf, U.; Biele, M.; Brabec, C. J., Influence of the Molecular Weight of Poly(3-hexylthiophene) on the Performance of Bulk Heterojunction Solar Cells. *Chemistry of Materials* **2005,** *17* (8), 2175-2180.

18.   Ballantyne, A. M.; Chen, L.; Dane, J.; Hammant, T.; Braun, F. M.; Heeney, M.; Duffy, W.; McCulloch, I.; Bradley, D. D. C.; Nelson, J., The Effect of Poly(3-hexylthiophene) Molecular Weight on Charge Transport and the Performance of Polymer:Fullerene Solar Cells. *Advanced Functional Materials* **2008,** *18* (16), 2373-2380.

19.   Zhao, K.; Khan, H. U.; Li, R.; Su, Y.; Amassian, A., Entanglement of Conjugated Polymer Chains Influences Molecular Self-Assembly and Carrier Transport. *Advanced Functional Materials* **2013,** *23* (48), 6024-6035.

20.   Hiorns, R. C.; de Bettignies, R.; Leroy, J.; Bailly, S.; Firon, M.; Sentein, C.; Khoukh, A.; Preud'homme, H.; Dagron-Lartigau, C., High Molecular Weights, Polydispersities, and Annealing Temperatures in the Optimization of Bulk-Heterojunction Photovoltaic Cells Based on Poly(3-hexylthiophene) or Poly(3-butylthiophene). *Advanced Functional Materials* **2006,** *16* (17), 2263-2273.

21.   Brown, P. J.; Thomas, D. S.; Köhler, A.; Wilson, J. S.; Kim, J.-S.; Ramsdale, C. M.; Sirringhaus, H.; Friend, R. H., Effect of interchain interactions on the absorption and emission of poly(3-hexylthiophene). *Physical Review B* **2003,** *67* (6), 064203.

22.   Li, G.; Shrotriya, V.; Huang, J.; Yao, Y.; Moriarty, T.; Emery, K.; Yang, Y., High-efficiency solution processable polymer photovoltaic cells by self-organization of polymer blends. *Nature Materials* **2005,** *4* (11), 864-868.

23.   Spano, F. C., Modeling disorder in polymer aggregates: The optical spectroscopy of regioregular poly(3-hexylthiophene) thin films. *The Journal of Chemical Physics* **2005,** *122* (23), 234701.

24.   Shreve, A. P.; Haroz, E. H.; Bachilo, S. M.; Weisman, R. B.; Tretiak, S.; Kilina, S.; Doorn, S. K., Determination of Exciton-Phonon Coupling Elements in Single-Walled Carbon Nanotubes by Raman Overtone Analysis. *Physical Review Letters* **2007,** *98* (3), 037405.

25.   Turner, S. T.; Pingel, P.; Steyrleuthner, R.; Crossland, E. J. W.; Ludwigs, S.; Neher, D., Quantitative Analysis of Bulk Heterojunction Films Using Linear Absorption Spectroscopy and Solar Cell Performance. *Advanced Functional Materials* **2011,** *21* (24), 4640-4652.

26.   Pingel, P.; Zen, A.; Abellón, R. D.; Grozema, F. C.; Siebbeles, L. D. A.; Neher, D., Temperature-Resolved Local and Macroscopic Charge Carrier Transport in Thin P3HT Layers. *Advanced Functional Materials* **2010,** *20* (14), 2286-2295.

27.   Juška, G.; Nekrašas, N.; Genevičius, K., Investigation of charge carriers transport from extraction current transients of injected charge carriers. *Journal of Non-Crystalline Solids* **2012,** *358* (4), 748-750.

28.   Zhokhavets, U.; Erb, T.; Hoppe, H.; Gobsch, G.; Serdar Sariciftci, N., Effect of annealing of poly(3-hexylthiophene)/fullerene bulk heterojunction composites on structural and optical properties. *Thin Solid Films* **2006,** *496* (2), 679-682.

29.   Joshi, S.; Grigorian, S.; Pietsch, U.; Pingel, P.; Zen, A.; Neher, D.; Scherf, U., Thickness Dependence of the Crystalline Structure and Hole Mobility in Thin Films of Low Molecular Weight Poly(3-hexylthiophene). *Macromolecules* **2008,** *41* (18), 6800-6808.

30.   Chiu, M.-Y.; Jeng, U.-S.; Su, C.-H.; Liang, K. S.; Wei, K.-H., Simultaneous Use of Small- and Wide-Angle X-ray Techniques to Analyze Nanometerscale Phase Separation in Polymer Heterojunction Solar Cells. *Advanced Materials* **2008,** *20* (13), 2573-2578.

31.   Balko, J.; Lohwasser, R. H.; Sommer, M.; Thelakkat, M.; Thurn-Albrecht, T., Determination of the Crystallinity of Semicrystalline Poly(3-hexylthiophene) by Means of Wide-Angle X-ray Scattering. *Macromolecules* **2013,** *46* (24), 9642-9651.

32.   Bartelt, J. A.; Beiley, Z. M.; Hoke, E. T.; Mateker, W. R.; Douglas, J. D.; Collins, B. A.; Tumbleston, J. R.; Graham, K. R.; Amassian, A.; Ade, H.; Fréchet, J. M. J.; Toney, M. F.; McGehee, M. D., The Importance of Fullerene Percolation in the Mixed Regions of Polymer–Fullerene Bulk Heterojunction Solar Cells. *Advanced Energy Materials* **2013,** *3* (3), 364-374.

33.   Zardetto, V.; Brown, T. M.; Reale, A.; Di Carlo, A., Substrates for flexible electronics: A practical investigation on the electrical, film flexibility, optical, temperature, and solvent resistance properties. *Journal of Polymer Science Part B: Polymer Physics* **2011,** *49* (9), 638-648.

Chapter 3

Electric Field-Assisted Thermal Annealing (EFTA) Treatment of Amorphous-Polymer Donor: Fullerene-Acceptor-Based Solar Cells

3.1 Introduction

3.1.1 Active layer

In this chapter, the effect of EFTA treatment on amorphous donor polymer blends with fullerene acceptors is studied. Poly[4,8-bis(5-(2-ethylhexyl)thiophen-2-yl)benzo[1,2-b;4,5-b']dithiophene-2,6-diyl-alt-(4-(2-ethylhexyl)-3-fluorothieno[3,4-b]thiophene-)-2-carboxylate-2-6-diyl)] (PTB7-Th) is a model amorphous polymer donor (molecular structure is shown in Figure 3.1) and has a lower-band gap (red-shifted) as compared to the semi-crystalline P3HT. Thermal annealing procedure for pure amorphous systems in principle does not alter the microstructure. Additive treatment has been found to be more effective usually for obtaining optimum BHJ films from blends of PTB7-Th and $PC_{70}BM$ to result in increased device efficiency of solar cells.[1, 2] Di-iodo-octane (DIO) is usually added in very small quantities to the native solvent used for the fabrication of solar cells.[3, 4] In semi-crystalline BHJ systems, DIO has been found to increase phase segregation of the active layer components. In the case of amorphous donor systems like PTB7-Th: $PC_{70}BM$, the addition of DIO limits phase segregation of the components. This allows for the formation of more homogenous distribution of donors and acceptors in the film, which eventually increases charge generating interface sites.[3, 5]
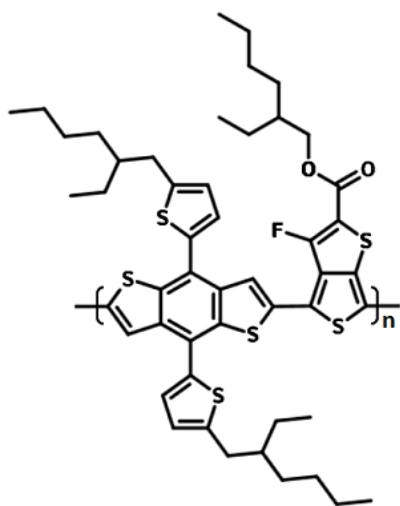
Figure 3.1 *Molecular structure of PTB7-Th polymer donor*

Although additive treatment contributes to the enhancement of device efficiencies, it leads to irreversible detrimental morphological changes in the active layer over time.[6] DIO molecule has a very low vapour pressure (0.04 Pa); hence, it stays longer in the film. Owing to its selective solubility of $PC_{70}BM$ molecules, the domain sizes of $PC_{70}BM$ regions increases in

size over time due to the presence of remnant DIO solvent in the active layer. This eventually reduces device efficiency over time due to unfavourable morphology, manifesting itself as a loss in device stability. It is necessary to arrest these metastable morphological changes to improve device efficiency.

Thermal annealing treatment after the film formation can remove DIO in the active layer, thereby improving stability.[7] However thermal annealing also leads to the formation of larger $PC_{70}BM$ domains in the active layer which limits device performance.[6] This eventually leads to a trade-off between stability and device efficiency in these BHJ systems.

Treatments like washing the active layer film with an inert solvent like methanol have shown to remove DIO and thereby locking the morphology.[8] But this treatment leads to enriched $PC_{70}BM$ in the top of the film, which will be unfavourable for solar cells devices fabricated in 'inverted architecture.'

3.1.2 EFTA treatment

The issue that is being addressed in this chapter is the effectiveness of EFTA treatment to control vertical phase segregation in the amorphous donor BHJ system of PTB7-Th: $PC_{70}BM$ (similar to the trend observed in P3HT: $PC_{70}BM$ BHJ system). In the earlier chapter, it was observed that $PC_{70}BM$ molecules were able to translate to a larger extent under EFTA treatment in the relatively more amorphous HMW-P3HT BHJ system. It is expected that the relatively more amorphous donor polymer like PTB7-Th should favour vertical distribution with EFTA treatment. EFTA treatment was studied by applying EF during thermal annealing treatment as described in the earlier chapter. The dependence on the polarity of EF applied during the EFTA treatment was also studied. EF(+) implies that the positive terminal was connected to the bottom ITO substrate and the top ITO counter was grounded during the EFTA treatment. EF(-) implies that during the EFTA treatment, the positive terminal was connected to the top electrode and the bottom electrode substrate was grounded. TA and UA terms refer to the control samples which have undergone thermal annealing treatment and completely untreated films, respectively.

3.1.3 Fabrication of thin films and solar cells

BHJ solutions of PTB7-Th: $PC_{70}BM$ were made at 1:2 ratio with polymer concentration at 12 mg/ml in chlorobenzene: di-iodo-octane (97:3 v/v) solvent. BHJ solutions were kept for more than 8 hours at 55 °C. The solutions were brought to room temperature. For fabricating active

layer thin films, the active layer was then spin-coated at 1000 rpm for 1 minute on ITO substrates inside a nitrogen-rich glovebox. Solar cell device fabrication involved spin-coating the active layer on ZnO coated ITO substrates. The active layer was then thermally annealed or EFTA treated, as described in Chapter 2. EFTA treatment was carried out where thermal annealing conditions were set as 140 ºC for 10 minutes

3.2 Characterization

3.2.1 Absorption studies

The absorption spectra of the BHJ thin films of PTB7-Th: $PC_{70}BM$ as a function of EFTA treatment is shown in Figure 3.2. The peaks around 640 nm and 700 nm correspond to the peaks of PTB7-Th.[1, 2] It was observed that there were no significant changes in the spectra with respect to the EFTA treatment when compared to only TA treatment. This could be due to non-crystalline nature of the polymer donor.
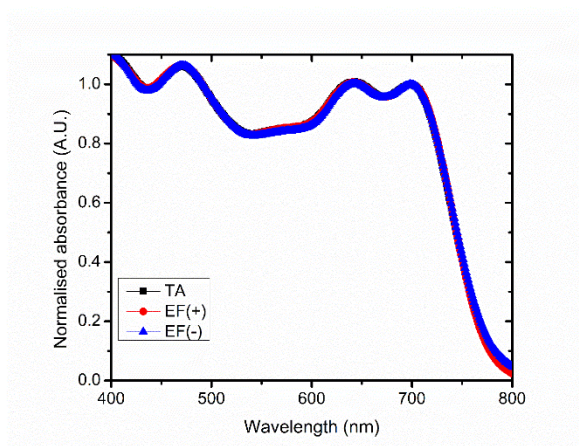
Figure 3.2 *Absorption spectra of BHJ films of PTB7-Th: $PC_{70}BM$. TA indicates Thermally annealed BHJ films. EF(+) and EF(-) indicates EFTA treated BHJ in positive and negative directions, respectively (EF strength $\cong 8.3 \times 10^3$ V/cm).Absorption studies of thin films were carried out using Perkin Elmer UV/Vis/NIR Lambda 750 Spectrometer.*

3.2.2 GIWAXS studies

X-ray diffraction studies were carried out to obtain insights into the morphological variations induced by the EFTA treatment. Even though PTB7-Th is an amorphous donor polymer, there exists small crystalline regions of the polymer in the amorphous matrix, which is evident from the GIWAXS spectra of the BHJ films of PTB7-Th: $PC_{70}BM$ (Figure 3.3).
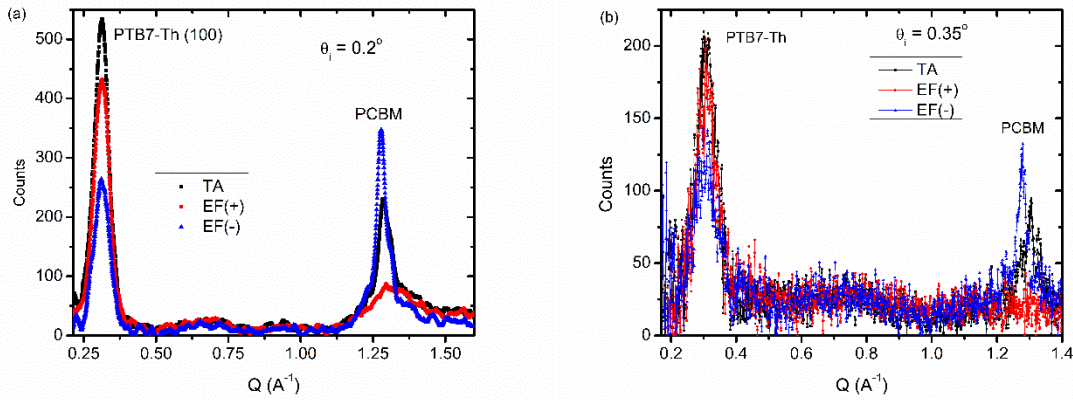
Figure 3.3 *GIWAXS Out-Of-Plane spectra of BHJ films of PTB7-Th: $PC_{70}BM$ at incidence angles a) 0.2° and b) 0.35° respectively. TA indicates Thermally annealed BHJ films. EF(+) and EF(-) indicates EFTA treated BHJ in positive and negative directions, respectively. (EF strength $\cong 8.3 \times 10^3$ V/cm). Experimental setup is described in the caption of Figure 2.7.*

The incidence angle (θ_i) during the GIWAXS measurements was varied to carry out depth analysis of the active layer films. Similar depth analysis using GIWAXS studies have been studied earlier to probe vertical phase segregation of P3HT: $PC_{70}BM$ active layer film with thermal annealing.[9] Critical angle (θ_c) is defined as the angle of incidence at which the incoming X-rays grazes the top surface and is dependent on the active layer. θ_c for PTB7-Th: $PC_{70}BM$ films were found to be $\approx 0.15°$. BHJ films were probed with two different incidence angles, 0.20° and 0.35°, such that one of the angles was closer to the critical angle. When the $\theta_i \approx \theta_c$, BHJ film close to the air-BHJ interface was probed. When the $\theta_I > \theta_c$, the bulk of the active layer was probed.

Table 3.1 *Analysis from GIWAXS spectra of PTB7-Th: $PC_{70}BM$ BHJ films. TA refers to thermally annealed sample. EF(+) and EF(-) refers to EFTA treated samples in positive and negative directions, respectively (EF strength $\cong 8.3 \times 10^3$ V/cm).*

	$R(\theta_i = 0.2^o)$ $= \dfrac{PCBM\,(\theta_i = 0.2^o)}{PTB7-Th\,(\theta_i = 0.2^o)}$	$R(\theta_i = 0.35^o)$ $= \dfrac{PCBM\,(\theta_i = 0.35^o)}{PTB7-Th\,(\theta_i = 0.35^o)}$	$\dfrac{R(\theta_i = 0.35^o)}{R\,(\theta_i = 0.2^o)}$
TA	0.43	0.46	1.07
EF(+)	0.2	0.27	1.32
EF(-)	1.33	1.04	0.78

GIWAXS spectra of EFTA treated and control BHJ films, obtained at two different incidence angles are shown in Figure 3.3. The peaks around q values of 0.31 A^{-1} and 1.28 A^{-1} corresponds PTB7-Th (100 peak) and $PC_{70}BM$ respectively.[10]

Consider the GIWAXS spectra obtained at $\theta_i = 0.2^\circ$. It can be seen that for the EF(+) treated films, $PC_{70}BM$ peak (around q value of 1.28 A^{-1}) reduces in intensity and for the EF(-) case, $PC_{70}BM$ peak increases in intensity, when compared to TA films. This trend is also reflected in the GIWAXS spectra, where bulk is probed ($\theta_i = 0.35^\circ$). From the intensities of $PC_{70}BM$ and PTB7-Th, a parameter R is defined, which is given by the ratio of the intensity of $PC_{70}BM$ peak to the intensity of PTB7-Th peak. This parameter R obtained from GIWAXS spectra at both the incidence angles are shown in Table 3.1.

The last column of Table 3.1, a parameter T is defined, which is given by the ratio of R obtained at higher incidence angle (0.35°) to R obtained at lower incidence angle (0.2°). This parameter T defines how the relative fraction of $PC_{70}BM$ with respect to PTB7-Th varies as we move from the air-BHJ interface into the bulk of the film. $T \approx 1$ implies that the relative fraction of $PC_{70}BM$ with respect to the polymer donor do not vary when you move from the top surface to bulk. Value of T less than 1 (greater than 1) implies that $PC_{70}BM$ proportion relative to PTB7-Th reduces (increases) when we move from surface to bulk. For the EF(+) case, it can be observed that T = 1.35 (>1), which indicates that $PC_{70}BM$ contribution in the active layer increases we move from surface to bulk implying that contribution of $PC_{70}BM$ is lesser in the surface. For the EF(-) case, T = 0.78(<1), this implies that $PC_{70}BM$ contribution reduces as we move from surface to bulk implying that it initially started with a higher concentration of $PC_{70}BM$ on top of the film.

Figure 3.4. *AFM phase images (3 x 3 μm^2) of a) TA b) EF(+) c) EF(-) treated PTB7-Th: $PC_{70}BM$ BHJ active layers coated on ZnO/ITO. . TA indicates Thermally annealed BHJ films. EF(+) and EF(-) indicates EFTA treated BHJ in positive and negative direction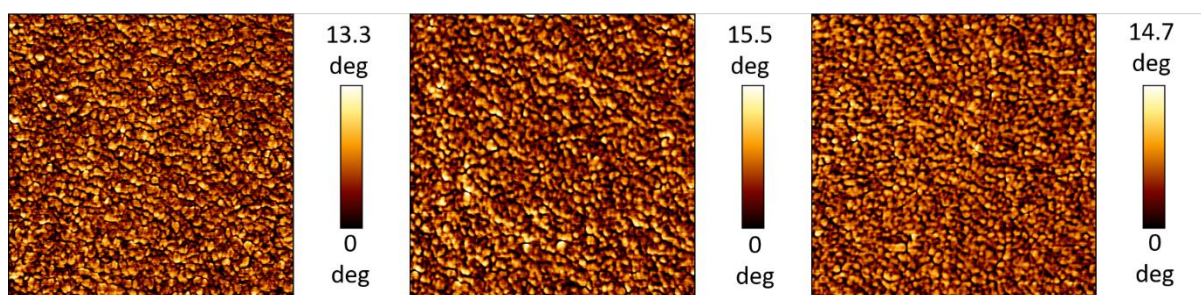s, respectively. (EF strength $\cong 8.3 \times 10^3$ V/cm). Experimental setup is described in the caption of Figure 2.6*

.**3.2.3 Surface characterization**

The surface of the active layer was probed by AFM imaging. The phase images obtained as a function of EFTA treatment is shown in Figure 3.4. Phase images of PTB7-Th: $PC_{70}BM$ thin films did not show any discernible change on account of EFTA treatment, owing to the amorphous nature of the polymer donor.
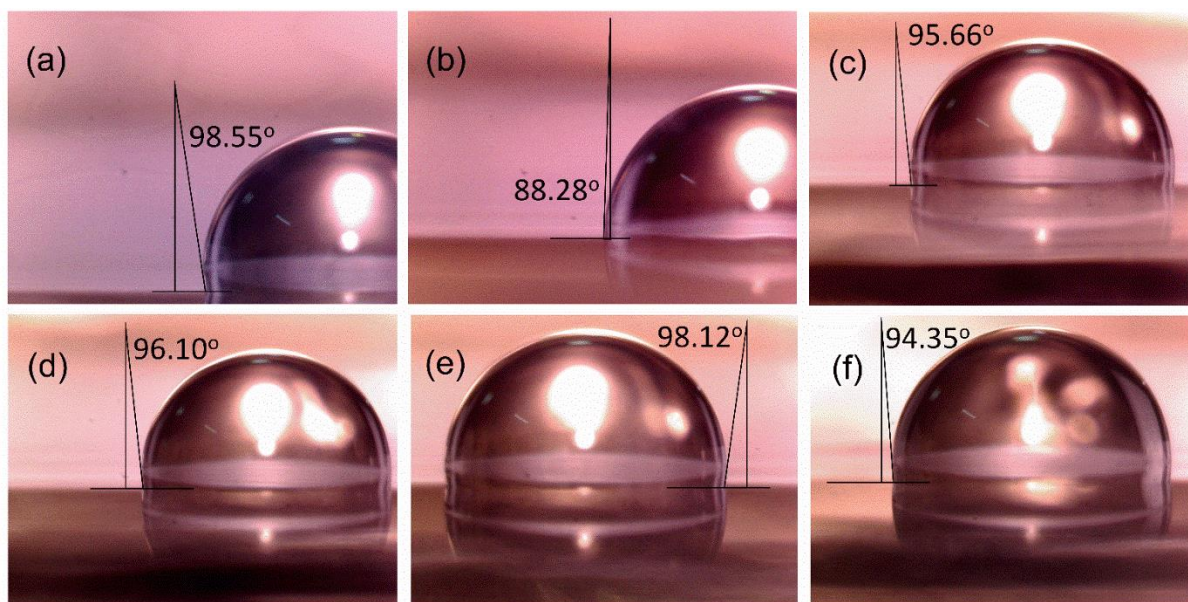
Figure 3.5 *Representative images of water contact angle measurements on thin films of a)*
PTB7-Th (pristine) b) $PC_{70}BM$ (pristine) c) Control (BHJ Blend) d) TA (BHJ Blend) e) EF(+)
(BHJ Blend) f) EF(-) (BHJ Blend). Control and TA correspond to untreated and thermally
annealed control samples, respectively. EF(+) and EF(-) refers to EFTA treated samples in
positive and negative directions, respectively (EF strength$\cong 8.3 \times 10^3$ V/cm).

The air-BHJ interface was further probed by water contact angle measurements. Contact angles were measured for pristine films, control, and EFTA treated BHJ films. Contact angles were obtained from measurements at different locations on the sample films. Typical water contact images obtained and the averaged contact values obtained for all the cases are shown in Figure 3.5. From the averaged contact angles of pristine and BHJ films, the fraction of donor polymer in the BHJ films in the air-BHJ interface was computed by using Cassie-Baxter equation,[6, 11]

$$\cos \theta_{Blend} = f \, \cos \theta_{PTB7-Th} + (1-f) \cos \theta_{PCBM} \qquad (3.1)$$

$\theta_{PTB7-Th}$, θ_{PCBM}, and θ_{Blend} correspond to water contact angles obtained for pristine PTB7-Th film, pristine $PC_{70}BM$ film, and BHJ blend films respectively. f corresponds to the fraction of

the donor polymer on the top of the films. Donor fraction obtained for the control and EFTA treated BHJ films are shown in Table 3.2.

The control untreated (UA) and TA films show a significantly higher fraction of donor on the air-BHJ interface. This observation is in accordance with earlier literature, which indicates that amorphous donor BHJ systems prefer higher donor concentration on the top of the film. When EF(+) treatment was carried out, the donor fraction increases as high as 93%. For the EF(-) treatment, the donor fraction reduces on top of the film to $\approx$ 56% because of $PC_{70}BM$ accruing at the top of the film.

Both depth analysis with GIWAXS studies and water contact angle measurements confirm the vertical phase segregation with EFTA treatment, with EF(+) and EF(-) treatments translating average distribution of $PC_{70}BM$ to the bottom of the film and air-BHJ interface respectively. The studies have proven the hypothesis that EFTA treatment will be able to bring in vertical phase segregation in the amorphous donor BHJ films.

Table 3.2 *PTB7-Th fraction on the air-BHJ interface for different BHJ films obtained from the Cassie-Baxter equation. UA and TA correspond to Untreated control and Thermally annealed BHJ films, respectively. EF(+) and EF(-) indicates EFTA treated BHJ films in positive and negative directions, respectively.*

	PTB7-Th fraction on the air-BHJ interface
UA	72.82 ± 1.08 %
TA	75.54 ± 0.54 %
EF(+)	92.66 ± 0.82 %
EF(-)	58.69 ± 1.63 %

3.2.4 Solar cell characterization

In the earlier studies involving semi-crystalline donors, EFTA treatment was carried out where thermal annealing conditions were set as 140 °C for 10 minutes. However long annealing times

($\approx$10 minutes) were found to detrimental to these present device performances yielding efficiencies less than 6%.
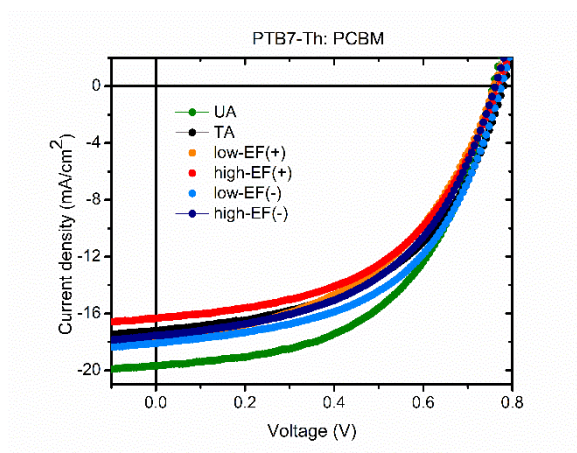
Figure 3.6 *Typical J-V characteristics of PTB7-Th: PC$_{70}$BM BHJ solar cells under 1 sun illumination.UA and TA corresponds to untreated and thermally annealed control devices, respectively. Low-EF and high-EF refer to EFTA treated devices with EF strengths 3.3 x 10^3 V/cm, and 8.3 $\times$ 10^3 V/cm, respectively. EF(+) and EF(-) correspond to positive and negative directions of polarity maintained during EFTA treatment, respectively. Experimental setup is described in the caption of Figure 2.8.*

After careful optimization, EFTA treatment (and TA treatment) duration was set as 150 seconds while annealing temperature was maintained at 140 ^{o}C. Solar cells were fabricated after carrying out EFTA treatment on the BHJ films of PTB7-Th: PC$_{70}$BM with new process parameters. Typical J-V characteristics obtained at 1 sun illumination is shown in Figure 3.6. Solar cell parameters obtained from J-V characteristics from a large set of devices (>10 devices in each case) are shown in Table 3.3.

The untreated control devices (UA) show the highest device efficiency (~7.8%) with J$_{sc}$ of ~19.5 mA/cm^2 and FF of ~52%. But these untreated devices are prone to degradation as will be discussed in the later sections. TA devices show efficiencies close to ~6.7 % with J$_{sc}$ of ~ 17 mA/cm^2 and FF of ~50%. EF(+) treatment reduces device efficiencies relative to TA treatment, with a significant reduction in FF (~48%). However, low-EF(+) devices have higher J$_{sc}$ value of 17.9 mA/cm^2. EF(-) treatment increases the device efficiencies compared to TA treatment, with low-EF(-) treated devices show efficiencies as high as ~7.2%. This increase in device efficiency is attributed to increase in FF (~52%) and J$_{sc}$ (17.5 mA/cm^2).

Table 3.3 *Solar cell parameters obtained from J-V characteristics of PTB7-Th: PC$_{70}$BM BHJ solar cells under 1 sun illumination.UA and TA corresponds to untreated and thermally annealed control devices, respectively. Low-EF and high-EF refer to EFTA treated devices with EF strengths 3.3 x 10^3 V/cm, and 8.3 × 10^3 V/cm, respectively. EF(+) and EF(-) correspond to positive and negative directions of polarity maintained during EFTA treatment, respectively.*

	V$_{oc}$ (V)	J$_{sc}$ (mA/cm^2)	Fill Factor (%)	Efficiency (%)
UA	0.76±0.00	19.69±0.05	52.52±0.61	7.82±0.04
TA	0.78±0.00	16.96±0.24	50.08±0.65	6.61±0.08
Low-EF(+)	0.76±0.00	17.9±0.30	48.18±0.60	6.52±0.16
High-EF(+)	0.77±0.00	16.92±0.32	48.55±1.09	6.3±0.15
Low-EF(-)	0.78±0.00	17.53±0.34	52.2±0.26	7.13±0.15
High-EF(-)	0.76±0.00	17.68±0.27	50.71±0.25	6.86±0.14

In the earlier chapter on semi-crystalline donors based blends, it was observed that lower EF strengths maintained during EF(+) treatment gave the highest device performance. In the case of EFTA treatment of PTB7-Th: PC$_{70}$BM, it was observed that low-EF(-) treatment gives superior performance when compared to other treatments. This observation could be explained by the variation of initial microstructure obtained for semi-crystalline and amorphous polymer donor: fullerene BHJ system in the presence of the solvent additive.[12] For semi-crystalline polymer BHJ systems, the difference between the interaction parameters of the active layer components drives the polymer donor closer to the BHJ-ZnO interface while PC$_{70}$BM moves to the top of the active layer. Hence, EF(+) treatment, which redistributes the PC$_{70}$BM closer to the bottom of the film is found to be favourable. In the case of amorphous donor polymer BHJ systems, PC$_{70}$BM molecules segregate close to the bottom of the film, while the polymer donor displaces to the air-BHJ interface. In this system, low-EF(-) treatment, which drives PC$_{70}$BM to the top of the film is found to be favourable.
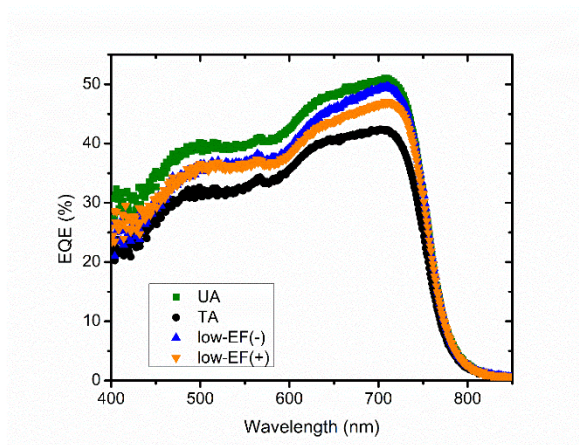
Figure 3.7 *Typical EQE characteristics of EFTA treated and control PTB7-Th: PC$_{70}$BM solar cells. UA and TA correspond to untreated control and thermally annealed control devices, respectively. EF(+) and EF(-) refer to positive and negative directions of polarity maintained during EFTA treatment, respectively. Experimental setup is described in the caption of Figure 2.9.*

Typical EQE spectra obtained for EFTA treated and control devices of PTB7-Th: PC$_{70}$BM OSCs are shown in Figure 3.7. UA devices show highest EQE values than the corresponding EFTA and TA devices. TA devices show lowest EQE values. Low-EF treated devices show higher EQE values than TA devices reflecting the corresponding trend in the J$_{sc}$ of the devices, as shown in Table 3.4.

This increase in FF and J$_{sc}$ for EF(-) treated devices were further probed by studying the light-dependence on J$_{sc}$ of solar cells.

J-V characteristics of solar cells were studied at different light intensities using neutral density filters. Light intensities were initially calibrated with a standard silicon solar cell. Typical J-V characteristics obtained at different light intensities are shown in Figure 3.8a. J$_{sc}$ obtained at different light intensities is shown in log-log plot (Figure 3.8b). J$_{sc}$ has a logarithmic dependence on the light intensity I,[13-15]

$$J_{sc} = CI^{\alpha}(\alpha \leq 1) \tag{4.3}$$

The parameter α tells about bimolecular recombination in the solar cell device. $\alpha \approx 1$ implies negligible bimolecular recombination in the solar cell device. When $\alpha < 1$, signifies that bimolecular recombination increases in the device.[16, 17]
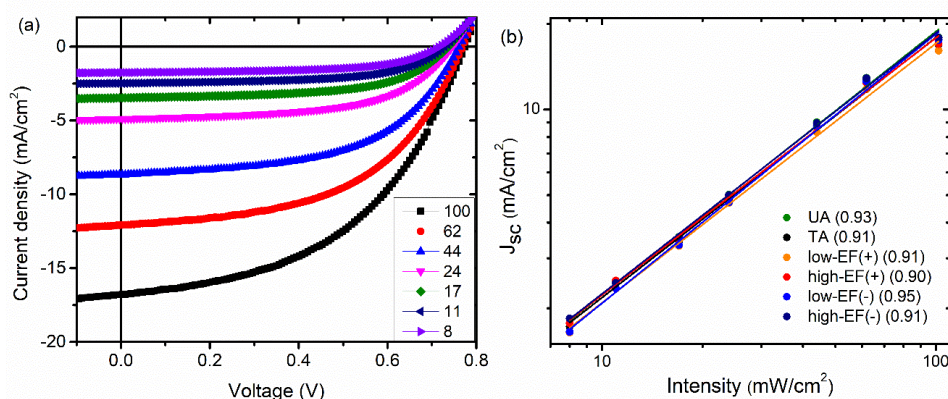
Figure 3.8 (a) Typical light-intensity dependence of J-V characteristics of PTB7-Th: $PC_{70}BM$ OSCs. Neutral density filters were used to vary the intensity of 1 sun illumination (AM 1.5 Global). Legends indicate light intensity in units of mW/cm^2. b) Jsc of EFTA treated and control PTB7-Th: $PC_{70}BM$ OSCs. Legends indicate typical α parameter obtained for EFTA treated and control devices.

α was obtained from the slope of the log-log plots of J_{sc} vs. light intensity. (from the above equation) The α obtained for control and EF treated devices are shown along with the legends in Figure 3.8b. For low-EF(-) treated devices, $\alpha \cong 0.95$ was obtained, which is higher than other EFTA treated and control devices. This observation implies that there is a reduction in bimolecular recombination in low-EF(-) treated devices. This is attributed to better percolation pathways for separated charge carriers.
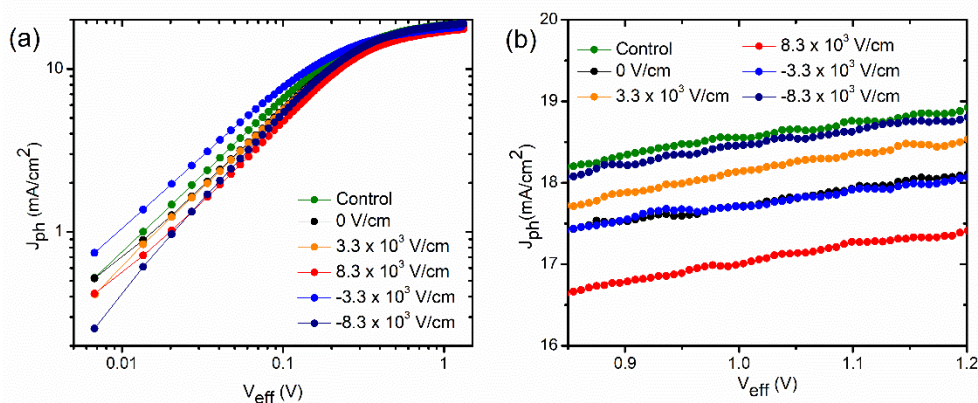
Figure 3.9 J_{ph} is plotted as a function of V_{eff} for PTB7-Th: $PC_{70}BM$ OSCs were measured at 1 sun illumination. (a) and (b) correspond to different V_{eff} ranges.

To gain further insight into charge collection efficiency, J_{ph} (J_{light}-J_{dark}) was studied as a function of V_{eff}. V_{eff} is given by V_o- $V_{applied}$, where V_o is the voltage at which J_{ph} becomes zero. The log-log plot of J_{ph} vs. V_{eff} is shown in Figure 3.9a. Higher J_{ph} is obtained for low-EF(-) devices even at very low V_{eff} range. This points towards better charge extraction of separated charge carriers in the active layer. For all the devices, J_{ph} saturates at around V_{eff} of 0.4 V. At high V_{eff}, all the generated e-h pairs are assumed to be dissociated and collected at the respective electrodes.
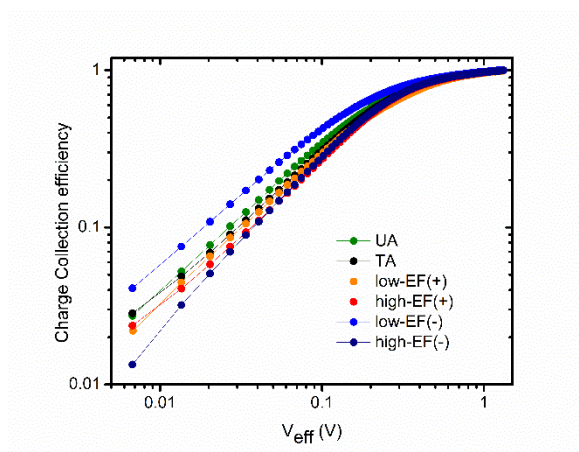
Figure 3.10 *Charge Collection efficiency of EFTA treated and control PTB7-Th: PC$_{70}$BM OSCs were measured at 1 sun illumination.*

Saturation J_{ph} (J_{sat}) reflects the total generated charge carriers i.e., interface area between donor and acceptor domains which acts as charge generation sites, is shown in Figure 3.9b. UA films have the highest J_{sat} reflecting maximum interface area because of the finer intermixing of donor and acceptor components in the active layer. Thermal annealing reduces the interface area between the components owing to the temperature-driven phase separation. High-EF(-) films also have a large interface area between the components since PC$_{70}$BM comes to the top of the film with EF(-) treatment. EF(+) treatment reduces the interface area between the components more than the control TA devices by gathering PC$_{70}$BM at the bottom of the active layer. Hence, high-EF(+) devices show the lowest J_{sat} values. J_{ph}/J_{sat} gives the charge collection efficiency of the solar cells devices and is plotted in Figure 3.10. Charge collection at lower V_{eff} is limited because of higher bimolecular recombination of separated charge carriers for all the devices. The charge collection efficiencies plotted also reflect the better optimized morphology of low-EF(-) devices when compared to other devices.

3.2.5 Electron mobility studies

EFTA treatment-induced vertical phase segregation in the active layer was further studied by SCLC electron mobility studies. Electron-only devices were fabricated with the following architecture ITO/ZnO (40 nm)/BHJ/ Al (100 nm). After EFTA (or TA) treatment of the BHJ film spin-coated on ZnO, the devices (electrode area $\approx$ 7 mm^2) were completed by thermal evaporation of 100 nm of Al at a base pressure of 10^{-6} mbar. J-V characteristics obtained for these devices in dark conditions exhibited space charge behaviour over a wide range and was fitted with the Mott-Gurney equation.

$$J = \frac{9}{8}\epsilon\mu_e\frac{V^2}{d^3} \tag{3.2}$$

Here, ε is permittivity of the active layer; μ_e is electron mobility of the charge carriers in the active layer and d is the thickness of the film respectively. μ_e obtained from several devices (>10 devices for each case) for PTB7-Th: PC$_{70}$BM BHJ system, as a function of EFTA treatment, is shown in Table 3.4.

Low-EF(-) treated devices exhibit higher μ_e when compared with other control and EFTA treated devices. This higher μ_e in the BHJ blends points towards better percolation pathways for electrons and enhanced ordering of PC$_{70}$BM molecules with low-EF(-) treatment. High-EF (+) and TA treatment leads to higher aggregation of PC$_{70}$BM at the bottom of the film, while High-EF(-) treatment increases fullerene fraction at the top of the film. The segregation of PC$_{70}$BM molecules at either film boundaries limits percolation pathways for charge carriers and hence reduces bulk μe.[18, 19]

Table 3.4 *Electron mobility obtained from PTB7-Th: PC$_{70}$BM BHJ devices in electron-only device architecture. Low-EF and high-EF refer to EFTA treated devices with EF strengths of 3.3 x 10^3 V/cm, and 8.3 × 10^3 V/cm, respectively. EF(+) and EF(-) correspond to positive and negative directions of polarity maintained during EFTA treatment, respectively.*

	Electron mobility (cm^2/Vs)
UA	$8.02\pm0.21\times10^{-4}$
TA	$6.14\pm0.32\times10^{-5}$
low-EF (+)	$4.03\pm0.27\times10^{-5}$
high-EF (+)	$2.76\pm0.34\times10^{-5}$
low-EF (-)	$1.22\pm0.16\times10^{-4}$
high-EF (-)	$2.57\pm0.19\times10^{-4}$

3.2.6 Photocurrent noise measurement
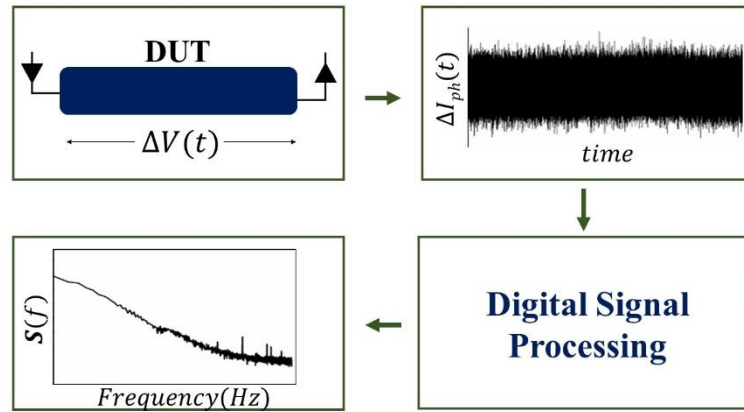
Figure 3.11 *Schematic of the photocurrent noise measurements.*

The reduction in charge transport barriers for low-EF(-) treated solar cell devices were further studied by photocurrent noise studies. Schematic of photocurrent noise measurement is shown in Figure 3.11. Fluctuations of photocurrent around a mean value for a constant steady light source will give insights regarding various processes occurring in the active layer, like charge generation, charge transport, and charge collection.[20-23] The fluctuations in photocurrent of a semiconductor are well described by Hooge's model.

$$S_I(f)/I^2 = \frac{\alpha_H}{f\,N} \tag{3.4}$$

Where $S_I(f)$ is the current fluctuation, f is the frequency, N is the carrier concentration, and α_H is the Hooge's parameter. The photocurrent noise fluctuations could be either due to fluctuations in carrier concentration or fluctuations in carrier mobility. Hooge's model is more suited to explain photocurrent fluctuations arising from fluctuations in mobility.

It is a common practice to visualize photocurrent noise spectra as power spectral density (PSD). Time series data of the photocurrent fluctuations are initially obtained from the device exposed to a steady-state light source. PSD is the power or variance distributed in the frequency domain. Mathematically, it is defined as the Fourier transform of the autocorrelation function. The autocorrelation function can be used for i) detecting non-randomness in data, ii) identifying an appropriate time series model if the data is not random. For measurements $x_1, x_2, ..., x_N$ at time $t_1, t_2, ..., t_N$ the lag k autocorrelation function is defined as

$$r_k = \frac{\sum_i (x_i - x_{mean})(x_{i+k} - x_{mean})}{\sum_i (x_i - x_{mean})^2} \tag{3.5}$$

Here i = 1, 2, …, N. The PSD is given by

$$S(f) = \int_{-\infty}^{\infty} r_k e^{-2\pi i f k} dk \qquad (3.6)$$
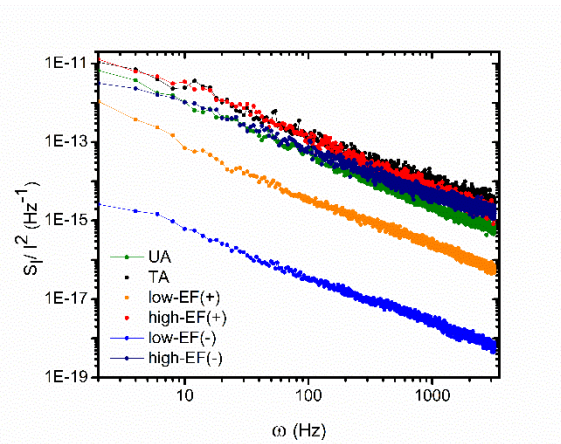
Figure 3.12 *Photocurrent noise spectra (arrived from time-series measurements using dynamic signal analyser ~10^4 samples/s for 40 s, under steady-state dc light levels of ~ 10 mW/cm^2) at 300 K of EF treated and control devices of PTB7-Th: PC$_{70}$BM. Dark background signal was < 10^{-20} A2/Hz for these devices.*

Information obtained from the photocurrent noise technique, pioneered in our laboratory have been used for understanding charge transport and stability in BHJ solar cells and perovskite solar cells. This sensitive technique was used to examine EFTA treated BHJ solar cells. Typical photocurrent noise spectra obtained for control and EFTA treated devices are shown in Figure 3.12. Main results from the photocurrent noise measurements are summarized in Table 3.5.

The NPSD of all the devices shows typical $1/f^\gamma$ behaviour. The parameter γ and the frequency range over which the $1/f^\gamma$ behaviour have been correlated to microscopic parameters in the active layer of the solar cell. Typical values of γ ~1.2 are obtained for all the devices, usually obtained for organic BHJ solar cells. UA, TA, high-EF(+) and high-EF(-) devices show higher NPSD. Comparing NPSD values of control and EFTA treated devices at ω = 2 Hz, it was observed that Low-EF(-) treated devices (2.6 x 10^{-15} Hz^{-1}) have values three orders lesser than the control UA devices (6.6 x 10^{-12} Hz^{-1}). The lower intensity of NPSD for the low-EF(-) treated devices show that there is a reduced barrier for charge transport and better stability in the active layer.

Table 3.5 *Normalized PSD values of various devices at 2 Hz and the frequency exponent calculated by fitting to Hooge's model.*

	S_I/I^2 Hz^{-1} (at 2 Hz)	γ
UA	6.63 x 10^{-12}	1.24
TA	1.08 x 10^{-11}	1.15
low-EF (+)	1.08 x 10^{-12}	1.21
high-EF (+)	1.3 x 10^{-11}	1.26
low-EF (-)	2.6 x 10^{-15}	1.17
high-EF (-)	3.15 x 10^{-12}	1.05

3.2.7 Stability studies

The long-term stability of solar cells was studied by degradation measurements. The devices were stored in dark and ambient conditions, without encapsulation after the first device characterization. J-V characteristics under 1sun illumination are studied at regular intervals of time. The normalized solar cell parameters as a function of aging time, obtained for UA, TA, and low-EF(-) treated devices are shown in Figure 3.13. For the control devices, it can be seen that all the solar cell parameters reduce drastically with aging time. PCE of these devices reduces to less than 10% of its initial value in the first 250 hours of study. While TA and low-EF(-) treated devices maintain close to 75% of its maximum efficiency in the first 260 hours of the degradation study. This stability of TA and EFTA treated devices is attributed to the removal of the additive DIO during the thermal annealing treatment. It should be noted that low-EF(-) devices have efficiencies higher than the control TA devices.

It is noticed that EFTA treatment serves as an external control parameter to tailor a vertical phase separation of active layer components in the amorphous donor BHJ film, and can compensate the effects of thermal annealing treatment and additive treatment. This was shown using a comprehensive analysis carried out during GIWAXS measurements and water contact angle measurements. By careful optimization, EFTA treated devices were shown to have efficiencies higher than thermally annealed devices. Series of studies were carried out to explore the increase in device performance with EFTA treatment. The results from these studies point towards optimized vertical phase segregation in the active layer due to the EFTA treatment. This leads to better percolation pathways for separated charge carriers and reduced bimolecular recombination in the blend film. Removal of DIO additive during thermal treatment has led to more stable devices. TA and EFTA treated devices retained close to 75% of its maximum efficiency over a period of 250 hours, while the efficiency of initially high

performing untreated control devices dropped to 10% of its maximum efficiency. EFTA treatment allows the fabrication of stable solar cells where efficiency loss due to thermal treatment is sufficiently overcome.
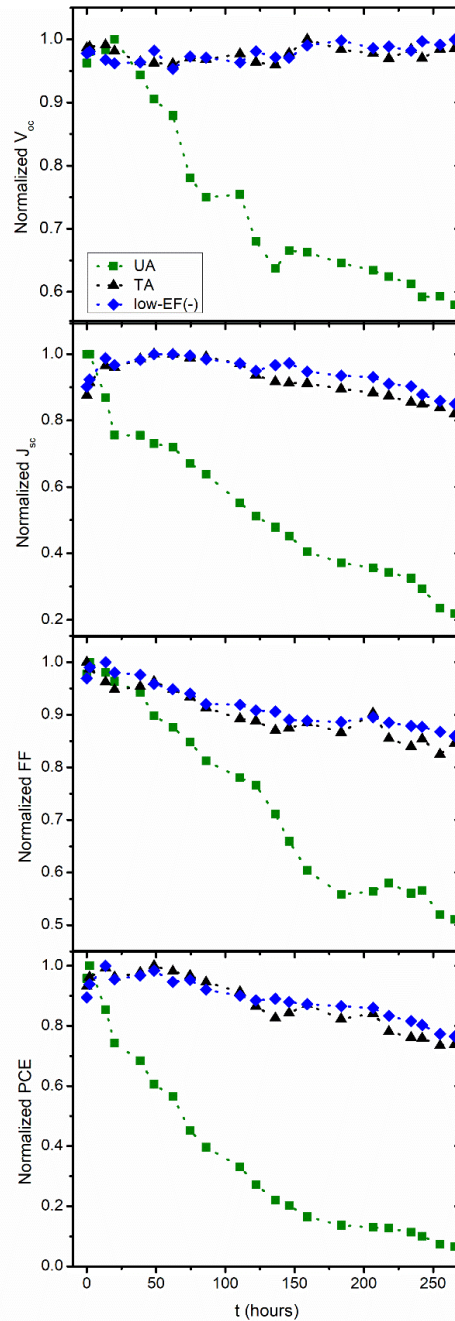
Figure 3.13. *Normalized Solar cell parameters of PTB7-Th: PC$_{70}$BM OSCs are shown as a function of aging time (t) in hours. Devices were stored in dark and ambient conditions without encapsulation, after the first measurement.*

3.3 Summary
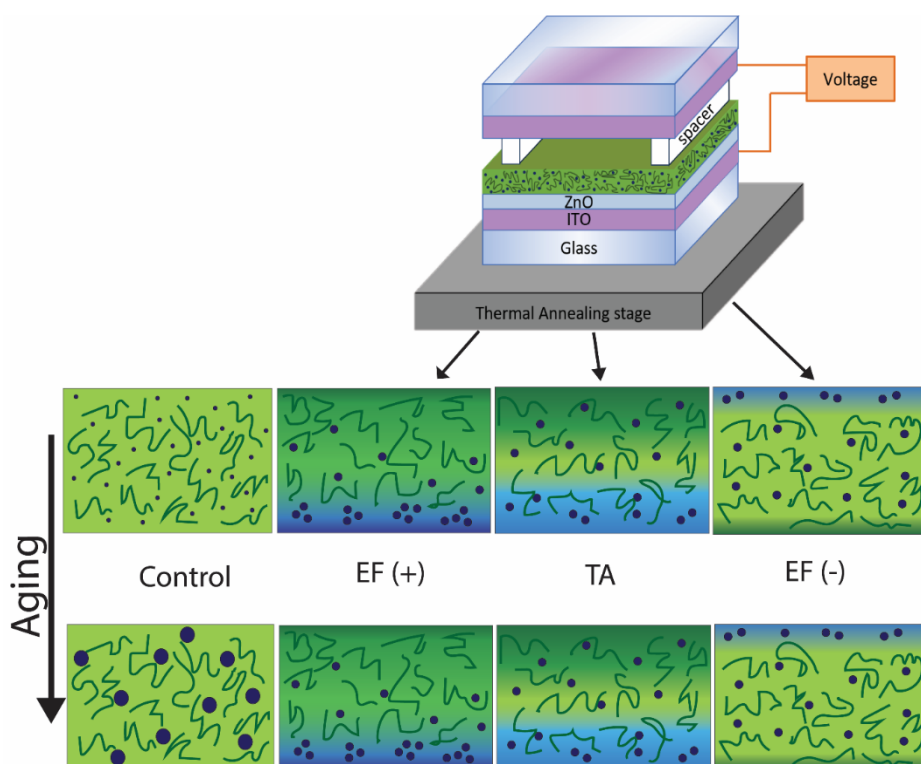
Figure 3.14 *Schematic shows how EFTA treatment, depending on the direction of the electric field applied during the treatment, is able to control vertical phase segregation in the active layer. Blue circles correspond to PC$_{70}$BM aggregates, and green wiggly lines correspond to PTB7-Th polymer. For the untreated control UA films, aging increases PC$_{70}$BM domain sizes. For the thermally treated films, the morphology remains consistent over time. EF(+) treatment (EF(-) treatment) increases PC$_{70}$BM segregation to the bottom (top) of the active layer film.*

EFTA treatment has shown to be effective in controlling the morphology of amorphous donor-based BHJ system of PTB7-Th: PC$_{70}$BM. By tuning the EFTA treatment parameters, solar cells more efficient than corresponding thermally annealed devices and more stable than control untreated devices were fabricated. Typical schematic of morphology control of the active layer with EFTA treatment is shown in Figure 3.14.

References

1.   Liang, Y.; Xu, Z.; Xia, J.; Tsai, S.-T.; Wu, Y.; Li, G.; Ray, C.; Yu, L., For the Bright Future—Bulk Heterojunction Polymer Solar Cells with Power Conversion Efficiency of 7.4%. *Advanced Materials* **2010,** *22* (20), E135-E138.

2.	Zhang, S.; Ye, L.; Zhao, W.; Liu, D.; Yao, H.; Hou, J., Side Chain Selection for Designing Highly Efficient Photovoltaic Polymers with 2D-Conjugated Structure. *Macromolecules* **2014,** *47* (14), 4653-4659.

3.	Liao, H.-C.; Ho, C.-C.; Chang, C.-Y.; Jao, M.-H.; Darling, S. B.; Su, W.-F., Additives for morphology control in high-efficiency organic solar cells. *Materials Today* **2013,** *16* (9), 326-336.

4.	Lee, J. K.; Ma, W. L.; Brabec, C. J.; Yuen, J.; Moon, J. S.; Kim, J. Y.; Lee, K.; Bazan, G. C.; Heeger, A. J., Processing Additives for Improved Efficiency from Bulk Heterojunction Solar Cells. *Journal of the American Chemical Society* **2008,** *130* (11), 3619-3623.

5.	Lou, S. J.; Szarko, J. M.; Xu, T.; Yu, L.; Marks, T. J.; Chen, L. X., Effects of Additives on the Morphology of Solution Phase Aggregates Formed by Active Layer Components of High-Efficiency Organic Solar Cells. *Journal of the American Chemical Society* **2011,** *133* (51), 20661-20663.

6.	Tremolet de Villers, B. J.; O'Hara, K. A.; Ostrowski, D. P.; Biddle, P. H.; Shaheen, S. E.; Chabinyc, M. L.; Olson, D. C.; Kopidakis, N., Removal of Residual Diiodooctane Improves Photostability of High-Performance Organic Solar Cell Polymers. *Chemistry of Materials* **2016,** *28* (3), 876-884.

7.	Limbu, S.; Pont, S.; Doust, A. B.; Kwon, S.; Fuller, P.; Tan, E.; Durrant, J. R.; Kim, J.-S., Impact of Initial Bulk-Heterojunction Morphology on Operational Stability of Polymer:Fullerene Photovoltaic Cells. *Advanced Materials Interfaces* **2019,** *6* (6), 1801763.

8.	Ye, L.; Jing, Y.; Guo, X.; Sun, H.; Zhang, S.; Zhang, M.; Huo, L.; Hou, J., Remove the Residual Additives toward Enhanced Efficiency with Higher Reproducibility in Polymer Solar Cells. *The Journal of Physical Chemistry C* **2013,** *117* (29), 14920-14928.

9.	Agostinelli, T.; Lilliu, S.; Labram, J. G.; Campoy-Quiles, M.; Hampton, M.; Pires, E.; Rawle, J.; Bikondoa, O.; Bradley, D. D. C.; Anthopoulos, T. D.; Nelson, J.; Macdonald, J. E., Real-Time Investigation of Crystallization and Phase-Segregation Dynamics in P3HT:PCBM Solar Cells During Thermal Annealing. *Advanced Functional Materials* **2011,** *21* (9), 1701-1708.

10.	Komilian, S.; Oklobia, O.; Sadat-Shafai, T., Controlling intercalations of PBDTTT-EFT side chain to initiate suitable network for charge extraction in PBDTTT-EFT:PC71BM blended bulk heterojunction solar cell. *Solar Energy Materials and Solar Cells* **2018,** *175*, 35-40.

11.   Huang, D. M.; Mauger, S. A.; Friedrich, S.; George, S. J.; Dumitriu-LaGrange, D.; Yoon, S.; Moulé, A. J., The Consequences of Interface Mixing on Organic Photovoltaic Device Characteristics. *Advanced Functional Materials* **2011,** *21* (9), 1657-1665.

12.   Kim, M.; Lee, J.; Jo, S. B.; Sin, D. H.; Ko, H.; Lee, H.; Lee, S. G.; Cho, K., Critical factors governing vertical phase separation in polymer–PCBM blend films for organic solar cells. *Journal of Materials Chemistry A* **2016,** *4* (40), 15522-15535.

13.   Riedel, I.; Parisi, J.; Dyakonov, V.; Lutsen, L.; Vanderzande, D.; Hummelen, J. C., Effect of Temperature and Illumination on the Electrical Characteristics of Polymer–Fullerene Bulk-Heterojunction Solar Cells. *Advanced Functional Materials* **2004,** *14* (1), 38-44.

14.   Schilinsky, P.; Waldauf, C.; Brabec, C. J., Recombination and loss analysis in polythiophene based bulk heterojunction photodetectors. *Applied Physics Letters* **2002,** *81* (20), 3885-3887.

15.   van Duren, J. K. J.; Yang, X.; Loos, J.; Bulle-Lieuwma, C. W. T.; Sieval, A. B.; Hummelen, J. C.; Janssen, R. A. J., Relating the Morphology of Poly(p-phenylene vinylene)/Methanofullerene Blends to Solar-Cell Performance. *Advanced Functional Materials* **2004,** *14* (5), 425-434.

16.   Gupta, V.; Kyaw, A. K. K.; Wang, D. H.; Chand, S.; Bazan, G. C.; Heeger, A. J., Barium: An Efficient Cathode Layer for Bulk-heterojunction Solar Cells. *Scientific Reports* **2013,** *3*, 1965.

17.   Kyaw, A. K. K.; Wang, D. H.; Gupta, V.; Leong, W. L.; Ke, L.; Bazan, G. C.; Heeger, A. J., Intensity Dependence of Current–Voltage Characteristics and Recombination in High-Efficiency Solution-Processed Small-Molecule Solar Cells. *ACS Nano* **2013,** *7* (5), 4569-4577.

18.   Bartelt, J. A.; Beiley, Z. M.; Hoke, E. T.; Mateker, W. R.; Douglas, J. D.; Collins, B. A.; Tumbleston, J. R.; Graham, K. R.; Amassian, A.; Ade, H.; Fréchet, J. M. J.; Toney, M. F.; McGehee, M. D., The Importance of Fullerene Percolation in the Mixed Regions of Polymer–Fullerene Bulk Heterojunction Solar Cells. *Advanced Energy Materials* **2013,** *3* (3), 364-374.

19.   Yazmaciyan, A.; Stolterfoht, M.; Burn, P. L.; Lin, Q.; Meredith, P.; Armin, A., Recombination Losses Above and Below the Transport Percolation Threshold in Bulk Heterojunction Organic Solar Cells. *Advanced Energy Materials* **2018,** *8* (18), 1703339.

20.   Hooge, F. N.; Kleinpenning, T. G. M.; Vandamme, L. K. J., Experimental studies on 1/f noise. *Reports on Progress in Physics* **1981,** *44* (5), 479-532.

21.   Bag, M.; Vidhyadhiraja, N. S.; Narayan, K. S., Fluctuations in photocurrent of bulk heterojunction polymer solar cells—A valuable tool to understand microscopic and degradation processes. *Applied Physics Letters* **2012,** *101* (4), 043903.

22.   Singh, A.; Nayak, P. K.; Banerjee, S.; Wang, Z.; Wang, J. T.-W.; Snaith, H. J.; Narayan, K. S., Insights Into the Microscopic and Degradation Processes in Hybrid Perovskite Solar Cells Using Noise Spectroscopy. *Solar RRL* **2018,** *2* (1), 1700173.

23.   Barone, C.; Lang, F.; Mauro, C.; Landi, G.; Rappich, J.; Nickel, N. H.; Rech, B.; Pagano, S.; Neitzert, H. C., Unravelling the low-temperature metastable state in perovskite solar cells by noise spectroscopy. *Scientific Reports* **2016,** *6*, 34675.

Chapter 4

Electric Field Assisted Thermal Annealing (EFTA) Treatment of Small Molecule Donor-Based and Non-Fullerene Acceptor-Based Solar Cells

There is a recent surge in efficiencies of organic solar cells with the replacement of fullerene-based acceptors by non-fullerene-based acceptors. [1-3] This improvement is primarily due to reduced V_{oc} losses in these BHJ systems and improved range of absorption. It is expected that the non-spherical symmetry offered by these acceptor molecules may be suited for electric field-assisted thermal annealing (EFTA) procedure. This treatment may be able to control the morphology of these new BHJ systems and in the process, improve the efficiencies beyond the current values.

In the earlier chapters, it was assumed that long-chain polymers do not directly respond to EFTA treatment due to the conformational constraints. The vertical phase segregation due to EFTA treatment is expected to be due to subtle changes introduced in the active layer. Studying EFTA treatment by replacing long-chain polymer donors with a small-molecule donor can help us in understanding the universality of the EFTA treatment.

Hence, in this chapter, EFTA treatment studies of two types of systems are studied:

i)   Polymer donor: non-fullerene acceptor based BHJ system
ii)   Small molecule donor: fullerene acceptor based BHJ system

4.1 Active layer components

The polymer donor and non-fullerene acceptor system chosen was PBDB-T-based polymers and ITIC-based small molecules. The small molecule donor chosen for EFTA treatment with $PC_{70}BM$ acceptor was SA48.
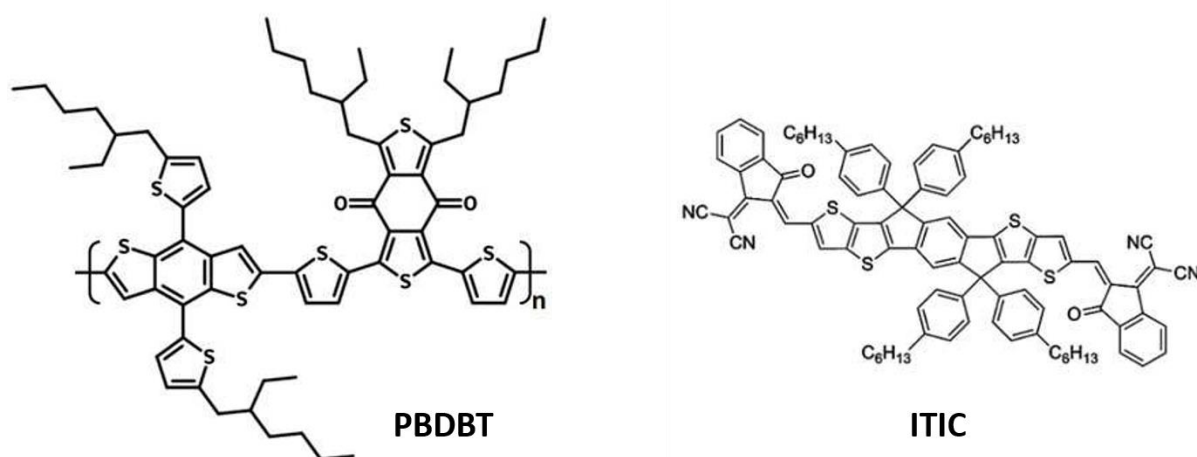
Figure 4.1 *Molecular structures of PBDBT and ITIC molecules.*

Poly[(2,6-(4,8-bis(5-(2-ethylhexyl)thiophen-2-yl)-benzo[1,2-b:4,5-b']dithiophene))-alt-(5,5-(1',3'-di-2-thienyl-5',7'-bis(2-ethylhexyl)benzo[1',2'-c:4',5'-c']dithiophene-4,8-dione)] (PBDB-T) is one of the high performing polymer donor.[4-6] It has HOMO and LUMO levels of -5.33 eV and -2.92 eV respectively. Poly[(2,6-(4,8-bis(5-(2-ethylhexyl-3-chloro)thiophen-2-yl)-benzo[1,2-b:4,5-b']dithiophene))-alt-(5,5-(1',3'-di-2-thienyl-5',7'-bis(2-ethylhexyl)benzo[1',2'-c:4',5'-c']dithiophene-4,8-dione)] (PBDBT-2Cl) is chlorinated derivative of donor polymer molecule PBDBT.[7-9] It has HOMO and LUMO levels of -5.52 eV and -3.57 eV respectively. This class of polymer donors are routinely used in conjugation with non-fullerene acceptor molecules.

3,9-bis(2-methylene-(3-(1,1-dicyanomethylene)-indanone))-5,5,11,11-tetrakis(4-hexylphenyl)-dithieno[2,3-d:2',3'-d']-s-indaceno[1,2-b:5,6-b']dithiophene (ITIC) is high efficient non-fullerene molecule with strong absorption characteristics from visible to infrared spectra.[10-12] HOMO and LUMO levels of this molecule are -5.48 eV and -3.83 eV respectively. It was the first small molecule to outperform fullerene acceptors in solar cell device efficiency. 3,9-bis(2-methylene-((3-(1,1-dicyanomethylene)-6,7-difluoro)-indanone))-5,5,11,11-tetrakis(4-hexylphenyl)-dithieno[2,3-d:2',3'-d']-s-indaceno[1,2-b:5,6-b']dithiophene (IT-4F) is a fluorinated derivative of ITIC acceptor molecule.[13] HOMO and LUMO levels of this molecule are -5.66 eV and -4.14 eV respectively. These acceptor molecules have also been found to be more stable than fullerene-based acceptors.
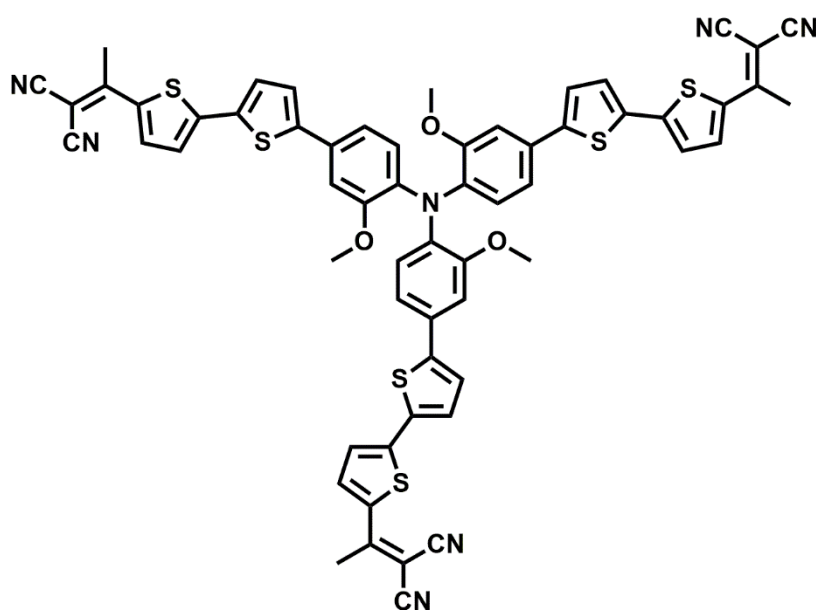

Figure 4.2 *Molecular structure of SA48 molecule.*

Solar cells with PBDB-T as donor and ITIC as acceptor have obtained efficiencies as high as 11% and shown high thermal stability.[5] Solar cells with PBDBT-2Cl as donor and IT4F as acceptor have reached efficiencies as high as 14%.[9] Molecular structures of PBDB-T and ITIC molecules are shown in Figure 4.1.

The small molecule donor chosen was tris{4-[5'-(1,1,-dicyanoprop-1-en-2-yl)-2,2'-bithien-5-yl]-2-methoxyphenyl} amine (SA48) molecule . SA48 donor small molecule was obtained from Prof. Sergei Ponomorenko's lab at Enikolopov Institute of Synthetic Polymeric Materials, Moscow. SA48 molecule (Figure 4.2) is one among the class of star-shaped donor molecules with triphenylamine donor core, with thiophene conjugated spacers and dicyanovinyl acceptor groups.[14-18] They are usually low-bandgap molecules and are usually amorphous in the thin-film state. Blending with $PC_{70}BM$ acceptor molecules, efficiencies as high as 5% have been obtained for this class of donor molecules.

4.2 Dipole moment calculations

The dipole moment parameter captures the response of a molecule to an external electric field. Molecules have the origin of dipole moments in the non-uniform distributions of positive and negative charges on the various atoms. It has been reported that the dipole moment of the active layer components is crucial in dictating charge separation, intermolecular interactions, crystallization properties, and the blended microscopic morphology.[19, 20]
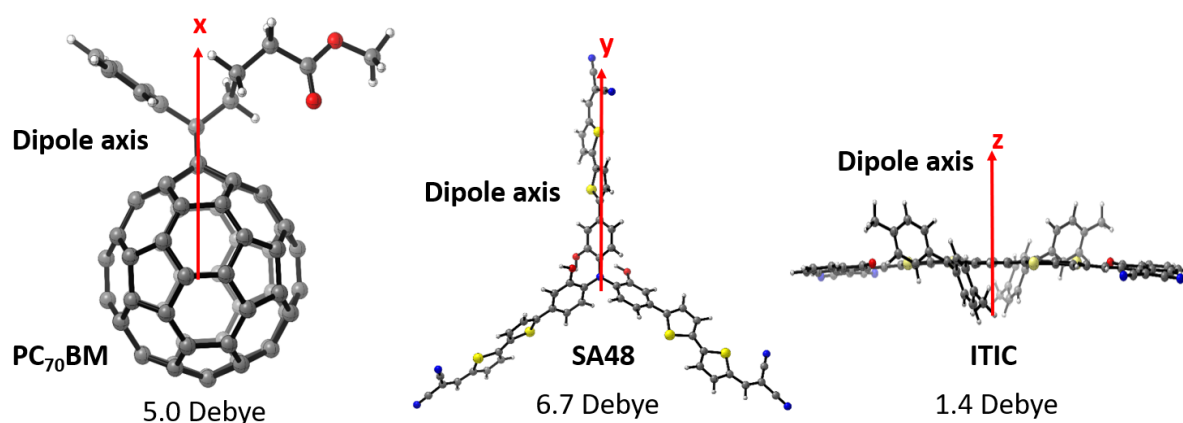
Figure 4.3 Dipole moments and dipole axis obtained for $PC_{70}BM$, SA48, and ITIC molecules through DFT calculations.

Dipole moment calculations were carried out using Density Functional Theory (DFT). The calculations were carried out by Dr. Ayan Dutta's group at Indian Association for the Cultivation Of Science, Kolkatta. B3LYP functional and 6-31 G(d,p) basis set was used for the

DFT calculations.[21, 22] For ground state optimization, B3LYP is the most robust functional for structure-property correlations. 6-31 G(d,p) describe the Gaussian basis set used to construct the atomic orbitals for computation. These are calculations in the gas phase, and the electric field magnitude used in these simulations are several orders higher in magnitude than used in experimental conditions.

The obtained dipole moments and the dipole axis of these small molecules are shown in Figure 4.3. From the results, it is clear that it is the small molecule donor SA48 has a higher dipole moment (6.7 Debye) than $PC_{70}BM$ molecule (5.0 Debye), whereas NFA molecule (ITIC) has the smallest dipole moment (1.4 Debye) among the three molecules studied.

EFTA treatment was carried out on both the BHJ systems as discussed in the earlier chapters, with the temperature of annealing as 140 °C maintained for 10 minutes. EF strength maintained was 8.3×10^3 V/cm. EF(+) treatment implies the positive terminal of the voltage source was connected to the bottom electrode and the top electrode was left grounded during EFTA treatment. EF(-) treatment implies the positive terminal of the voltage source was connected to the top electrode and the bottom electrode was left grounded during EFTA treatment. TA corresponds to the thermally annealed control devices.

4.3 EFTA treatment of polymer donor: non-fullerene acceptor based BHJ system

BHJ blend solutions were fabricated with the donor: acceptor in the ratio 1:1 with 10 mg/ml polymer concentration, in chlorobenzene solvent with 0.5% di-iodo-octane (DIO) additive. The blend solution was kept stirring at 55 °C for more than 8 hours. It was spin-coated on substrates when the solution was at room temperature, at 1000 rpm for 60 seconds in inert conditions. ITO- substrates and ZnO-coated ITO substrates were used depending on the requirement, with the latter case for the fabrication of inverted solar cells.

4.3.1 Absorbance studies

The normalized absorption spectra of PBDBT: ITIC thin films are shown in Figure 4.4. The resultant spectra obtained from the blend film is due to the overlapping spectra of both the polymer and small molecule. The peak at 610 nm is due to the main peak of PBDBT polymer and shoulder peak of ITIC small molecule. The peak at 670 nm is solely due to ITIC molecule. It was verified by pristine ITIC films and is in agreement with reported value.[23] It was observed that the absorption spectra did not vary with EFTA treatment. Spectra obtained for EFTA

treated thin films and control thin films revealed an almost complete overlap of the spectral response in the entire wavelength range.
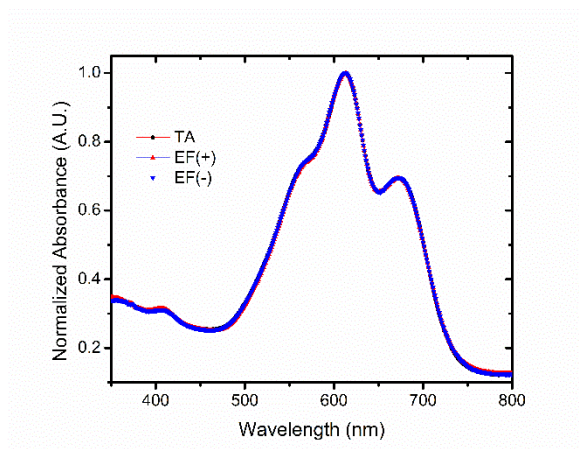
Figure 4.4 Normalized absorption spectra of control and EFTA treated PBDBT: ITIC blend films. The thickness of the films was ≈ 150 nm. All the films were coated on ITO substrates for absorption studies. TA indicates Thermally annealed BHJ films. EF(+) and EF(-) indicates EFTA treated BHJ in positive and negative directions, respectively (EF strength $\cong 8.3 \times 10^3$ V/cm).Absorption studies of thin films were carried out using Perkin Elmer UV/Vis/NIR Lambda 750 Spectrometer.

4.3.2. Water contact angle measurements
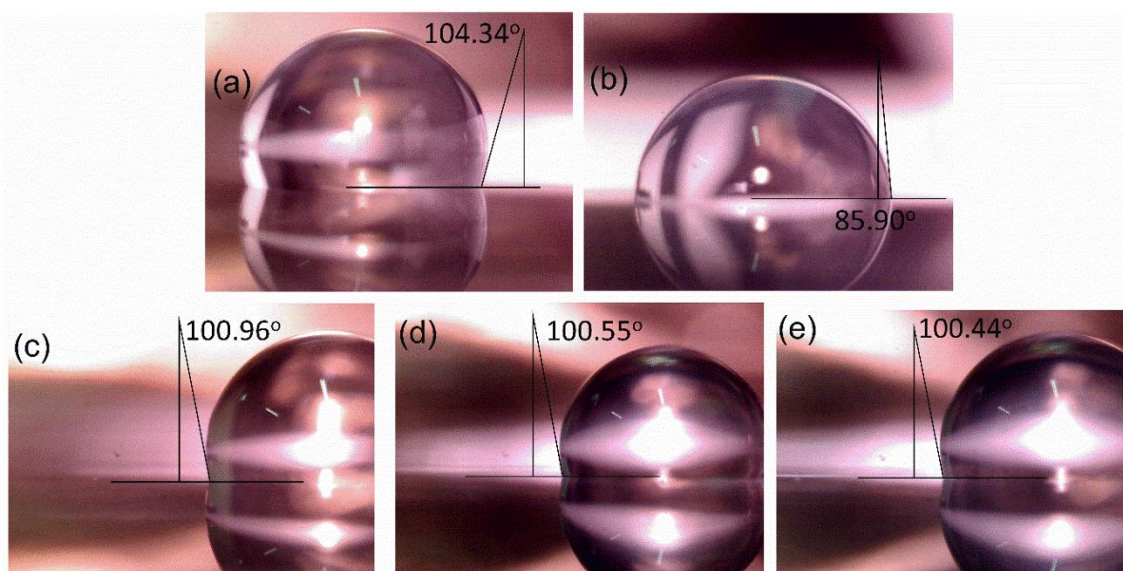
Figure 4.5 Representative images of water contact angle measurements on thin films of a) PBDBT (pristine) b) ITIC (pristine) c) Control TA (BHJ Blend) d) EF(+) (BHJ Blend) e) EF(-) (BHJ Blend). TA corresponds to thermally annealed control samples, respectively. EF(+) and

EF(-) refers to EFTA treated samples in positive and negative directions, respectively (EF strength≅ 8.3 × 10³ V/cm).

Water contact angles were measured for pristine films, control, and EFTA treated BHJ films to obtain more information about the top of the film. Contact angles (θ_c) were obtained from measurements at different locations on the sample films and averaged. Typical water contact images obtained and the averaged contact values obtained for all the cases are shown in Figure 4.5. Pristine donor polymer surface ($\theta_c \approx 104.34°$) was found to be relatively more hydrophobic than pristine acceptor surface ($\theta_c \approx 85.90°$). Irrespective of TA or EFTA treatments, all the blend films showed θ_c close to 100°. Using the Cassie-Baxter equation (eq (3.1)),[24, 25] the polymer donor fraction on the top surface was found to be ≈ 80%, for all the blend films, indicating a donor-rich top surface. It was observed that EFTA treatment does not bring any discernible change to the donor fraction at the air-BHJ interface.
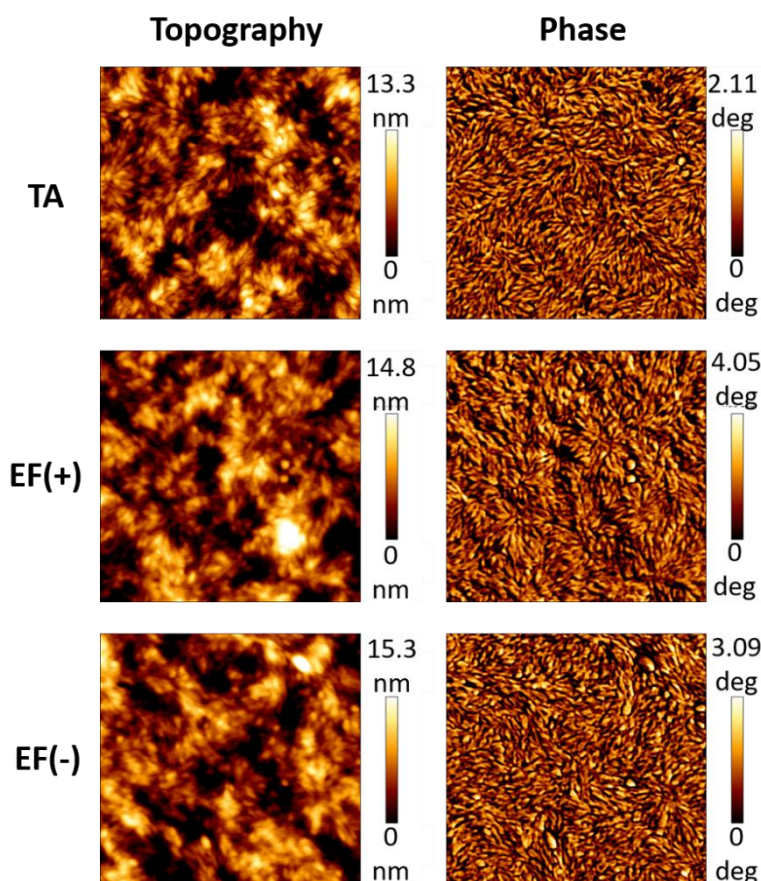
***Figure 4.6** Typical topography and phase AFM images (1.5 μm x 1.5 μm) of PBDBT: ITIC BHJ thin films. TA corresponds to thermally annealed films. EF(+) and EF(-) corresponds to*

EFTA treated films with positive and negative directions of polarity, respectively. EF strength $\approx 8.3x10^3$ V/cm. Experimental setup is described in the caption of Figure 2.6.

4.3.3 Atomic force microscopy (AFM) imaging

The air-BHJ interface of control and EFTA treated PBDBT: ITIC films were examined by AFM. Typical topography and phase images of 10 μm x 10 μm of the BHJ films are shown in Figure 4.6. The topography and phase images indicate needle-like features. No apparent change in the surface morphology with EFTA treatment was observed. The roughness$_{RMS}$ of the AFM images which was found to be close to 7 nm, remained independent on the EFTA treatment.

4.3.4 Solar cell characteristics
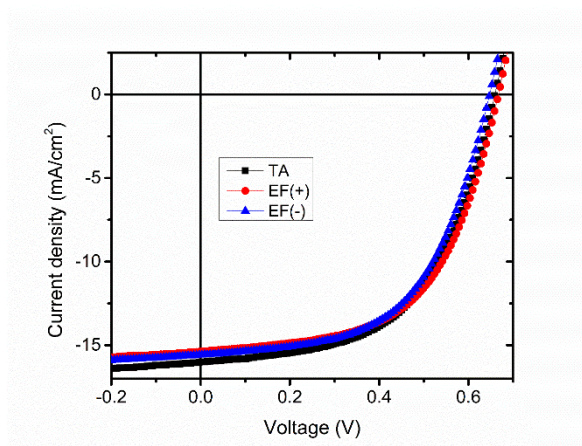
Figure 4.7 *Typical J-V characteristics of PBDBT-Cl: IT4F BHJ solar cells under 1 sun light illumination. TA corresponds to thermally annealed control devices. EF(+) and EF(-) corresponds to EFTA treated devices with positive and negative directions of polarity, respectively. EF strength $\approx 8.3x10^3$ V/cm. Experimental setup is described in the caption of Figure 2.8.*

Solar cells were fabricated after the EFTA treatment was carried out on the active layer. Solar cells were fabricated in inverted-device architecture (ITO/ZnO (40nm) /BHJ/MoOx (10 nm)/Ag (100 nm)). Donor: Acceptor system of PBDBT-2Cl and IT-4F were used for this study as it was relatively more efficient than PBDBT: ITIC BHJ system. Typical J-V characteristics under 1 sun illumination and solar cell parameters obtained from a large set of solar cells (> 10 devices for each case) are shown in Figure 4.7 and Table 4.1, respectively, as a function of EFTA treatment. This specific BHJ systems based on these components have been reported to exhibit efficiencies as high as 14%. These values were not observed in our studies. It should

be noted that the devices fabricated were not optimized for all the processing parameters. Since the objective of these studies was to see if this system responds to EFTA treatment, a standardized set of control devices which were reproducible consistently were used for the studies. However, no discernible change in device performance with respect to the EFTA treatment was observed. Similar results and trends were obtained for the solar cell fabricated from BHJ system of PBDBT: ITIC.

Table 4.1 *Typical solar cell parameters obtained for PBDBT-2Cl: IT4F solar cells under 1 sun illumination. TA corresponds to the thermally annealed control device. EF(+) and EF(-) correspond to EFTA treated devices, with positive and negative directions of polarity maintained during the treatment, respectively. EF strength ≈ 8.3 × 10³ V/cm.*

	V_{oc} (V)	J_{sc} (mA/cm^2)	Fill Factor (%)	Efficiency (%)
TA	0.66±0.02	15.85±0.26	55.68±0.54	5.85±0.35
EF(+)	0.66±0.00	15.05±0.16	57.39±0.17	5.69±0.07
EF(-)	0.65±0.01	15.57±0.09	55.27±1.26	5.57±0.21

Based on the extensive set of devices fabricated and studied it can be concluded from these studies that the BHJ system of PBDBT-based polymers and ITIC-based acceptors does not show any response to the EFTA treatment (at least for the range of standard processing parameters used for fabrication). The study on this class of BHJ systems shows that EFTA treatment may not always be effective. The absence of change in morphology of active layer films with EFTA is also consistent with the trends in the device performance. To further explore different ranges and dependencies of EFTA treatment, studies were extended to BHJ system of small molecule donor and fullerene acceptors.

4.4 EFTA treatment of small-molecule donor: fullerene acceptor- based BHJ system

BHJ blend solutions were fabricated with the donor: acceptor in the ratio 1:2 with dichlorobenzene solvent with 4% di-iodo-octane (DIO) additive. The 24 mg/ml solution was kept stirring at 55 °C for more than 8 hours. It was spin-coated on substrates when the solution was at room temperature, at 700 rpm for 60 seconds in inert conditions. The solution was spin-

coated on ITO- substrates for thin-film studies and ZnO-coated ITO substrates for solar cells studies.

4.4.1 Absorbance studies

From the normalized absorption spectra (Figure 4.8), it can be seen that there is no significant change with respect to EFTA treatment when compared to control samples of thermally annealed films (TA). The spectra in the visible region are mainly dominated by the SA48 small molecule. SA48 molecule has shown to be amorphous in thin films blended with $PC_{70}BM$. It can be inferred that SA48 packing does not alter with EFTA treatment.
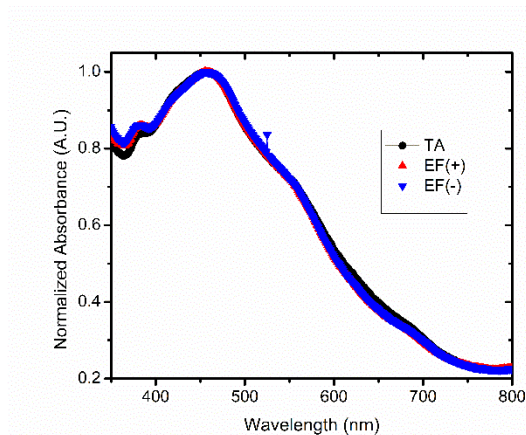
Figure 4.8 *Normalized absorption spectra of control and EFTA treated SA48: $PC_{70}BM$ blend films. The thickness of the films was ≈ 150 nm. All the films were coated on ITO substrates for absorption studies. TA indicates Thermally annealed BHJ films. EF(+) and EF(-) indicates EFTA treated BHJ in positive and negative directions, respectively (EF strength $\cong 8.3 \times 10^3$ V/cm).Absorption studies of thin films were carried out using Perkin Elmer UV/Vis/NIR Lambda 750 Spectrometer.*

4.4.2 Surface characterization

Water contact measurements were carried out to investigate the air-BHJ interface of the active films. The water contact angles of the pristine films of SA48 and $PC_{70}BM$ (shown in Figure 4.9) and the corresponding blend films yielded similar contact angles. Hence, water contact angle measurements could be used to track the variation in the donor fraction with EFTA treatment.
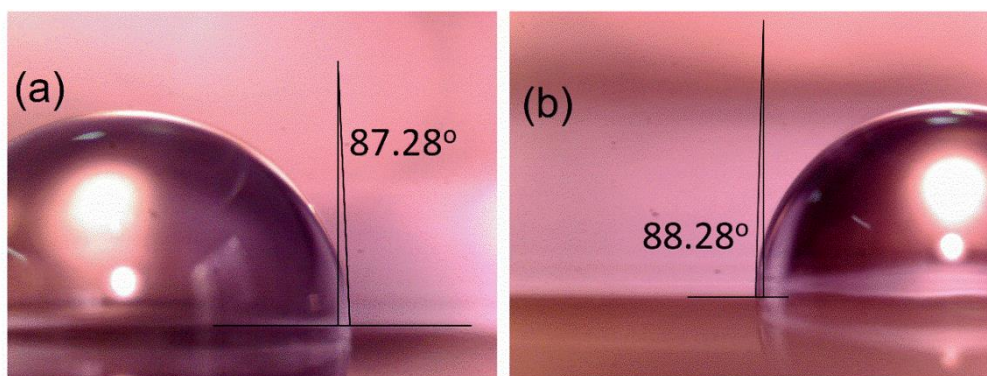
Figure 4.9 *Representative images of water contact angle measurements on thin films of a) SA48 (pristine) b) PC₇₀BM (pristine).*
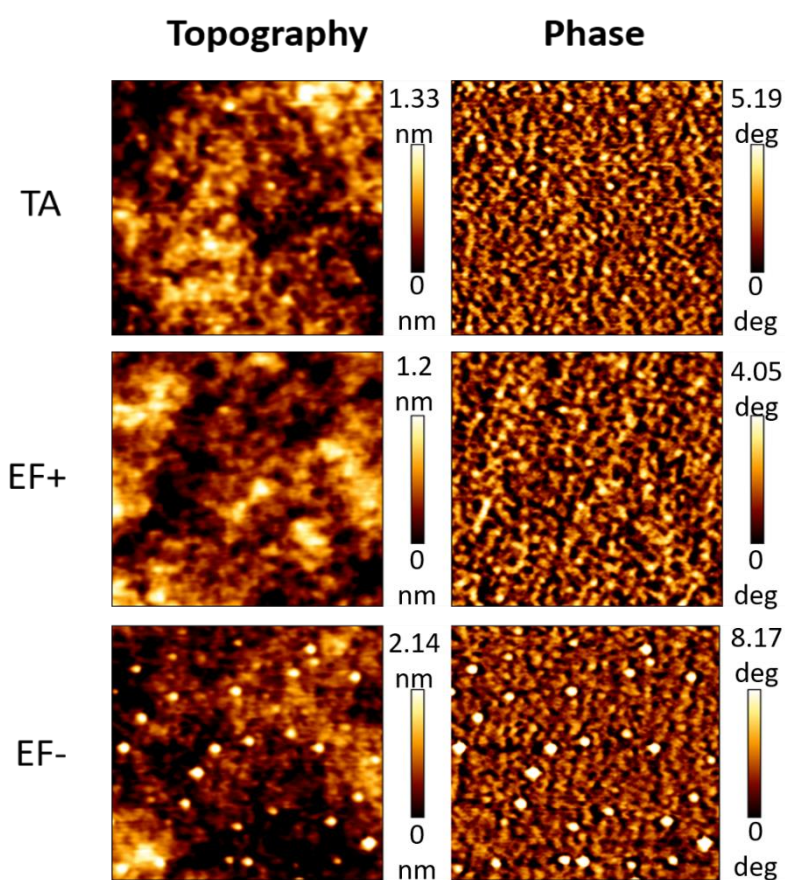
Figure 4.10 *Typical topography and phase AFM images (1.5 μm x 1.5 μm) of SA48: PC₇₀BM BHJ thin films. TA corresponds to thermally annealed control devices. EF(+) and EF(-) corresponds to EFTA treated devices with positive and negative directions of polarity, respectively. EF strength ≈ 8.3 x 10³ V/cm. Experimental setup is described in the caption of Figure 2.6.*

AFM images of the BHJ films provide insight into the morphological variations introduced by the EFTA treatment. Typical Topography and Phase images (1.5 μm x 1.5 μm) of BHJ films for control and EFTA treated devices is shown in Figure 4.10. For EF(-) treatment, features of $PC_{70}BM$ -type aggregation towards the film surface can be observed. It is then inferred that this response is similar to the ones obtained in earlier chapters where $PC_{70}BM$ redistributes towards the top of the film with EF(-) treatment and $PC_{70}BM$ moves to the BHJ-ZnO interface with EF(+) treatment. It is not clear if there is a competition between donor and acceptor molecules in responding to EFTA results. Results indicate that clearly reorganization of the $PC_{70}BM$ distribution in the active layer due to the electric field during the treatment.

From the AFM studies, it can be inferred that the response to EFTA treatment is mainly because of the $PC_{70}BM$ redistribution in the active layer. Also, it is expected that by careful tuning of the process parameters, improved efficiency numbers can be obtained in these systems.

4.4.3 Solar cell characteristics
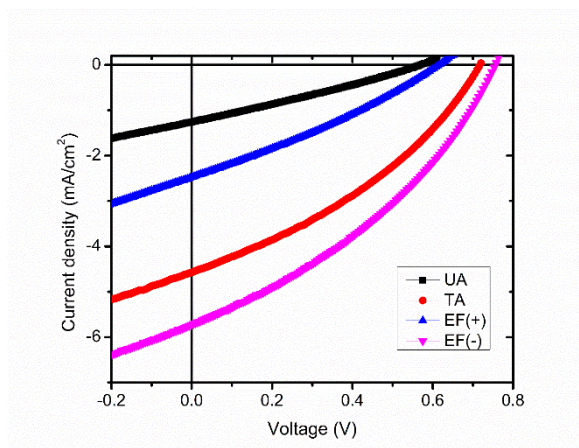
Figure 4.11 *Typical J-V characteristics of SA48: $PC_{70}BM$ BHJ solar cells under 1sun light illumination. UA and TA correspond to untreated and thermally annealed control devices. EF(+) and EF(-) corresponds to EFTA treated devices with positive and negative directions of polarity, respectively. EF strength $\approx 8.3x10^3$ V/cm. Experimental setup is described in the caption of Figure 2.8.*

Solar cells were fabricated (as mentioned in chapter 2) in inverted-device architecture (ITO/ZnO (40nm) /BHJ/MoOx (10 nm)/Ag (100 nm)). Typical solar cell characteristics under 1 sun illumination are shown in Figure 4.11. Solar cell parameters obtained from a large set of devices (> 10 devices for each case) are shown in Table 4.2.

The data indicates there is a strong dependence on EFTA treatment on the solar cell parameters. EF(-) treatment is shown to increase device performance when compared to TA devices. V_{oc} increases from ≈ 0.7 V to ≈ 0.74 V, while J_{sc} increases from ≈ 4.22 mA/cm^2 to ≈ 5.26 mA/cm^2. However, there is a slight reduction in FF for EF(-) treated devices when compared to TA devices. EF(+) treatment reduces device efficiencies with respect to TA devices with a considerable reduction in all the solar cell parameters

Table 4.2 *Typical solar cell parameters of SA48: PC$_{70}$BM solar cells under 1 sun illumination. TA corresponds to the thermally annealed control device. EF(+) and EF(-) correspond to EFTA treated devices, with positive and negative directions of polarity maintained during the treatment, respectively. EF strength $\approx 8.3 \times 10^3$ V/cm.*

	V_{oc} (V)	J_{sc} (mA/cm^2)	Fill Factor (%)	Efficiency (%)
TA	0.7±0.01	4.22±0.23	36.07±0.45	1.07±0.08
EF(+)	0.63±0.01	2.86±0.90	30.47±0.76	0.56±0.19
EF(-)	0.74±0.01	5.26±0.32	34.71±0.79	1.36±0.13

4.4.4 Dependence of solvent on EFTA treatment of SA48: PC$_{70}$BM solar cells

To understand the origin of the apparent response of PC$_{70}$BM molecule to EFTA treatment, studies were carried out by varying the solvent used in the fabrication of BHJ solutions of SA48: PC$_{70}$BM. Earlier studies were carried out with dichlorobenzene (DCB) with 4% di-iodo-octane (DIO) as the solvent. BHJ solutions were fabricated without additive in dichlorobenzene and chlorobenzene (CB), respectively. The boiling points of the solvents used in the fabrication are in the order CB (131 °C) < DIO (168 °C) < DCB (180 °C) respectively. The vapour pressures of the solvents are in the order DIO (0.04 Pa) < DCB (133 Pa) < CB (1200 Pa) respectively. Summary of the normalized solar cell efficiencies of the solar cell as a function of EFTA treatment for different solvents is shown in Figure 4.12.

From the results, it is clear that the response of the BHJ films to EFTA treatment is limited to the case in which DCB+ DIO was used as the solvent. It can be observed that the presence of DIO brings in a drastic enhancement in the response of the active layer to the EFTA treatment.

It has been shown earlier that DIO selectively dissolves PC$_{70}$BM molecules.[26] DIO also stays longer in the solvent phase due to its low vapour pressure. It is inferred that this measure results

in PC$_{70}$BM molecules to dwell longer in the solvent phase after the film formation. Staying longer in the solvent phase provides a larger degree of response upon applying the external electric field during EFTA treatment and arrive at a reorganized distribution with a preference towards a top-half or bottom-half of the active layer film. This feature of the vertical distribution depends on the polarity of the EF applied during the treatment.
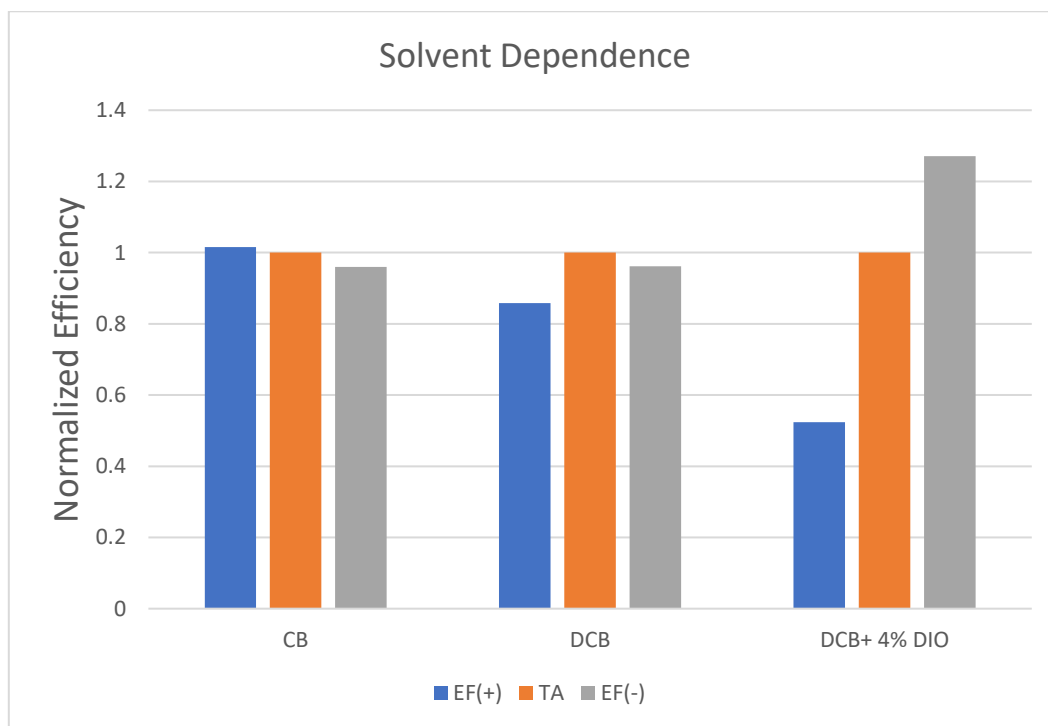
Figure 4.12 *Power conversion efficiencies of SA48: PC$_{70}$BM solar cells obtained under 1 sun illumination with different solvent conditions, Chlorobenzene (CB), Dichlorobenzene (DCB), Dichlorobenzene + 4% Diiodooctane (DCB +4% DIO). TA corresponds to the thermally annealed control device. EF(+) and EF(-) correspond to EFTA treated devices, with positive and negative directions of polarity maintained during the treatment, respectively. EF strength ≈ 8.3 × 10^3 V/cm. Efficiencies obtained have been normalized with efficiency obtained at TA conditions for each solvent case.*

It should be mentioned that in order to generalize this EFTA induced structural reorganization observed in solution-processed films of the small molecule donor (SA48)-fullerene system, a larger range of small molecule donor studies need to be carried out. However, this trend of SA48 systems is similar to that observed in macromolecule-donor: PC$_{70}$BM systems. The EFTA-polarity dependent effect of PC$_{70}$BM based BHJs (with small-molecule SA48 donor or macromolecular P3HT/PTB7) with the presence of additive-DIO are however not observed in non-fullerene based BHJs. This is indeed interesting and points to the importance of secondary

factors such as acceptor molecular diffusivity and aggregation promoting parameters to arrive at a final microstructure.

Extensive studies of EFTA treatment involving many different combinations of active layer components, selective solubilities, additives can justify this processing procedure in the fabrication of efficient OSCs. Further, EFTA treatment on ternary BHJ solar cells (two donors and one acceptor or one donor and two acceptors) involving both non-fullerene acceptor and fullerene acceptor can be expected to improve the device efficiencies even higher. Solvents with higher boiling point and lower saturated vapour pressure may benefit in improving the response of molecules to EFTA treatment.

4.5 Summary

Studies of molecular systems like ITIC in BHJ as an acceptor did not exhibit clear trends to EFTA treatment. The device results were in agreement with surface imaging observation indicating the absence of any significant changes to the morphology.

Studies of BHJ with small-molecule donor (SA48) systems indicates $PC_{70}BM$ reorganization upon EFTA treatment. The effect of $PC_{70}BM$, which selectively dissolves upon introduction of additive-DIO, leads to EFTA effects which are dependent on the polarity. This trend is similar to that observed in macromolecule-donor: $PC_{70}BM$ systems.

It was not possible to correlate these results to the dipole moment estimates of these molecules calculated using DFT (in the gas phase, and high electric field magnitude). The dipole moment of the SA48 molecule in these estimates was higher than that of $PC_{70}BM$ molecule. These results are indicative of the importance of secondary factors in EFTA treatment.

References

1. Yan, C.; Barlow, S.; Wang, Z.; Yan, H.; Jen, A. K. Y.; Marder, S. R.; Zhan, X., Non-fullerene acceptors for organic solar cells. *Nature Reviews Materials* **2018,** *3*, 18003.

2. Wadsworth, A.; Moser, M.; Marks, A.; Little, M. S.; Gasparini, N.; Brabec, C. J.; Baran, D.; McCulloch, I., Critical review of the molecular design progress in non-fullerene electron acceptors towards commercially viable organic solar cells. *Chemical Society Reviews* **2019,** *48* (6), 1596-1625.

3.   Zhang, G.; Zhao, J.; Chow, P. C. Y.; Jiang, K.; Zhang, J.; Zhu, Z.; Zhang, J.; Huang, F.; Yan, H., Nonfullerene Acceptor Molecules for Bulk Heterojunction Organic Solar Cells. *Chemical Reviews* **2018,** *118* (7), 3447-3507.

4.   Li, S.; Ye, L.; Zhao, W.; Zhang, S.; Mukherjee, S.; Ade, H.; Hou, J., Energy-Level Modulation of Small-Molecule Electron Acceptors to Achieve over 12% Efficiency in Polymer Solar Cells. *Advanced Materials* **2016,** *28* (42), 9423-9429.

5.   Zhao, W.; Qian, D.; Zhang, S.; Li, S.; Inganäs, O.; Gao, F.; Hou, J., Fullerene-Free Polymer Solar Cells with over 11% Efficiency and Excellent Thermal Stability. *Advanced Materials* **2016,** *28* (23), 4734-4739.

6.   Zhao, W.; Li, S.; Zhang, S.; Liu, X.; Hou, J., Ternary Polymer Solar Cells based on Two Acceptors and One Donor for Achieving 12.2% Efficiency. *Advanced Materials* **2017,** *29* (2), 1604059.

7.   Zhang, Y.; Yao, H.; Zhang, S.; Qin, Y.; Zhang, J.; Yang, L.; Li, W.; Wei, Z.; Gao, F.; Hou, J., Fluorination vs. chlorination: a case study on high performance organic photovoltaic materials. *Science China Chemistry* **2018,** *61* (10), 1328-1337.

8.   Fan, Q.; Zhu, Q.; Xu, Z.; Su, W.; Chen, J.; Wu, J.; Guo, X.; Ma, W.; Zhang, M.; Li, Y., Chlorine substituted 2D-conjugated polymer for high-performance polymer solar cells with 13.1% efficiency via toluene processing. *Nano Energy* **2018,** *48*, 413-420.

9.   Zhang, H.; Yao, H.; Hou, J.; Zhu, J.; Zhang, J.; Li, W.; Yu, R.; Gao, B.; Zhang, S.; Hou, J., Over 14% Efficiency in Organic Solar Cells Enabled by Chlorinated Nonfullerene Small-Molecule Acceptors. *Advanced Materials* **2018,** *30* (28), 1800613.

10.   Lin, Y.; Wang, J.; Zhang, Z.-G.; Bai, H.; Li, Y.; Zhu, D.; Zhan, X., An Electron Acceptor Challenging Fullerenes for Efficient Polymer Solar Cells. *Advanced Materials* **2015,** *27* (7), 1170-1174.

11.   Gao, L.; Zhang, Z.-G.; Bin, H.; Xue, L.; Yang, Y.; Wang, C.; Liu, F.; Russell, T. P.; Li, Y., High-Efficiency Nonfullerene Polymer Solar Cells with Medium Bandgap Polymer Donor and Narrow Bandgap Organic Semiconductor Acceptor. *Advanced Materials* **2016,** *28* (37), 8288-8295.

12.   Bin, H.; Zhang, Z.-G.; Gao, L.; Chen, S.; Zhong, L.; Xue, L.; Yang, C.; Li, Y., Non-Fullerene Polymer Solar Cells Based on Alkylthio and Fluorine Substituted 2D-Conjugated Polymers Reach 9.5% Efficiency. *Journal of the American Chemical Society* **2016,** *138* (13), 4657-4664.

13.   Zhao, W.; Li, S.; Yao, H.; Zhang, S.; Zhang, Y.; Yang, B.; Hou, J., Molecular Optimization Enables over 13% Efficiency in Organic Solar Cells. *Journal of the American Chemical Society* **2017,** *139* (21), 7148-7151.

14.   Luponosov, Y. N.; Min, J.; Solodukhin, A. N.; Bakirov, A. V.; Dmitryakov, P. V.; Shcherbina, M. A.; Peregudova, S. M.; Cherkaev, G. V.; Chvalun, S. N.; Brabec, C. J.; Ponomarenko, S. A., Star-shaped D–π–A oligothiophenes with a tris(2-methoxyphenyl)amine core and alkyldicyanovinyl groups: synthesis and physical and photovoltaic properties. *Journal of Materials Chemistry C* **2016,** *4* (29), 7061-7076.

15.   Ponomarenko, S. A.; Luponosov, Y. N.; Min, J.; Solodukhin, A. N.; Surin, N. M.; Shcherbina, M. A.; Chvalun, S. N.; Ameri, T.; Brabec, C., Design of donor–acceptor star-shaped oligomers for efficient solution-processible organic photovoltaics. *Faraday Discussions* **2014,** *174* (0), 313-339.

16.   Luponosov, Y. N.; Min, J.; Solodukhin, A. N.; Kozlov, O. V.; Obrezkova, M. A.; Peregudova, S. M.; Ameri, T.; Chvalun, S. N.; Pshenichnikov, M. S.; Brabec, C. J.; Ponomarenko, S. A., Effects of electron-withdrawing group and electron-donating core combinations on physical properties and photovoltaic performance in D-π-A star-shaped small molecules. *Organic Electronics* **2016,** *32*, 157-168.

17.   Kozlov, O. V.; Luponosov, Y. N.; Ponomarenko, S. A.; Kausch-Busies, N.; Paraschuk, D. Y.; Olivier, Y.; Beljonne, D.; Cornil, J.; Pshenichnikov, M. S., Ultrafast Charge Generation Pathways in Photovoltaic Blends Based on Novel Star-Shaped Conjugated Molecules. *Advanced Energy Materials* **2015,** *5* (7), 1401657.

18.   Min, J.; Luponosov, Y. N.; Gasparini, N.; Xue, L.; Drozdov, F. V.; Peregudova, S. M.; Dmitryakov, P. V.; Gerasimov, K. L.; Anokhin, D. V.; Zhang, Z.-G.; Ameri, T.; Chvalun, S. N.; Ivanov, D. A.; Li, Y.; Ponomarenko, S. A.; Brabec, C. J., Integrated molecular, morphological and interfacial engineering towards highly efficient and stable solution-processed small molecule solar cells. *Journal of Materials Chemistry A* **2015,** *3* (45), 22695-22707.

19.   Carsten, B.; Szarko, J. M.; Son, H. J.; Wang, W.; Lu, L.; He, F.; Rolczynski, B. S.; Lou, S. J.; Chen, L. X.; Yu, L., Examining the Effect of the Dipole Moment on Charge Separation in Donor–Acceptor Polymers for Organic Photovoltaic Applications. *Journal of the American Chemical Society* **2011,** *133* (50), 20468-20475.

20.   Li, M.; Zhou, Y.; Zhang, J.; Song, J.; Bo, Z., Tuning the dipole moments of nonfullerene acceptors with an asymmetric terminal strategy for highly efficient organic solar cells. *Journal of Materials Chemistry A* **2019,** *7* (15), 8889-8896.

21.   Bhattacharyya, K.; Surendran, A.; Chowdhury, C.; Datta, A., Steric and electric field driven distortions in aromatic molecules: spontaneous and non-spontaneous symmetry breaking. *Physical Chemistry Chemical Physics* **2016,** *18* (45), 31160-31167.

22.   Jissy, A. K.; Datta, A., Effect of External Electric Field on H-Bonding and π-Stacking Interactions in Guanine Aggregates. *ChemPhysChem* **2012,** *13* (18), 4163-4172.

23.   Liang, Q.; Han, J.; Song, C.; Yu, X.; Smilgies, D.-M.; Zhao, K.; Liu, J.; Han, Y., Reducing the confinement of PBDB-T to ITIC to improve the crystallinity of PBDB-T/ITIC blends. *Journal of Materials Chemistry A* **2018,** *6* (32), 15610-15620.

24.   Tremolet de Villers, B. J.; O'Hara, K. A.; Ostrowski, D. P.; Biddle, P. H.; Shaheen, S. E.; Chabinyc, M. L.; Olson, D. C.; Kopidakis, N., Removal of Residual Diiodooctane Improves Photostability of High-Performance Organic Solar Cell Polymers. *Chemistry of Materials* **2016,** *28* (3), 876-884.

25.   Huang, D. M.; Mauger, S. A.; Friedrich, S.; George, S. J.; Dumitriu-LaGrange, D.; Yoon, S.; Moulé, A. J., The Consequences of Interface Mixing on Organic Photovoltaic Device Characteristics. *Advanced Functional Materials* **2011,** *21* (9), 1657-1665.

26.   Lee, J. K.; Ma, W. L.; Brabec, C. J.; Yuen, J.; Moon, J. S.; Kim, J. Y.; Lee, K.; Bazan, G. C.; Heeger, A. J., Processing Additives for Improved Efficiency from Bulk Heterojunction Solar Cells. *Journal of the American Chemical Society* **2008,** *130* (11), 3619-3623.

Chapter 5

Organic Ferroelectric Memristors (OFMs) and Electric Field Assisted Thermal Annealing (EFTA) Treatment of Organic Ferroelectric Memristors

This chapter deals with the application of electric-field assisted thermal annealing (EFTA) treatment on binary mixtures consisting of ferroelectric polymer with dilute levels of a semiconducting polymer. The films obtained from the blend solutions of these components reveal memory resistor switching properties. The effectiveness of EFTA in optimising organic ferroelectric memristors is described in this chapter.

5.1 Memristor

Memristor is the amalgamation of the terms 'memory' and 'resistor'. It is a non-linear passive two-terminal electrical component. Along with resistor, capacitor and inductor, the memristor is now increasingly accepted as a basic circuit element.[1, 2] Memory-devices consisting of memory-cell elements which store data and information are integral to any basic computing and storage product. Each memory cell at a fundamental level differentiates between two states, retains them for long periods and retrieves them when the need arises.

Memristor is a type of memory device in which memory is stored as two different resistance states of the device, low resistance state and high resistance states. The low resistance state (LRS) and high resistance state (HRS) acts as ON and OFF states of the memory, respectively. ON-OFF ratio of a memristor is given by the ratio between the current in the ON-state to the current in OFF-state.[3]

Memristors devices can be obtained from a different variety of systems and phenomena. A common feature in these different approaches is the availability of two resistance (conductance) states for a given external voltage. Some of them are mentioned below:

1. Conductive filament(s) based devices[4, 5]
2. Redox based-devices[6]
3. Phase change-based devices[7]
4. Magnetic tunnel junction-based devices[8]
5. Organic ferroelectric material-based devices

5.2 Organic ferroelectric memristor (OFM)

5.2.1 Active layer

Ferroelectric organic memristors are a branch of memristors in which the active layer is a blend of ferroelectric (FE) polymer and semiconducting (SC) polymer sandwiched between two electrodes.[3, 9] Ferroelectric polymers are a class of crystalline polar polymers that

exhibit ferroelectricity, implying that they maintain a permanent electric polarization that can be reversed, or switched, by an external bias. Polyvinylidene fluoride (PVDF) and its copolymers are class of dielectrics which has been explored for its ferroelectric functionalities and are known to exhibit polymorphism.

The possibility of dispersing small fraction of semiconducting polymers and small molecules in this matrix opens up a platform to address important problems involving the molecular organization in confined volume. When dilute levels of SC are cast in host FE polymer matrix, the SC is likely to be confined in the amorphous phase. Earlier results from our laboratory of small-molecule fluorescent chromophores in the FE matrix revealed emission characteristics suggesting different forms of the aggregation within the confined matrix.[10] The simultaneous combination of confined space and local electric-field effects originating from the crystalline phase of the FE matrix provides a valuable control of the electrical transport via the semiconductor fraction.

Blend films of FE and SC polymers have shown to yield completely phase-separated SC domains embedded in the matrix of FE polymer.[11] Studies of composition variation by changing the FE: SC ratio indicated:[11]

i.   Domain sizes of SC polymer regions increased linearly with increasing fraction of SC polymer
ii.   The number of SC domains decreases almost linearly with the reciprocal SC content

These observations indicated the phase separation of the active layer is spinodal decomposition-driven rather than nucleation-driven. The substrate on which blend film is cast is shown to have only a negligible role in dictating the phase separation of the components.

The built-in electric field of the FE matrix can be used to modulate the electronic transport of the dispersed semiconductor. The net conduction between the top and bottom substrate electrodes is largely through the network of SC polymer which forms vertical channels in the FE matrix and is accompanied by barrier hopping and tunnelling mechanisms in the non-semiconducting pathways.

5.2.2 Working of organic ferroelectric memristors

The blend composition is so chosen that the semiconducting polymer content is marginally above the percolation threshold required to provide connectivity between the two electrodes. The distribution of the semiconducting polymer should be such that physical barriers for

contact with electrodes are absent. The work function level of the metal electrodes should position with the energy levels of the SC to limit injection at the metal-SC interface. In the absence of such ideal conditions, the transport can be dominated by injection limited mechanisms.
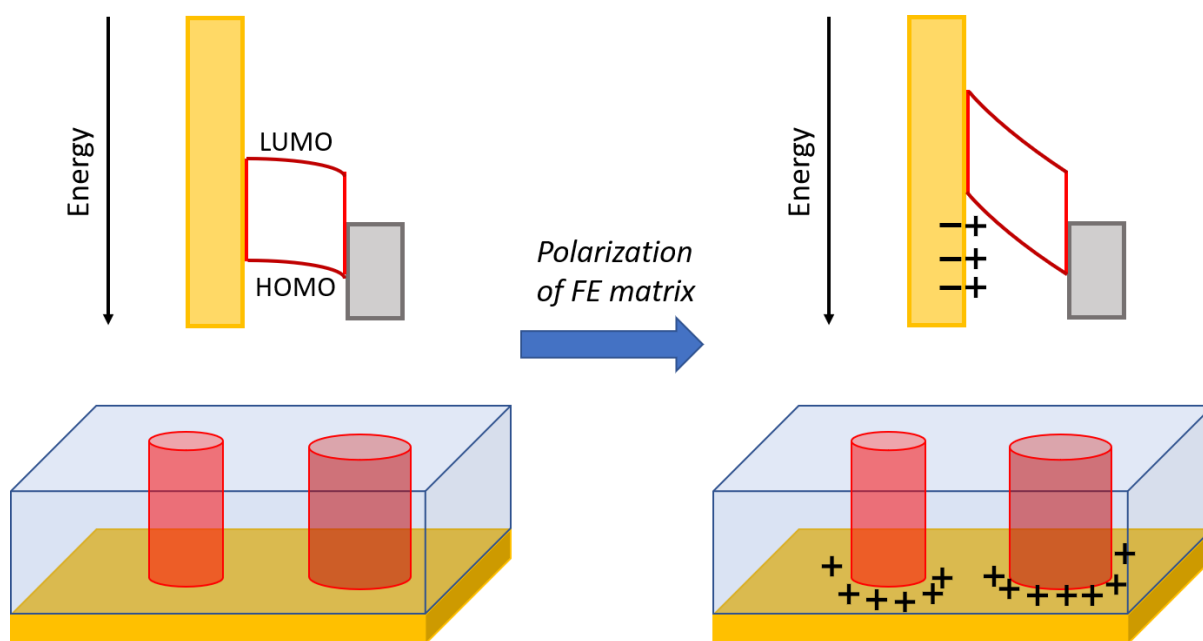
Figure 5.1 *Working of a ferroelectric memristor suggested by Ref. [9] In the schematic, red regions indicate SC polymer, and blue regions indicate the FE polymer matrix. Yellow indicates metal electrodes.*

The polarization state of the FE matrix has been shown to increase the injection of charge carriers into the SC regions from the electrode. The exact mechanism of how the polarization state influences the charge injection is debatable. It has been suggested that polarization of FE matrix-induced band bending of the SC at the metal interface. When the FE matrix is poled such that electrons get accumulated close to the electrode, holes will accumulate in the SC phase at the electrode interface. The stray field from the FE matrix and the resultant accumulated charges in the SC material gives rise to bend bending of SC energy levels at the metal electrode.[9, 12] This allows tunnelling injection of charge carriers from the metal into the SC regions, thereby increasing the current density.[13] This high conduction state acts as the low resistance state (LRS) of the memristor device, defined as the ON-state. The device can be switched to the OFF state by changing the direction of polarisation of the FE polymer, which will bring in charge carriers of the opposite type at the interface, which will increase the injection barrier. The polarization state of the FE polymer matrix for this scenario then controls the conduction state of the SC polymer channels. A simplistic schematic to depicting a situation

when the FE matrix is polarised with field strength above its coercive field is shown in Figure 5.1.
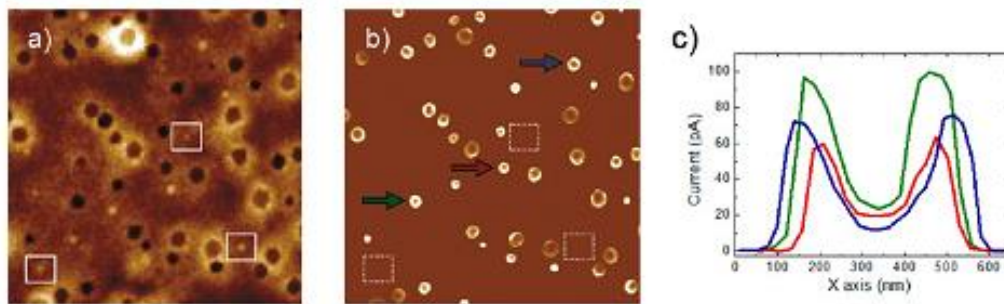
Figure 5.2 *Conductive-AFM images (10 × 10 μm²) of a F8BT/P(VDF-TrFE) (9:1 w/w) blend on Au. (a) Topography (total vertical scale of 110 nm). (b) Corresponding current map taken with C-AFM at +15 V applied bias to the bottom electrode (120 pA). (c) Line sections over three (labelled with coloured arrows) conductive domains indicated in panel b. (Reproduced with permission from Ref. [14])*

It is to be noted in this picture that the band bending of the SC polymer only occurs in the vicinity of the FE polymer where the influence of the electric field of FE polymer is appreciable. This band bending leads to a situation where the periphery of the SC in close proximity to the FE polymer only allows current in the ON state.[14] Some aspects of this speculation can be justified by CAFM measurements, where the conducting tip can be used to identify semiconductor regions and also used to measure the current. This is evident in the CAFM image shown in Figure 5.2. Line scan across CAFM image over conducting region shows the current is maximum at the interface between SC polymer and FE polymer.

5.2.3 Limitations of organic ferroelectric memristors

A realistic model is far more complex. A wide range of length scales and issues from classical models of polymer chain organisations to electronic interfaces come into play. The possibility that SC channels in the FE matrix need not always form bridging-channels between the top and bottom electrodes (for the present case of low volume SC fraction) is shown in Figure 5.3. These SC regions in the FE matrix which do not form bridging-channels does not contribute to the current through the device, limiting the maximum obtainable current.[15, 16] The current during the ON-state decides the ON-OFF ratio of the device. The uncertainty arising out of the statistical factors can be a bottleneck in scaling down these OFM devices.

Figure 5.3 *Schematic of a ferroelectric memristor adapted from Ref. [15]. In the schematic, red regions indicate SC polymer, and blue regions indicate the FE polymer matrix. Yellow indicates metal electrodes. It can be seen that not all the SC channels bridge bottom and top electrodes.*

Another factor that determines the current through the memristors is the size of the SC domains at the electrode interface. Since band-bending and resultant switching in conduction states only occur at the interface area between the SC and FE regions, the domain sizes of the SC at the electrodes play a huge role in determining the maximum current. For maximum current through the device, the domain sizes have to be small so that interface area between SC and FE materials can be maximized (as shown in Figure 5.4). But there is a critical threshold (d_{crit}) of domain sizes below which the current is no longer injected into SC material even in ON-state. This is because when domain sizes are below d_{crit}, the stray field from the FE from the opposite ends of SC domains cancel each other, which subsequently neutralises the band-bending of SC polymer, and limits current injection.
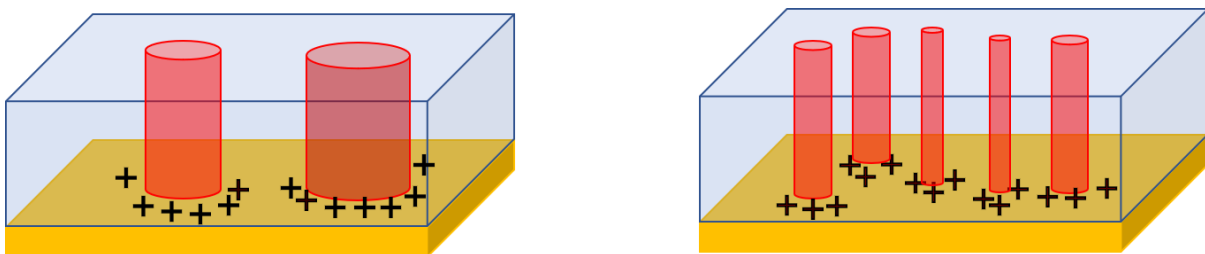
Figure 5.4 *Schematic of a ferroelectric memristor in ON-state with different dimensions of SC channels. In the schematic, red regions indicate SC polymer, and blue regions indicate the FE polymer matrix. Yellow indicates metal electrodes*

5.3 Morphology control of organic ferroelectric memristors (OFMs)

Several lithography inspired strategies have been attempted to control the morphology of OFM films. [16, 17] In the work of Breemen et al., micro-contact printing was used to create regular patterns of Self-Assembled membranes (SAM) on the bottom substrates before blend film is cast. SAM was chosen such that PVDF-TrFE interacts more with it than the SC polymer, while SAM has more adhesion towards the bottom substrate. This strategy allowed them to create surface-directed growth of SC in the matrix of FE polymer. 10-fold increase of the ON-current and six-fold larger current modulation was obtained as a result of their treatment.

In the work of Sung, S. H et. al., electron-beam (e-beam) lithography was used to create regular patterns in PVDF-TrFE film, which was then filled with P3HT polymer solution to create ordered OFMs. Using this strategy, they were able to change the domain size of the SC regions in this study. Ordered OFMs with SC regions of optimum domain sizes ($\approx$ 400nm) were able to give ON-OFF ratios ($\sim 10^3$) more than twice as higher than the corresponding conventional OFMs (ON-OFF ratio $\sim$ 500).

These strategies are limited by the resolution of the lithographic process ($\sim\mu$m) and scaling up of these strategies will be a challenging endeavour. The possibility of electric field-assisted thermal annealing (EFTA) treatment to control the morphology and transport characteristics of the composite film is explored in this chapter.

5.4 Fabrication of organic ferroelectric memristors

In our studies, Poly(vinylidene fluoride-co-trifluoroethylene) (PVDF-TrFE) is used as FE material; Poly(3-hexylthiophene-2,5-diyl) (P3HT) and Poly(9,9-di-n-octylfluorenyl-2,7-diyl) (PFO) is used as SC material.

5.4.1 PVDF-TrFE

PVDF-TrFE is a co-polymer of vinylidene fluoride and trifluroethylene obtained in the monomer ratios of 70: 30. This is an insulating polymer and used as a dielectric in the fabrication of organic capacitors, organic field-effect transistors (OFETs), sensors, etc. PVDF-TrFE in thin-film form is a mixed-phase ferroelectric material with predominating crystalline domains which are FE in nature. FE behaviour of PVDF-TrFE films is observed by temperature-dependent Polarization-Electric field (P-E) responses. PVDF-TrFE in its ferroelectric (FE) phase can hold a typical surface charge density of 10 μC/cm^2.[18] The dielectric

constant of PVDF-TrFE increases with temperature till the Curie temperature ($T_c \approx 125 \, ^oC$) is reached.[18-22] When temperature $T>T_c$, the polymer chains undergo a structural rearrangement from polar all-trans (β-phase) form to less polar alternating trans-gauche form (α-phase) along with a reduction in the bulk dielectric constant. In this paraelectric phase ($T > T_c$), even though the polarisation is absent, the polymer still retains its semi-crystallinity.
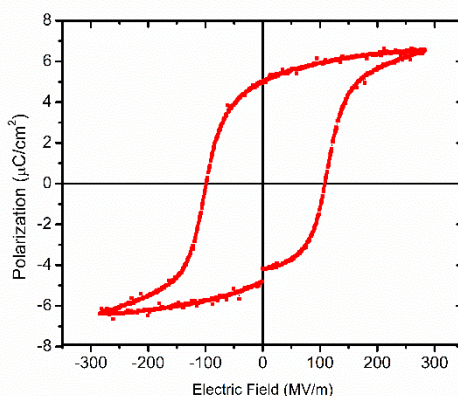

Figure 5.5 *Polarization obtained as a function of Electric Field for pristine PVDF-TrFE thin films. The film was sandwiched between gold electrodes. The thickness of the film was around 350 nm. P-E measurement was carried out by using Precision Materials Analyzer, Radiant Technologies.*

P-E characteristics of thermally annealed PVDF-TrFE films sandwiched between gold electrodes (100 nm) is shown in Figure 5.5. The hysteresis indicate the ferroelectric nature of the PVDF-TrFE film. This is in good agreement with earlier reports from our laboratory.[23] Ferroelectric property of the PVDF-TrFE thin films can also be captured in the Piezo Force Microscopy (PFM) images, as shown in Figure 5.6. PFM amplitude (Figure 5.6a) is a measure the amplitude of out-of-plane piezoelectricity in the vicinity of the surface.

5.4.2 Semiconducting Polymers

5.4.2.1 P3HT

P3HT (poly(3-hexylthiophene-2,5-diyl)) is a regio-regular semiconducting semi-crystalline polymer whose repeating units are 3-hexyl-thiophene. It is a hole semiconducting polymer with hole mobilities $\sim 10^{-4}$ cm^2/Vs in bulk and 10^{-1} cm^2/Vs in the FET architecture.[24] The HOMO and LUMO energy levels of the polymer is around -5.2 eV and -3.2 eV respectively. The band-gap of the polymer is about 1.9-2 eV.
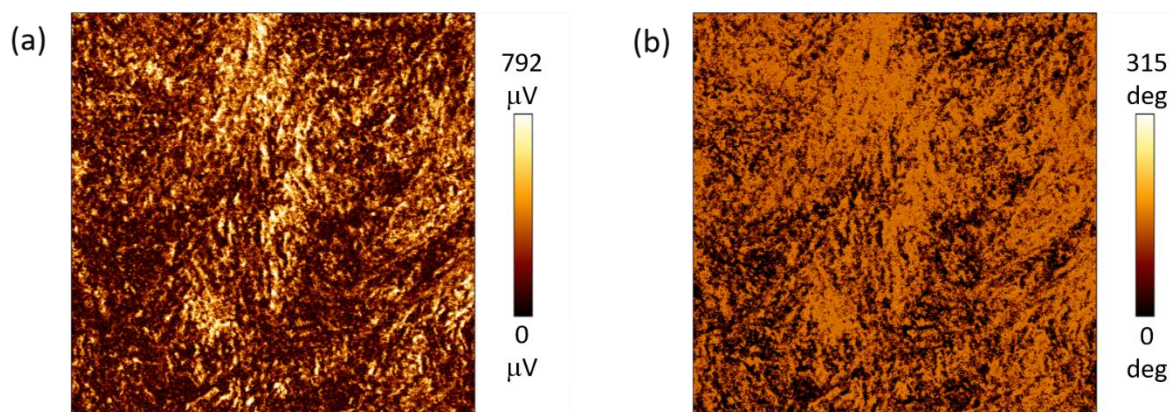
Figure 5.6 *a) Amplitude and b) phase of (5 μm x 5 μm) PFM images of pristine PVDF-TrFE thin films. Peak-to-peak AC voltage of 12 Volts was applied during the scan. Experimental setup is described in the caption of Figure 2.6. Budget sensor silicon AFM tips coated with Chromium/Platinum with resonance frequency 13 kHz and force constant 0.2 N/m was used in contact-mode for the study.*

5.4.2.2 PFO

PFO (Poly(9,9-di-n-octylfluorenyl-2,7-diyl)) is a polyfluorene derivative used mainly as active material in the organic light-emitting diodes (OLEDs). This molecule is also shown to have liquid crystalline properties.[25] PFO is also a hole semiconductor with hole mobilities close to 10^{-5} cm^2/Vs.[26] The HOMO and LUMO levels of this polymer are around -5.8 eV and -2.6 eV respectively.

PVDF-TrFE: P3HT memristors have achieved ON-OFF ratios of ~10^2-10^3 with silver electrodes and ~10^2 with gold electrodes.[3, 9] Retentivity times of more than 10 days have been obtained for these devices.[27] PVDF-TrFE: PFO memristors have reached ON-OFF ratios of 10^4-10^5 with gold electrodes with retentivity times of more than one week.[3, 28, 29]

5.4.3 Fabrication of organic ferroelectric memristors

Initially, PVDF-TrFE and P3HT (or PFO) are taken in 3:1 solution of cyclohexanone and tetrahydofuran in the ratio 9:1 in weight (total concentration of the solution is 50 mg/ml). The solution is kept stirring overnight at 80 °C. Active layer solution is spin-coated on Aluminium coated glass or Indium doped Tin Oxide coated glass (ITO) respectively, inside the glovebox. Thermal annealing at 140 °C for 1 hour inside the glove box. Top electrode (Al (100nm)) was then deposited using thermal deposition at 10^{-6} mbar base pressure to fabricate OFM.

5.4.3.1 I-V characteristics

Typical I-V characteristics of a thermally treated OFM device is shown (in Figure 5.7). Unlike the insulating nature of pristine PVDF-TRFE film, the composite device (10 % semiconducting polymer fraction in PVDF-TRFE matrix) exhibited typical memristor characteristics. The scan direction originates from -15V to +15V and retraces to -15V. (sweep rate = 0.5 V/s) It can be clearly seen that depending on the direction of the voltage sweep; there exist two different current states for a given voltage value. Consider, for example, the voltage -5V in Figure 5.7. It can be observed that there is an HR-OFF state and LR-ON state, respectively. The current states can be in-turn switched between ON and OFF states by applying +20V and -20V voltage pulses respectively. It should be noted that the I(V) curves are dependent on the sweep rate. However, the trends observed in Fig. 5.6 persisted even for the slowest sweep rate measured. This attribute is also reflected in the time-dependent measurements.
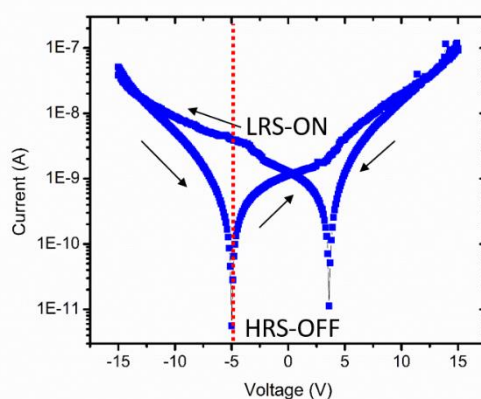
Figure 5.7 *Typical I-V characteristics of a memristor (PVDF-TrFE: PFO) where the voltage scan was from -20 V to +20 V and then back to -20 V. It can be seen that depending on the direction of the scan; there exist two current states for the same voltage values. LR-ON state and HR-ON state can be seen at -5V volts (indicated in vertical dashed red line). Current-Voltage studies were carried out using Keithley 4200 Semiconductor Characterization system.*

5.4.3.2 AFM imaging

AFM imaging of the active layer surface was carried to understand the surface morphology. Typical topography image is showed in Figure 5.8a. The films indicated high roughness ~ 100 nm. Topography will be discussed more in detail in the later sections. Corresponding Conductive-AFM image of Figure 5.8a is shown in Figure 5.8b. The circular regions indicate the periphery of the SC and FE regions where the conductivity is maximum. Typical line scan

across a conducting SC domain extracted from the CAFM image is shown in Figure 5.8c. These results correlate well with CAFM data reported earlier for memristor blend films.[14]
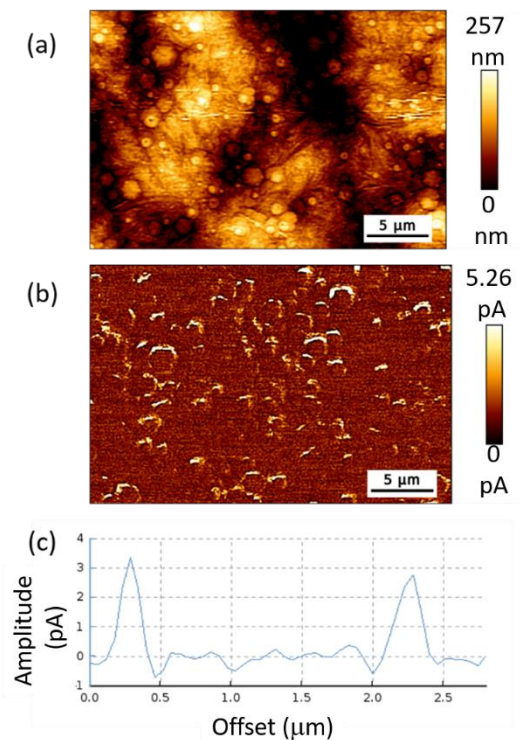

Figure 5.8 *a) Typical Topography image of PVDF-TrFE: PFO films. b) Corresponding Conductive-AFM image obtained with +10 V applied bias to the bottom electrode. c) Line scan across a conducting region in the CAFM image. Experimental setup is described in the caption of Figure 2.6. Budget sensor silicon AFM tips coated with Chromium/Platinum with resonance frequency 13 kHz and force constant 0.2 N/m was used in contact-mode for the study.*

5.5 EFTA treatment of organic ferroelectric memristors

EFTA treatment was carried out for the active layer similar to the methodology used for the EFTA treatment of solar cells and is shown in the schematic (Figure 5.9)

Active layer solution is spin-coated on Aluminium coated glass or Indium doped Tin Oxide coated glass (ITO) respectively inside the glove box. The spin-coated substrate is then taken to a heating stage. A temporary top electrode is brought over the active layer and kept separated by a spacer ($\approx$ 1.35 mm). Voltage is then applied between the top and bottom electrodes; such that the top electrode was connected to the positive terminal while the bottom electrode was grounded. Thermal annealing for 140 ºC (> ferroelectric transition temperature T_c) for 1 hour is then carried out on the active layer. Voltage is maintained throughout the thermal annealing

process. After the annealing process, the voltage terminals are removed along with the temporary top electrode and spacer. All of these steps are carried out inside the glove box. For the thermally annealed control devices, no voltage is applied during the treatment. A permanent top electrode is then deposited by thermal deposition to complete the organic ferroelectric memristor device. Thermally annealed control devices and Electric-Field-assisted thermally annealed devices are referred to TA and EFTA devices, respectively.
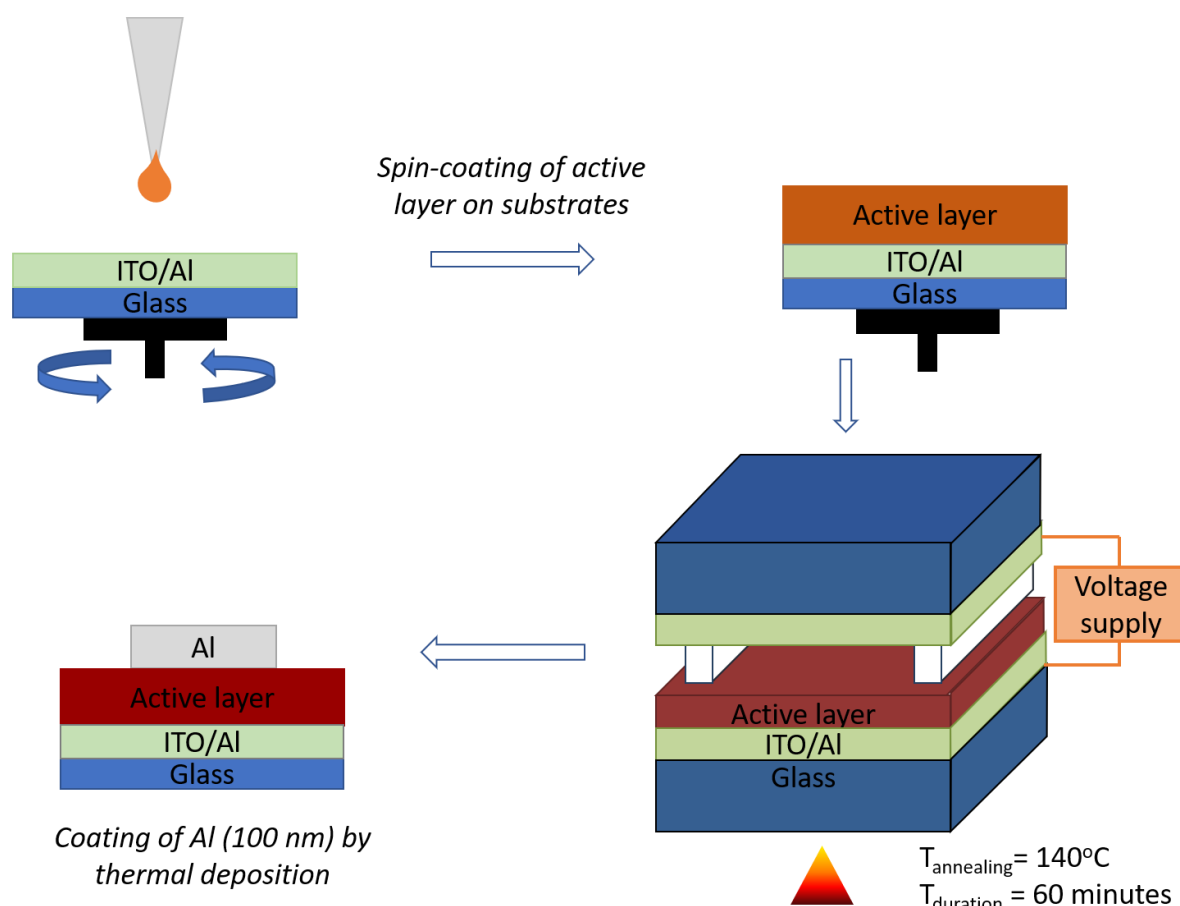
5.9 Schematic representation of the methodology of Electric field-assisted thermal annealing (EFTA) treatment of Organic Ferroelectric Memory (OFM) devices

5.5.1 Characterization

5.5.1.1 XRD studies

The morphological changes induced by EFTA treatment in PVDF-TrFE: PFO blend films was examined by GIWAXS studies. The GIWAXS spectra of blend films are shown in Figure 5.10. The peak corresponding to semi-crystalline PVDF-TrFE is present in both the TA and EFTA treated films. This peak at $2\theta \approx 19.8°$ (d = 4.48 Å) corresponding to the (110)/ (200) peak of the low temperature ferroelectric β phase of P(VDF-TrFE). It can be observed that EFTA

treatment improves the crystalline quality of the PVDF-TrFE, reflected in the narrowing of the peak. Scherrer's analysis of the PVDF-TrFE peak indicated enhancement in coherence lengths from 5.5 nm to 8 nm with EFTA treatment.
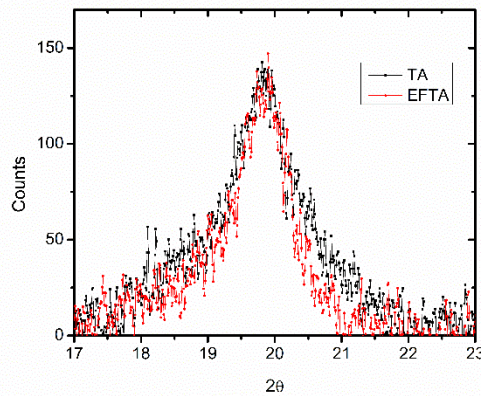
Figure 5.10 *GIWAXS spectra of PVDF-TrFE: PFO blend films. TA and EFTA correspond to thermally annealed, and electric field-assisted thermally annealed films respectively. Experimental setup is described in the caption of Figure 2.7.*

5.5.1.2 I-V characteristics
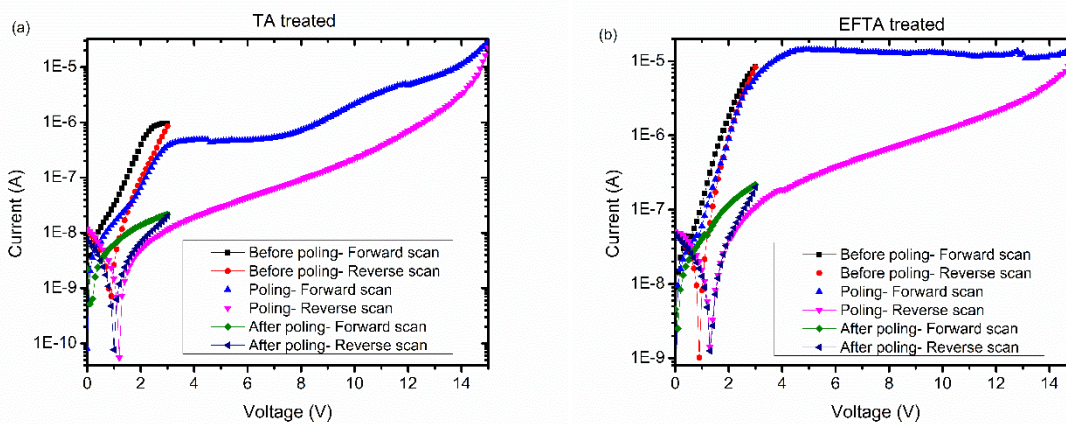
Figure 5.11 *Typical I-V characteristics of a) Thermally annealed and b) EFTA treated memristor (PVDF-TrFE: P3HT) devices. Forward (0 V to +3 V) and Reverse (+3 V to 0 V) directions of measurement scan before poling are represented in black and red curves respectively. Forward (0 V to +15 V) and Reverse (+15 V to 0 V) directions of poling scan are represented in blue and pink curves respectively. Forward (0 V to +3 V) and Reverse (+3 V to 0 V) directions of measurement scan after poling are represented in green and navy curves respectively. Current-voltage measurements were carried out using Keithley 4200 Semiconductor Characterization System.*

Effect of EFTA treatment was observed by studying I-V characteristics of treated and untreated OFM devices. Typical I-V characteristics for control (TA) and EFTA treated PVDF-TrFE: P3HT OFMs in the positive voltage axis, are shown in Figure 5.11. Black and red curves indicate the current in the forward and reverse scans during the ON-state of the OFM device. Blue and Pink curves indicate the forward and reverse scans during the poling scan. After the application of the poling scans, the device is set to OFF-state. Green and navy curves indicate the current in the forward and reverse scans during the OFF-state of the OFM device. It can be seen that higher current values are obtained for EFTA treated devices than the control TA devices. Currents improve by an order of magnitude in both the OFF-state and ON-states of device operation. This observation points to improved-order, implying reduced-barrier and/or enhanced charge injection at the interface. There is also a trend of saturation of current at lower voltage values for EFTA devices.
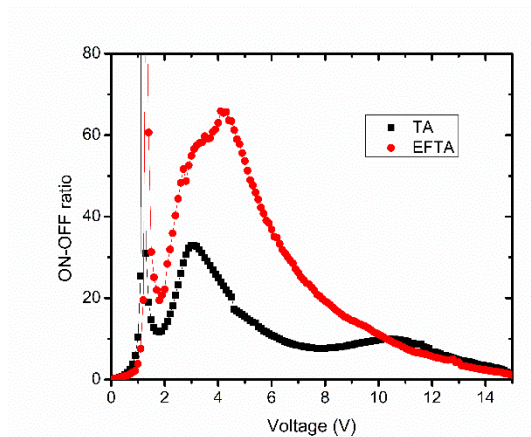
Figure 5.12 *ON-OFF ratio as a function of voltage extracted from the poling scans of TA and EFTA treated devices (PVDF-TrFE: P3HT) of Figure 5.11.*

Higher ON-OFF ratios obtained for the EFTA treated when compared to TA devices can be seen in Figure 5.12. ON-OFF ratio was obtained by dividing the current value during the forward scan with current value during the reverse scan for every voltage value.

Similar I-V characteristics were obtained for PVDF-TrFE: PFO OFMs is shown in Figure 5.13. The forward poling scan (0 V to +10V) and Reverse poling scan (+10 V to 0 V) directions are represented in black and red curves for both TA and EFTA treated devices, in Figures 5.13a and 5.14b. It can be seen that the reverse scans have higher current than the forward scan since the poling the FE has switched the SC conducting channels to ON-state. Higher magnitudes of current are obtained for EFTA treated devices than corresponding TA devices. ON-OFF ratios,

as a function of voltage, obtained from curves in Figure 5.13a and 5.13b is shown in Figure 5.13c. The ON-OFF ratios of PFO: PVDF-TrFE memristors are higher than the P3HT: PVDF-TrFE. This is because of the lower-lying HOMO levels of PFO when compared to P3HT. It can be observed that ON-OFF ratios of the EFTA treated devices are higher than TA treated devices, in almost the entire voltage range. Also, EFTA treated devices, allows highest ON-OFF ratios ($> 10^3$) at a lower voltage, which allows using a lower read voltage.
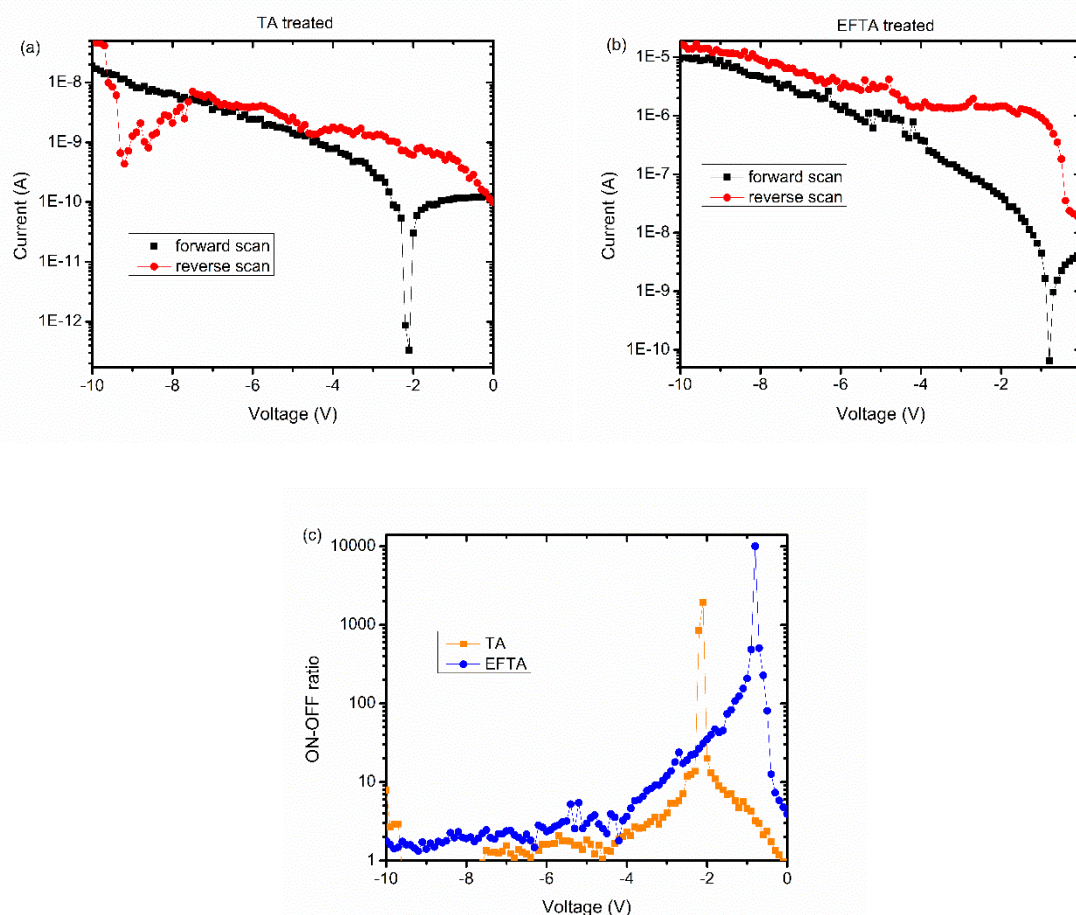
Figure 5.13 *a) and b) Typical I-V characteristics of a) Thermally annealed and b) EFTA treated memristor (PVDF-TrFE: PFO) devices. Forward poling scan (0 V to -10V) and Reverse poling scan (-10 V to 0 V) directions are represented in black and red curves, respectively. c) ON-OFF ratio as a function of voltage extracted from the poling scans of TA and EFTA treated devices of a) and b). Current-Voltage studies were carried out using Keithley 4200 Semiconductor Characterization system.*

The device characteristics obtained for the memristors is relatively lesser than the corresponding values reported in the literature.[3, 9, 27-29] This, however, can be improved by

optimizing the processing conditions. It has to be noted that EFTA treatment is shown to improve the performance parameters when compared to the control devices.

5.5.1.3 Retentivity and cyclability studies

It can be observed that the voltage corresponding to the maximum ON-OFF ratio, V_{max}, is significantly lower for EFTA devices (Figure 5.14). V_{max} is usually chosen as the probe (read-out) pulse voltage used to measure the state of the device. Since read-out is a destructive process in OFM devices, lower magnitudes of probe pulse voltages (V_{max}) are expected to improve long term retentivity. To confirm this hypothesis, retentivity studies were carried out. OFM devices were initially set to ON-state (by applying 20 V pulse). 20 V was chosen because it corresponds to electric field strength higher than the coercive field strength of the PVDF-TrFE matrix. ON-state was then read-out by applying suitable probe pulses voltages (V_{max}) at regular intervals of time. Decay profiles of ON-current measured at the probe voltage indicates an initial rapid decay and reaches a saturation level for both the EFTA and TA devices. The decay profiles were fitted to an exponential process. The time taken for ON-current to reduce 90% of its initial value was found to be ≈ 1269 s and 870 s for EFTA and TA devices respectively, for similar measurement parameters. Reduced probe voltages used for EFTA devices has led to longer retentivity times when compared to TA devices.
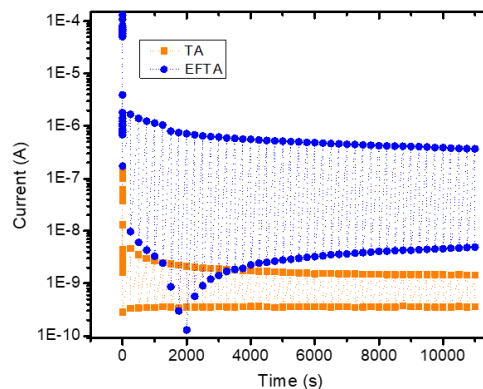
Figure 5.14 *Retentivity studies: 20V pulse (400 ms) is initially applied to set the memristor to ON-state. ON-current is then measured at probe voltage pulses of 75 ms (-4.1V for TA devices and -1.3V for EFTA devices) at intervals of 250 seconds.*

Cyclability studies (>250 cycles) carried out on OFM devices to verify that the higher current magnitudes obtained for EFTA devices were retained after multiple cycles (Figure 5.15). Each cycle involves, a voltage pulse to set the device to ON-state, followed by a probe pulse to

measure the ON-current, a voltage pulse to set the device to OFF-state, followed by a probe pulse to measure the OFF-current. It can be seen that the current magnitudes reduce by an order of magnitude for both TA and EFTA devices over 250 cycles. However, EFTA devices have higher current magnitudes and maintain similar ON-OFF ratios, than corresponding TA devices.
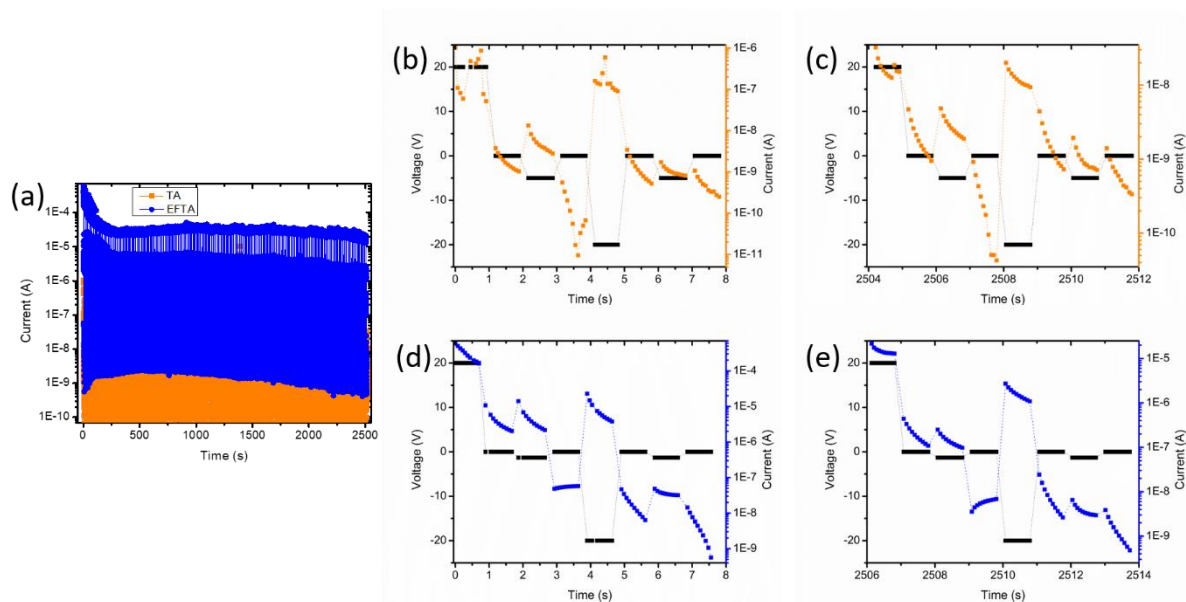
Figure 5.15 *Typical current values of TA and EFTA memristor devices obtained during cyclability studies (>250 cycles). Each cycle involves a +20 V set pulse, followed by a probe pulse and -20 V set pulse, and ends with probe pulse. Pulses at +20 V and -20 V set the devices into ON and OFF state respectively. Each cycle lasts about ~ 10s. (b) and (c) indicates the current values obtained for 1st cycle and 251st cycle for TA devices. (d) and (e) indicates the current values obtained for 1st cycle and 251st cycle for EFTA devices.*

The origin of the higher current magnitudes lies in the morphology modifications induced by the EFTA treatment. To understand the effect of EFTA treatment, the surface of the OFM active layer was investigated with Atomic Force Microscopy (AFM).

5.5.1.4 AFM imaging

Morphology-device performance correlations of OFMs have been well studied in the literature.[30, 31] Typical AFM images (10 μm x 10 μm) of OFM active layer shown in Figure 5.16. The circular regions which can be observed in the topography and phase images indicate the SC domains in FE matrix. It is expected that the SC regions extend into the bulk of the active layer. Some of these SC regions act as bridging channels between the top and bottom

electrodes. From earlier studies, it is known that SC regions which project out of the film (convex shape) do not reach the bottom electrode, as indicated in the schematic (Figure 5.3).[15] A typical image of the such SC region is indicated in the blue square in the AFM image (Figure 5.16). SC regions which reached the bottom substrate dip below the film (concave shape) as shown in the schematic (Figure 5.3) and indicated within a red square (Figure 5.16).
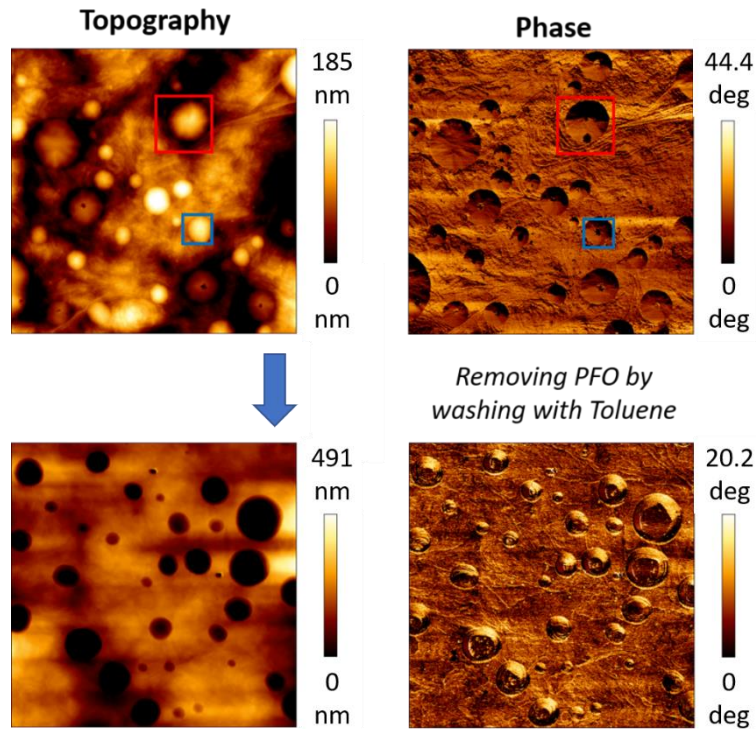
Figure 5.16 *Typical Topography and phase AFM (10 μm x 10 μm) images of PFO: PVDF-TrFE memristor blend film, before and after washing with Toluene to remove PFO. Bridging and non-bridging semiconductor channels are indicated in red and blue squares, respectively. Experimental setup is described in the caption of Figure 2.6. Budget sensor silicon AFM tips coated with gold coating with resonance frequency 300 kHz and force constant 40 N/m was used in tapping-mode for the study.*

SC material can be selectively removed by washing the film in toluene. The image shows the blend films without the PFO regions (Figure 5.16). Typical line scan across the topography image (Figure 5.17a) after the removal of SC material is shown in Figure (5.17b). It can be seen that not all the depressions left by the PFO reach the bottom electrode. The depressions which do not reach the bottom electrode are non-bridging channels that do not contribute to the current in the device. By image analysis using ImageJ software, the partial depressions left

non-bridging channels can be removed from the image. Typical resultant image after processing is shown in Figure 5.17c.

The resultant image (Figure 5.17c) only contains the domains of SC channels in contact with the bottom electrode. The domain size distribution of these bridging SC channels can be obtained by image analysis. Domain size distribution obtained for control films and EFTA-treated films from image analysis from a large number of such images is shown in Figure 5.17d. A clear transformation in the domain size distribution with EFTA treatment was observed. Domain sizes of smaller size are reduced in quantity with EFTA treatment when compared to the control films. EFTA treatment also increases the distribution of domain sizes of larger dimensions.
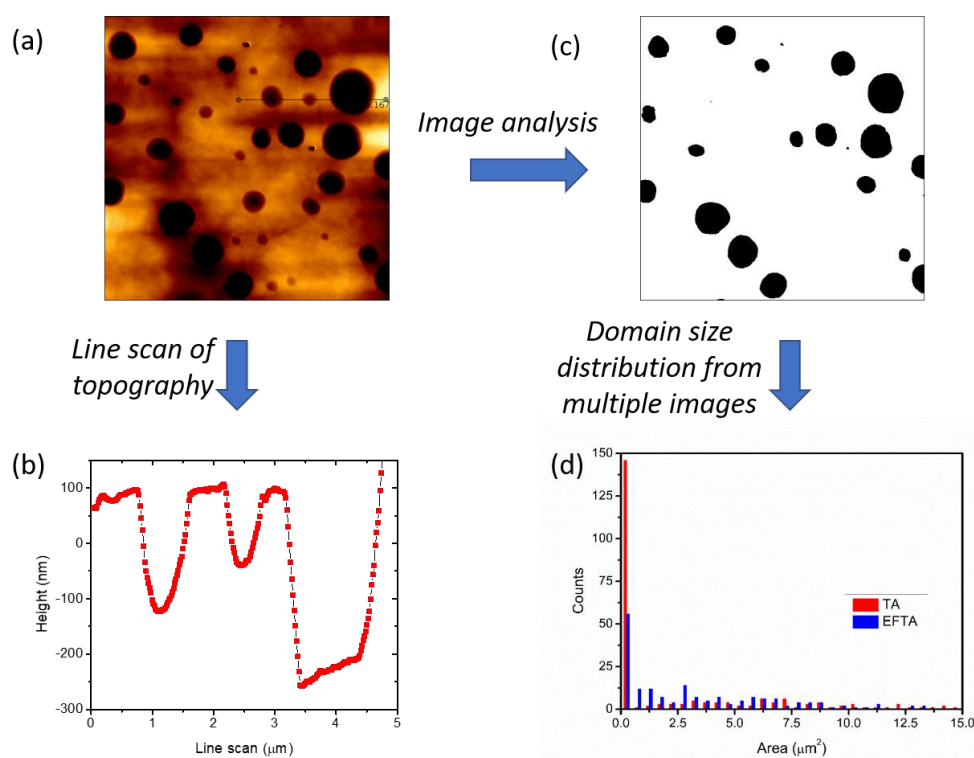
Figure 5.17 *a) Typical Topography AFM (10 μm x 10 μm) image of PFO: PVDF-TrFE memristor blend film, b) Typical topography line scan indicated by a black horizontal line in a), c) image analysis carried out to remove non-bridging Semiconductor channels. d) Domain size distribution obtained from multiple images for thermally annealed control (TA) and Electric field-assisted thermal annealing (EFTA) treated blend films.*

The overlap of images representing SC regions at the air-active layer interface (Figure 5.17(a)) and active layer-substrate interface (Figure 5.17(b)) reveals the bridged-domains, while the complementary fraction represents the non-bridged segments. Domain sizes of SC regions at

these two interfaces can be estimated from AFM images. Charge-injection into the SC from the electrodes occurs only around the SC-FE interface, i.e., regions close to the SC domains perimeter. From the domain size distribution, the effective charge injection region, given by the product of the circumference of the SC regions and spread of the charge injection region around the SC-FE interface (s in μm), was found to 26.38×s μm^2/100 μm^2 for TA treated films and 29.07×s μm^2/100 μm^2 for EFTA treated films respectively. Assuming that the spread of charge injection region (s) is independent of the treatment, it can be seen that the EFTA treatment improves the effective charge injection region by ~ 10 %.

5.5.1.5 Space charge limited current (SCLC) mobility studies:

To understand how EFTA treatment improves crystalline quality in the SC regions of the OFM active layer, SCLC hole mobility studies were carried out. SCLC mobility (μ) was obtained by fitting the obtained I-V curves to Mott–Gurney's square law,

$$I = \frac{9}{8} A_{eff} \varepsilon_0 \varepsilon_r \mu \frac{(V_{app} - V_{on})^2}{L^3} \tag{5.1}$$

where $\varepsilon_o \varepsilon_r$ - dielectric constant, L -film thickness, V_{app} - applied voltage, V_{on} is the voltage at which the OFM is switched to ON-state. Effective charge injection region obtained from the AFM analysis was used as the effective SC area (A_{eff}) for SCLC analysis (s was assumed to 50 nm for the calculations). μ obtained for TA and EFTA treated devices were 1.2±0.1 × 10^{-7} cm^2/Vs and 1.4±0.2 × 10^{-4} cm^2/Vs, respectively. EFTA treatment is found to improve μ by three orders of magnitude in the bridged SC regions.

The ability of EF to modify the FE-SC interface has been observed earlier in a similar study where EF was applied laterally on dielectric film during thermal annealing treatment. SC layer was then spin-coated on the treated/control FE dielectric surface. Organic field effect transistors fabricated with oriented PVDF-TrFE FE dielectric surface lead to a ~ 300 % higher μ at the SC-FE interface, than the control devices.

These studies suggest the possibility of structural reorganization in the active layer due to EFTA treatment. Improvement in current magnitudes due to EFTA can be attributed to factors contributing to the increase in the proportion of bridged SC channels and enhanced charge carrier mobility.

5.6 Summary

EFTA treatment provides additional control in improving the device characteristics of the two-component organic memristors. EFTA treatment was able to increase the current magnitudes in the organic ferroelectric memristor devices – in both PVDF-TrFE: PFO and PVDF-TrFE: P3HT devices. The improvement in current was attributed to an increase in bridged SC channels and enhancement in charge carrier mobility in the bridged semiconducting regions. This improvement in current magnitudes also subsequently improves the ON-OFF ratio of the EFTA treated devices. The presence of EF during the film annealing with FE polymer appears to be a natural driving force to an organised structure. Schematic representing the morphology change induced by the EFTA treatment is shown in Figure 5.18. This depiction is relatively simplistic but captures the essence of the key results.

(a) TA   (b) EFTA
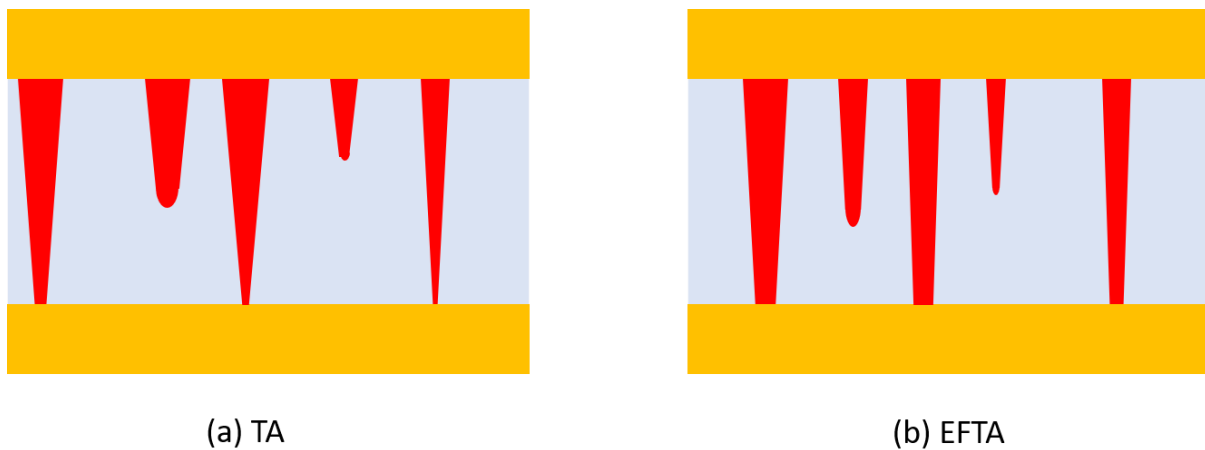
Figure 5.18 *Schematic of a possible morphology variation of the active layer of ferroelectric memristor a) Control Thermally annealed (TA) films, b) Electric field-assisted thermally annealed (EFTA) films. In the schematic, red regions indicate SC polymer, and blue regions indicate the FE polymer matrix. Yellow indicates metal electrodes. It can be seen that EFTA treatment increases domain sizes at active layer /bottom electrode interface.*

References

1.   Chua, L., Memristor-The missing circuit element. *IEEE Transactions on Circuit Theory* **1971,** *18* (5), 507-519.

2.   The memristor revisited. *Nature Electronics* **2018,** *1* (5), 261-261.

3.   Asadi, K.; de Boer, T. G.; Blom, P. W. M.; de Leeuw, D. M., Tunable Injection Barrier in Organic Resistive Switches Based on Phase-Separated Ferroelectric–Semiconductor Blends. *Advanced Functional Materials* **2009,** *19* (19), 3173-3178.

4.   Liu, Q.; Sun, J.; Lv, H.; Long, S.; Yin, K.; Wan, N.; Li, Y.; Sun, L.; Liu, M., Real-Time Observation on Dynamic Growth/Dissolution of Conductive Filaments in Oxide-Electrolyte-Based ReRAM. *Advanced Materials* **2012,** *24* (14), 1844-1849.

5.   Kim, K. M.; Jeong, D. S.; Hwang, C. S., Nanofilamentary resistive switching in binary oxide system; a review on the present status and outlook. *Nanotechnology* **2011,** *22* (25), 254002.

6.   Waser, R.; Dittmann, R.; Staikov, G.; Szot, K., Redox-Based Resistive Switching Memories – Nanoionic Mechanisms, Prospects, and Challenges. *Advanced Materials* **2009,** *21* (25-26), 2632-2663.

7.   Boniardi, M.; Redaelli, A.; Cupeta, C.; Pellizzer, F.; Crespi, L.; Arrigo, G. D.; Lacaita, A. L.; Servalli, G. In *Optimization metrics for Phase Change Memory (PCM) cell architectures*, 2014 IEEE International Electron Devices Meeting, 15-17 Dec. 2014; 2014; pp 29.1.1-29.1.4.

8.   Yao, X.; Harms, J.; Lyle, A.; Ebrahimi, F.; Zhang, Y.; Wang, J., Magnetic Tunnel Junction-Based Spintronic Logic Units Operated by Spin Transfer Torque. *IEEE Transactions on Nanotechnology* **2012,** *11* (1), 120-126.

9.   Asadi, K.; de Leeuw, D. M.; de Boer, B.; Blom, P. W. M., Organic non-volatile memories from ferroelectric phase-separated blends. *Nature Materials* **2008,** *7*, 547.

10.   Chellappan, K. V.; Kandappa, S. K.; Rajaram, S.; Narayan, K. S., Ferroelectric Polymer Matrix for Probing Molecular Organization in Perylene Diimides. *The Journal of Physical Chemistry Letters* **2015,** *6* (2), 224-229.

11.   Asadi, K.; Wondergem, H. J.; Moghaddam, R. S.; McNeill, C. R.; Stingelin, N.; Noheda, B.; Blom, P. W. M.; de Leeuw, D. M., Spinodal Decomposition of Blends of Semiconducting and Ferroelectric Polymers. *Advanced Functional Materials* **2011,** *21* (10), 1887-1894.

12.   Kemerink, M.; Asadi, K.; Blom, P. W. M.; de Leeuw, D. M., The operational mechanism of ferroelectric-driven organic resistive switches. *Organic Electronics* **2012,** *13* (1), 147-152.

13.   Ghittorelli, M.; Lenz, T.; Sharifi Dehsari, H.; Zhao, D.; Asadi, K.; Blom, P. W. M.; Kovács-Vajna, Z. M.; de Leeuw, D. M.; Torricelli, F., Quantum tunnelling and charge accumulation in organic ferroelectric memory diodes. *Nature Communications* **2017,** *8*, 15741.

14.   Khikhlovskyi, V.; Wang, R.; van Breemen, A. J. J. M.; Gelinck, G. H.; Janssen, R. A. J.; Kemerink, M., Nanoscale Organic Ferroelectric Resistive Switches. *The Journal of Physical Chemistry C* **2014,** *118* (6), 3305-3312.

15.   Khikhlovskyi, V.; van Breemen, A. J. J. M.; Michels, J. J.; Janssen, R. A. J.; Gelinck, G. H.; Kemerink, M., 3D-morphology reconstruction of nanoscale phase-separation in polymer memory blends. *Journal of Polymer Science Part B: Polymer Physics* **2015,** *53* (17), 1231-1237.

16.   van Breemen, A.; Zaba, T.; Khikhlovskyi, V.; Michels, J.; Janssen, R.; Kemerink, M.; Gelinck, G., Surface Directed Phase Separation of Semiconductor Ferroelectric Polymer Blends and their Use in Non-Volatile Memories. *Advanced Functional Materials* **2015,** *25* (2), 278-286.

17.   Sung, S. H.; Boudouris, B. W., Systematic Control of the Nanostructure of Semiconducting-Ferroelectric Polymer Composites in Thin Film Memory Devices. *ACS Macro Letters* **2015,** *4* (3), 293-297.

18.   Senanayak, S. P.; Guha, S.; Narayan, K. S., Polarization fluctuation dominated electrical transport processes of polymer-based ferroelectric field effect transistors. *Physical Review B* **2012,** *85* (11), 115311.

19.   Legrand, J. F., Structure and ferroelectric properties of P(VDF-TrFE) copolymers. *Ferroelectrics* **1989,** *91* (1), 303-317.

20.   Bellet-Amalric, E.; Legrand, J. F., Crystalline structures and phase transition of the ferroelectric P(VDF-TrFE) copolymers, a neutron diffraction study. *The European Physical Journal B - Condensed Matter and Complex Systems* **1998,** *3* (2), 225-236.

21.   Li, C.; Wu, P.; Lee, S.; Gorton, A.; Schulz, M. J.; Ahn, C. H., Flexible Dome and Bump Shape Piezoelectric Tactile Sensors Using PVDF-TrFE Copolymer. *Journal of Microelectromechanical Systems* **2008,** *17* (2), 334-341.

22.   Sharma, T.; Je, S.-S.; Gill, B.; Zhang, J. X. J., Patterning piezoelectric thin film PVDF–TrFE based pressure sensor for catheter application. *Sensors and Actuators A: Physical* **2012,** *177*, 87-92.

23.   Ashar, A. Z.; Narayan, K. S., Electric field induced ferroelectric-surface modification for high mobility organic field effect transistors. *Organic Electronics* **2017,** *42*, 8-12.

24.   Wang, G.; Swensen, J.; Moses, D.; Heeger, A. J., Increased mobility from regioregular poly(3-hexylthiophene) field-effect transistors. *Journal of Applied Physics* **2003,** *93* (10), 6137-6141.

25.   Chen, S. H.; Su, A. C.; Chen, S. A., Noncrystalline Phases in Poly(9,9-di-n-octyl-2,7-fluorene). *The Journal of Physical Chemistry B* **2005,** *109* (20), 10067-10072.

26.   Nicolai, H. T.; Wetzelaer, G. A. H.; Kuik, M.; Kronemeijer, A. J.; Boer, B. d.; Blom, P. W. M., Space-charge-limited hole current in poly(9,9-dioctylfluorene) diodes. *Applied Physics Letters* **2010,** *96* (17), 172107.

27.   Asadi, K.; Wildeman, J.; Blom, P. W. M.; Leeuw, D. M. d., Retention Time and Depolarization in Organic Nonvolatile Memories Based on Ferroelectric Semiconductor Phase-Separated Blends. *IEEE Transactions on Electron Devices* **2010,** *57* (12), 3466-3471.

28.   Asadi, K.; Li, M.; Stingelin, N.; Blom, P. W. M.; Leeuw, D. M. d., Crossbar memory array of organic bistable rectifying diodes for nonvolatile data storage. *Applied Physics Letters* **2010,** *97* (19), 193308.

29.   Li, M.; Stingelin, N.; Michels, J. J.; Spijkman, M.-J.; Asadi, K.; Beerends, R.; Biscarini, F.; Blom, P. W. M.; de Leeuw, D. M., Processing and Low Voltage Switching of Organic Ferroelectric Phase-Separated Bistable Diodes. *Advanced Functional Materials* **2012,** *22* (13), 2750-2757.

30.   Braz, T.; Ferreira, Q.; Mendonça, A. L.; Ferraria, A. M.; do Rego, A. M. B.; Morgado, J., Morphology of Ferroelectric/Conjugated Polymer Phase-Separated Blends Used in Nonvolatile Resistive Memories. Direct Evidence for a Diffuse Interface. *The Journal of Physical Chemistry C* **2015,** *119* (3), 1391-1399.

31.   Su, G. M.; Lim, E.; Kramer, E. J.; Chabinyc, M. L., Phase Separated Morphology of Ferroelectric–Semiconductor Polymer Blends Probed by Synchrotron X-ray Methods. *Macromolecules* **2015,** *48* (16), 5861-5867.

Chapter 6

Summary and Future Directions

6.1 Summary of the thesis

In this thesis, the effectiveness of electric-field assisted thermal annealing (EFTA) treatment in controlling the microstructure of two different types of organic devices; (organic solar cells (OSCs) and organic ferroelectric memristors (OFMs)) have been explored. The first chapter provided the essential background introduction and information to the various topics relevant to the thesis.

In the second chapter, studies of EFTA treatment applied to BHJ system of semi-crystalline donor (P3HT): fullerene acceptor (PCBM) was presented. It was observed that EFTA treated devices showed improvement in solar cell device performance when compared to corresponding thermally annealed control devices. EFTA treatment was able to control vertical phase separation of active layer components in thin films. The improvement in device performance was attributed to increased crystallinity of the donor domains and better optimized morphology for charge generation and charge extraction in the blend. Dependence of the molecular weight of donor polymer P3HT on the EFTA treatment was observed. The results indicated that EFTA treatment was more effective to create vertical phase segregation in the relatively less-crystalline higher molecular weight P3HT based BHJ system.

In the third chapter, EFTA treatment was shown to bring in vertical phase segregation in BHJ system of amorphous polymer donor PTB7-Th and PCBM. By careful optimization of the process parameters, EFTA treated solar cell devices were able to get efficiencies higher than only-thermal annealed devices. The enhanced device performance was due to better optimized morphology of the EFTA treated devices. Additive DIO used to improve the efficiency of PTB7-Th: PCBM solar cells have been shown to cause irreversible, detrimental morphological changes in the active layer over time. DIO was removed by the thermal annealing treatment leading to more stable solar cell devices. The possibility of solar cell devices, which were more efficient than control thermally annealed devices and more stable than control untreated devices, was demonstrated using the EFTA treatment.

In the fourth chapter, EFTA treatment was applied on two different systems, polymer donor (PBDB-T): non-fullerene acceptor (ITIC) based BHJ system and small molecule donor (SA48): fullerene acceptor based BHJ system. The non-fullerene based BHJ system did not show any discernible change with EFTA treatment, in the range of parameters used for the study. The small molecule donor (SA48): PCBM system indicated that the response to EFTA treatment is significant. It was observed that additive DIO used during the treatment plays a

crucial role in creating vertical phase separation in the active layer. DIO is a low vapour pressure solvent, resides longer in the film. PCBM was selectively dissolved by the additive and has the tendency to remains in the solvent phase much longer after the film is obtained from spin coating. This allows PCBM molecules to respond to EFTA treatment. No correlations were identified between the molecular dipole moments obtained through DFT calculations, and the corresponding response of the small molecules to EFTA treatment.

In the fifth chapter, EFTA treatment was used to improve the device performance of organic ferroelectric memristors. Two different active layer systems of PVDF-TrFE: PFO and PVDF-TrFE: P3HT was used for the study. EFTA treatment was shown to increase the current magnitudes for both the systems along with a lowering of the threshold voltage. This was attributed to EFTA treatment induced better optimized domain sizes of conducting channels of semiconductor polymers inside the ferroelectric matrix. The improvement in current magnitudes also reflected in better ON-OFF ratios for both the memristor systems.

6.2 Critical points and significance of the thesis

-The crystallinity of the polymer donor determines the response of blend film towards electric-field assisted thermal annealing (EFTA) treatment, with the largest variations appearing in relatively lesser crystalline polymer donor systems.

-The enhancement in device efficiency of semi-crystalline donor: PCBM solar cells with EFTA treatment has been identified to be due to improved hole mobility and optimal vertical phase segregation (VPS)

- EFTA treatment compensates efficiency lost during thermal annealing of amorphous donor: PCBM solar cells by improving VPS of active layer components. Removal of additive leads to more stable devices. Our work was the first report where EFTA treatment was shown to improve performance parameters of amorphous donor-based BHJ solar cells.

-The role of solvent additive (DIO) in the migration of PCBM with EFTA treatment was identified. The largest response to EFTA treatment was observed when DIO was used along with the native solvent.

-EFTA treatment enhances the performance of organic ferroelectric memristors by increasing the current densities in the devices. It was identified that EFTA treatment increases the proportion of bridging semiconducting channels and the mobility of charge carriers in these

regions. This is one of the first reports where an external treatment was used to improve the device characteristics of organic ferroelectric memristors.

6.3 Future Directions

Understanding the driving force behind the response of a certain set of molecules in different environments to EFTA treatment is critical in making the best use of this treatment. An extensive study involving different active layer components and different additives will help us understand the strengths and limitations of EFTA treatment. It is conceivable that EFTA treatment can further increase the high efficiencies demonstrated in certain new systems reported recently. Ternary solar cell BHJ systems which have one donor and two acceptors, with one of them being fullerene would be an interesting platform for this EFTA approach.

The observed effect of EFTA treatment of organic memristors, consisting of semiconducting polymer domains in a ferroelectric matrix, reveals a promising method to further improve device performance and the various figure of merit parameters. Extensive structural characterization accompanied by modelling is needed to improve the understanding and functioning of these devices.